

Either appear as you are or be as you appear.

Mevlana Celaleddin Rumi

University of Alberta

Fermion-Spin Interactions in One Dimension in the Dilute Limit

by

Fatih Doğan

A thesis submitted to the Faculty of Graduate Studies and Research
in partial fulfillment of the requirements for the degree of

Doctor of Philosophy

Department of Physics

©Fatih Doğan
Fall, 2009
Edmonton, Alberta

Permission is hereby granted to the University of Alberta Libraries to reproduce single copies of this thesis and to lend or sell such copies for private, scholarly or scientific research purposes only. Where the thesis is converted to, or otherwise made available in digital form, the University of Alberta will advise potential users of the thesis of these terms.

The author reserves all other publication and other rights in association with the copyright in the thesis and, except as herein before provided, neither the thesis nor any substantial portion thereof may be printed or otherwise reproduced in any material form whatsoever without the author's prior written permission.

Examining Committee

Frank Marsiglio, Physics

Jack Tyszynski, Physics

Kevin Beach, Physics

Mark Freeman, Physics

Samer Adeeb, Electrical Engineering

Erik Sorensen, Physics, McMaster University, Hamilton, ON, Canada

To
My Better Half

Abstract

In this thesis, we have analyzed one-dimensional fermion-spin interactions in the dilute limit. The two cases we analyze represent different paradigms. For the first part, we look at the existence of “spins” for all sites as an effective model to describe the rearrangement of core electrons within the dynamic Hubbard model. Within this model, the behavior of electrons and holes will be compared in the presence of fermion-spin coupling and on-site repulsion. It will be shown that in this framework, electrons and holes behave differently and even though electrons experience increased repulsion, holes show attraction for a range of on-site repulsions. The characteristics of the interaction show effective nearest-neighbor attraction though no such term exists within the model. By the analysis of dynamic properties, two regions of interaction are identified. The gradual change from weak to strong coupling of fermions is presented. The effect of introducing on-site repulsion for both ranges of coupling is presented for both the dynamic Hubbard model and electron-hole symmetric version.

For the second case involving fermion-spin interaction, we look at the interaction of a fermion with spins existing only for a small portion of the lattice, representing a coupled magnetic layer that an itinerant fermion interacts with through Heisenberg-like spin flip interaction. The interaction represents a spin-flip interaction of a spin current and magnetic layer. This interaction has been extensively studied for its relevance to computer hard drives both experimentally and theoretically. Most theoretical descriptions utilize the semi-classical Landau-Lifshitz-Gilbert (LLG) formalism. However, with recent improvements in experimental methods with very small magnetic layers and very fast real time measurements, quantum effects become more pronounced. We present quantum mechanical results that show considerable modification to spin-flip interaction. We identify a set of conditions that exhibits the existence of an emerging bound state for the spin current both numerically and analytically. The bound state is a quantum mechanical state and cannot be achieved with a classical picture. We present results in a one-dimensional lattice for a spin-1/2

system, and generalize our arguments to higher dimension and spins with $S > 1/2$.

Acknowledgements

I would like to thank first and foremost my supervisor, Dr. Frank Marsiglio whose support, direction and patience during the preparation of this thesis was invaluable. His constant presence and always welcoming attitude deserves more than just mere gratitude. Dr. Lucian Covaci has been my office mate and the first person I discussed any result or problem I had with research. His pointers and enthusiasm about computational world has shaped the way I perform research more than anyone. Dr. Wonkee Kim was the first person who included me in the scattering problem. That chapter would not have existed without his determination to understand the physics. I would like to thank the organizers of “CIFAR-PITP International Summer School on Numerical Methods for Correlated Systems in Condensed Matter” (2008) as I will cherish the knowledge I gained in the two weeks I spent in that summer school for years. On the personal side, I dedicate this thesis to my wife, who has always been there to keep me sane through the process, she has supported me emotionally and intellectually. She has typed most of the appendix named “plane wave derivation”. I thank my family, especially my mother for enduring me being so far away all these years, and to Temelli family for making Edmonton feel more like home with their warm friendship.

Table of Contents

1	Introduction	1
2	Models	5
2.1	Overview	5
2.2	Dynamic Hubbard Model (DHM)	7
2.3	Scattering of Spin Current From Magnetic Layers	9
3	Methods	11
3.1	Density Matrix Renormalization Group (DMRG)	11
3.1.1	Terminology:	11
3.1.2	The Methodology:	11
3.1.3	Finite Size	15
3.1.4	Calculation of Observables:	16
3.1.5	Variation to Standard Approach	17
3.2	Chebyshev Polynomial Expansions	18
3.2.1	General Arguments	18
3.2.2	Time Evolution of a Wavepacket	19
3.2.3	The Dynamic Response Functions	20
3.2.4	Handling the Delta Function	22
3.3	Computational Details	23
3.3.1	DMRG	23
3.3.2	Chebyshev Polynomial Expansion	25
4	Static Properties of the DHM	28
4.1	Introduction	28
4.2	Model	29
4.3	Density Profile	30
4.4	Relative Positions of the holes	35
5	Dynamical Response Functions of the DHM	55
5.1	Spectral Function	56
5.2	Optical Conductivity	64
6	Conclusions on the Dynamic Hubbard Model	73

TABLE OF CONTENTS

7 Non-Equilibrium Bound State	75
7.1 Introduction	75
7.2 Method	76
7.3 Numerical Results	77
7.4 Numerical Results with Proper Basis States	90
7.5 Analytical Approach	94
7.6 Generalizations	100
7.7 Conclusions	101
8 Conclusions	104
Bibliography	106
A Time Evolution Using Chebyshev Polynomials	110
A.1 Derivation	111
B Plane Wave Derivations	116
B.1 Case for $E > 3J_1$	121
B.2 Generalization to all J_1	125
B.3 Generalization to arbitrary S	126
C Expectation value of σ_z	132

List of Tables

5.1	The value of U_{eff} of the interacting holes, for the corresponding value of U for each model with $g = 3$ and $\omega_0 = 0.5$	64
5.2	The value of U of the interacting fermions, for the corresponding value of U_{eff} for the static Hubbard model with $g = 3$ and $\omega_0 = 0.5$	65

List of Figures

2.1	The terms of the Hamiltonian, Eq. 7.1 for the scattering of spin current off magnetic layer.	9
3.1	First iteration for the DMRG calculation. The two sites on the left will form the system and the two on the right will form the environment.	13
3.2	Procedure for infinite size systems. At each iteration, the neighboring sites are added to system (or environment) to increase its size by one. This is continued until convergence.	15
3.3	Procedure for finite size systems after the system size is reached. When one sweep is completed for the system, it is done for the environment as well.	16
3.4	The profile of interaction of pseudo-spin basis states within the dynamic Hubbard model. Non-zero elements of the Hamiltonian for this subspace are shown. This particular plot is for a 12 site system.	23
3.5	The density profile for $U = 16$ and $g = 4.0$. Failed and successful results are shown for comparison.	24
3.6	The Bessel function evaluated at indicated values over a range of orders.	25
3.7	The appearance of oscillatory behavior when the expansion is not accurate in the case of the spectral function. Dashed (green) line is as it appears in Fig. 5.3b for $U = 0$ and $g = 3$. The solid (red) curve is an inaccurate representation of dashed (green) curve.	27
4.1	Density profile of the Hubbard model for 20 sites. The profile is valid for both electron and hole.	31
4.2	Density profile of the Hubbard model for 40 sites, very low to very large on-site repulsions. The profile is valid for both electron and hole.	32
4.3	Density profile of the Hubbard model for 40 sites, using realistic on-site repulsions. The profile is valid for both electron and hole.	32
4.4	Change in the magnitude of the density for centre of the system (site 20) and centre of half system (site 12). The profile is valid for both electron and hole.	33
4.5	Density profile for DHM for electrons.	33
4.6	Density profile for DHM for holes for coupling constants a) $g = 0.5$, b) $g = 1.5$ and c) $g = 4.0$. Note the similarity of weak coupling (a) to the Hubbard model.	34

LIST OF FIGURES

4.7	Density profile for holes interacting via the dynamic Hubbard model. a) Extreme values of on-site repulsion for the onset of attraction (peaking) and repulsion (splitting) for different on-site repulsion. $g = 0.01$ is essentially identical to the Hubbard model. b) With increasing g , attractive behavior is observed for $U = 4$. c) When $U = 16$, we see effective repulsion for every coupling plotted.	36
4.8	Density-density correlation function for a 40-site system for the Hubbard model, for a) site 2 and b) site 10. The correlation is valid for both electrons and holes.	37
4.9	Density-density correlation function for a) site 20 of a 40-site and b) site 21 of a 41-site system for the Hubbard model. The correlation is valid for both electrons and holes.	38
4.10	Density-density correlation function of a 40-site system for the dynamic Hubbard model for electrons, $g = 1.5$	40
4.11	Density-density correlation function of holes for site 11 in a 40-site system for the dynamic Hubbard model for a) $g = 0.5$, b) $g = 1.5$ and c) $g = 4.0$. For intermediate (b) and strong coupling (c), formation of nearest neighbor peaks, though non-symmetric, is observed.	41
4.12	Density-density correlation function of holes for site 21 of 40-site system for the dynamic Hubbard model for a) $g = 0.5$, b) $g = 1.5$ and c) $g = 4.0$. Values are larger with respect to Fig. 4.11 since the reference site is much closer to the higher density region.	42
4.13	Normalized density-density correlation function (see text) for the Hubbard model for the onset of the on-site repulsion for a) site 2, b) site 10 and c) site 20. The density-density correlation function is divided by the the value of the density at the reference site and at the site it is measured. The results are valid for both electrons and holes.	43
4.14	Normalized density-density correlation function (see text) for the Hubbard model for a) site 2, b) site 10 and c) site 20. The density-density correlation function is divided by the the value of the density at the reference site and at the site it is measured. The results are valid for both electrons and holes.	44
4.15	Normalized density-density correlation function (see text) for the same system as Fig. 4.11. Unity is no-correlation. Attraction is observed for a wide range of the on-site repulsion for intermediate (b) to strong coupling (c).	47
4.16	Normalized density-density correlation function (see text) for the same system as Fig. 4.12. Unity is no-correlation. Attraction is observed for a wide range of the on-site repulsion for intermediate (b) to strong coupling (c).	48
4.17	Relative location of two holes for a 40-site system interacting via the dynamic Hubbard model with small (a), intermediate (b) and strong (c) on-site repulsion. Nearest neighbor attraction persists even for $U = 8$ with $g = 4$	49

LIST OF FIGURES

4.18	Change from attraction to repulsion by increasing on-site repulsion of two holes for a 40-site system interacting via the dynamic Hubbard model with small (a), intermediate (b) and strong (c) coupling. Attraction dies off at different points for different coupling constants . . .	50
4.19	Effect of spin frequency, ω_0 . For $\omega_0 = 0.5$, refer to Fig. 4.18a.	51
4.20	Coupling to spins as affected from ω_0 . Counter intuitive behavior is observed for the effect of frequency.	52
5.1	The $A^-(\omega)$ component of the spectral function for electrons interacting via the dynamic Hubbard model for a) $g = 1$ and b) $g = 3$ for a 12-site system with Hilbert space of 589,824. In both cases, the behavior is similar.	58
5.2	The value of the $A^-(\omega)$ component of the spectral function at $\omega = 0$ for electrons interacting via the dynamic Hubbard model for a 10-site system with Hilbert space of 102,400. The increase in energy scale of pseudo-spin has the same effect as changing the coupling. $\omega_0 = 0.5$ except as indicated.	59
5.3	The $A^-(\omega)$ component of the spectral function for two holes interacting via the dynamic Hubbard model for a) $g = 1$ and b) $g = 3$ for a 12-site system with Hilbert space of 589,824. The incoherent part is considerably enhanced with higher coupling.	60
5.4	The value of the $A^-(\omega)$ component of the spectral function at $\omega = 0$ for holes interacting via the dynamic Hubbard model for a 10-site system with Hilbert space of 102,400. As the coupling is increased, the peak at positive U moves to higher values and peak at negative U is revealed. The increase in energy scale of pseudo-spin has the same effect as changing the coupling for negative U , but only shows relatively lower enhancement to coupling.	61
5.5	The value of effective interaction U_{eff} for holes interacting via the dynamic Hubbard model for a 10-site system with Hilbert space of 102,400. The line shows where U_{eff} changes sign.	62
5.6	The value of effective interaction U_{eff} for holes interacting via the dynamic Hubbard model as a function of the parameters U and g for a 10-site system with Hilbert space of 102,400.	63
5.7	The value of effective interaction U_{eff} for fermions interacting via the static Hubbard model for a 10-site system with Hilbert space of 102,400. The line shows where U_{eff} changes sign.	64
5.8	The value of effective interaction U_{eff} for fermions interacting via the static Hubbard model as a function of the parameters U and g for a 10-site system with Hilbert space of 102,400.	65
5.9	The $A^-(\omega)$ component of the spectral function for fermions interacting via static Hubbard model for $g = 3$ for a 12-site system with Hilbert space of 589,824.	66

LIST OF FIGURES

5.10 The value of the $A^-(\omega)$ component of the spectral function at $\omega = 0$ for fermions interacting via the static Hubbard model. The behavior is similar to that of electrons in the dynamic Hubbard model for a 10-site system with Hilbert space of 102,400. 66

5.11 Reduced optical conductivity for holes interacting via the dynamic Hubbard model for a) $g = 1$ and b) $g = 3$ for a 12-site system with Hilbert space of 589,824. As the magnitude of the on-site repulsion is increased, the weight is pushed to higher frequencies especially at strong coupling. 68

5.12 The maximum of the reduced optical conductivity around $\omega = 0$ for holes interacting via the dynamic Hubbard model for a 10-site system with Hilbert space of 102,400. As the coupling is increased, the behavior for positive U is modified considerably. For strong coupling, a peak around $U = 0$ is formed. 69

5.13 Optical conductivity for holes interacting via the dynamic Hubbard model for a) $g = 1$ and b) $g = 3$ for a 12-site system with Hilbert space of 589,824. As the magnitude of the on-site repulsion is increased, the weight is pushed to higher frequencies especially at strong coupling. 70

5.14 Reduced optical conductivity for fermions interacting via static Hubbard model for $g = 3$ for a 12-site system with Hilbert space of 589,824. As the on-site repulsion is increased, the weight is pushed to lower frequencies. 71

5.15 The maximum of the reduced optical conductivity around $\omega = 0$ for fermions interacting via static Hubbard model for a 10-site system with Hilbert space of 102,400. As the coupling is increased, the trend is shifted to higher on-site repulsions. 71

5.16 Optical conductivity for fermions interacting via static Hubbard model for $g = 3$ for a 12-site system with Hilbert space of 589,824. 72

7.1 Time evolution of a wave packet, originally centered around site 700. The wave packet moves towards two local spins positioned at site indices 800 and 801, and interacts with the local spins with $J_0 = 2.0$, and $J_1 = 0.0$. After the interaction, some portion of the wave packet reflects back, and some of it transmits through with either spin. 78

7.2 Wave packet spin long after the wave packet interacts with the local spins. Top panel: As a function of both wave packet-spin, J_0 , and spin-spin interaction, J_1 , for 20 local spins. Bottom panel: Slices through J_1 for several constant values of J_0 . Many features are present, very difficult to interpret. For computational accuracy, 3000 site lattice is used with Hilbert space of 630,000. 79

7.3 Wave packet spin long after the wave packet interacts with the local spins. Slices through J_1 for $J_0 = 10$. Many features are present, and very difficult to interpret. With a smaller number of sites the wiggles are reduced in numbers. For three sites, there are three visible ones. Note that the y-axis is shifted for better visualization. Lowest J_1 point is the same for all curves. 80

LIST OF FIGURES

7.4	Wave packet spin long after the wave packet interacts with the local spins. Top panel: As a function of both wave packet-spin, J_0 , and spin-spin interaction, J_1 , for 2 local spins. Bottom panel: Slices through J_1 for several constant values of J_0 . Three regions are readily identified, low J_1 , very high J_1 and the ridge that is function of both J_0 and J_1 .	81
7.5	The resulting wave packet spin long after wave packet interacts with local spin(s). Results with a single local spin and two local spins are shown.	82
7.6	The resulting reflected and transmitted components of an incoming spin up wave packet long after wave packet interacts with local spin for a single local spin.	82
7.7	z-component of the wave packet spin for different wave packet-spin interaction strengths for several fixed J_1 . The behavior barely changes with the onset of spin-spin interaction. With larger values of J_1 , effectiveness of the spin flip interaction is reduced, following the trend shown in Fig. 7.4b.	84
7.8	z-component of local spins for different spin-spin interaction strength for $J_0 = 2$. The introduction of spin-spin interaction changes the behavior of the local spins considerably.	84
7.9	Time evolution of a wave packet, interacting with two local spins with $J_0 = 2.0$ with the same conditions as Fig. 7.1. The cases shown are a) $J_1 = 0.25$, b) $J_1 = 0.5$ and c) $J_1 = 1.0$.	86
7.10	Time evolution of a wave packet, interacting with two local spins with $J_0 = 2.0$, and $J_1 = 0.8$ with the same conditions as Fig. 7.1.	87
7.11	z-component of local spins for different spin-spin interaction strength for $J_0 = 2$. For $J_1 = 10$, two spins have the same value. Spin numbers are given with respect to the order they interact with the incoming spin up wave packet.	87
7.12	Time evolution of wave packet, interacting with two local spins with $J_0 = 8.0$, and $J_1 = 3.1$, short after the interaction. Note the logarithmic scale for y-axis. The wide peaks to the sides of the graph are reflected and transmitted components of the wave packet. $a = 6$ is used for this plot. The linear trend around the local spins is indicative of an exponential decay of the weight around the local spins.	89
7.13	Time evolution of wave packet, interacting with two local spins with $J_0 = 2.0$, and $J_1 = 1.4$, short after the interaction. Note the logarithmic scale for y-axis. The wide peaks to the sides of the graph are reflected and transmitted components of the wave packet. $a = 6$ is used for this plot. The linear trend around the local spins is indicative of an exponential decay of the weight around the local spins. There is very small slow moving packet revealed at late times.	89
7.14	Time evolution of the z component of the local spins for 2 sites. The cases along the ridge is shown. The legend is (J_0, J_1) , spin number in order of interaction with the wave packet. The final value of S_z is same for both spins. The second spin changes first.	90

LIST OF FIGURES

7.15 Time evolution of wave packet, interacting with two local spins with $J_0 = 2.0$, and $J_1 = 3.1$, short after the interaction. Note the logarithmic scale for y-axis. $a = 6$ is used for this plot. Since this set of parameters is away from the ridge, multiple reflections are observed instead of exponential decay. 91

7.16 Time evolution of wave packet, interacting with two local spins with $J_0 = 2.0$, The spin symmetric states a) $|h(x)|^2$, b) $|f(x)|^2$ and c) $|g(x)|^2$, are shown. 93

7.17 The component $|g(x)|^2$ right after the wave packet interacts with the local spins. We use $J_1 = 3.1$ and local spins are at sites 790 and 810. Note the logarithmic scale for the y-axis. The results correspond to earliest times in Figs. 7.12 and 7.15. 94

7.18 The component $|g(x)|^2$ integrated over the entire lattice right after the wave packet interacts with the local spins, using the same time step as Fig. 7.17. Note that scale for J_1 starts at one. 95

7.19 The component $|g(x)|^2$ integrated over the entire lattice long after the wave packet interacts with the local spins. The magnitude changes with J_0 , but we are only interested in existence of $g(x)$. We plot on a logarithmic scale to hide the magnitude change for the slowly moving piece. 95

7.20 Division of one dimensional space. The Hamiltonian has two delta functions at $x = 0$ and $x = a$ 97

7.21 The weight transferred to the component $g(x)$ from the incoming plane wave component X of $f(x)$. Specifically, the component $|\frac{B}{X}|^2$ is shown. Only the negative energy portion is shown with $a = 1$ and $p = 2$. Two ridges are shown with one much more pronounced than the other. The maximum amplitude occurs for low J_1 98

7.22 The total weight of the component $g(x)$ as generated from the incoming plane wave component X of $f(x)$. Only the negative energy portion is shown with $a = 1$ and $p = 2$. Two ridges are shown following closely with Fig. 7.21. The maximum amplitude occurs for low J_1 99

7.23 z-component of the spin current modeled by a plane wave. For qualitative comparison to Fig. 7.4. The three regions are again present. Low J_1 behavior, very high J_1 and the ridge that is a function of both J_0 and J_1 show similar behavior to wave packet counterparts. There are two ridges instead of one because we have a well defined momentum in this case for the incoming portion of the spin current. 100

7.24 Wave packet spin long after the wave packet interacts with the local spins. Top panel: As a function of both wave packet-spin, J_0 , and spin-spin interaction, J_1 , for 3 local spins. Bottom panel: Slices through J_1 for several constant values of J_0 . Three regions are readily identified. Low J_1 , very high J_1 and the ridges, there are several in this case, that is function of both J_0 and J_1 102

B.1 Three regions for which the coefficients are defined. 118

Chapter 1

Introduction

In this thesis, we look at how fermions interact with one another on an underlying lattice, with the use of two paradigms. We model this interaction to analyze two scenarios that are similar from a computational point of view.

Within the first paradigm, we look at the interaction between fermions in the presence of on-site repulsion and coupling to bosonic states on the lattice. The model we use is an extension of the Hubbard model [1, 2]. In theoretical and computational analysis of electronic structures on a lattice, one of the most utilized models is the Hubbard model. Since its introduction, the model has been used to describe and analyze ferromagnetism [2], antiferromagnetism, superconductivity [3], and the Mott insulator [4, 5]. Due to its simplicity and description of two opposing structures, both ferromagnetic and antiferromagnetic, it has been the choice of many researchers. On the one hand, fermions can move through hopping, on the other hand, when they are on the same site, the system acquires additional energy, describing a short range coulomb repulsion in the simplest possible form. After the discovery of high temperature superconductors [6], to investigate nearest neighbor attraction, an extension to the Hubbard model was proposed, namely the extended Hubbard model [7, 8]. In this new model, in addition to repulsion when two particles are on the same site, attraction is possible when two fermions are on neighboring sites.

The results within the Hubbard model does not show any difference for electrons and holes. In this thesis, we will analyze another extension to the Hubbard model. The same interaction will have different effects for electrons and holes.

On a lattice, one would expect fermions, in this case electrons or holes, to move around through hopping constituting the conduction band. The lattice points are defined as the locations that the electrons spend most of their time before continuing their movement. Due to Bloch's theorem, electrons delocalize and can spend time at any lattice point. The lattice point is also the location of the atom that forms

the lattice. This atom has core electrons associated with it that are bound to the atom, and orbital the atom in a stationary orbit. These orbitals are determined by the interaction between the nucleus and the electrons and by the Pauli exclusion principle. The core electrons are always present on every lattice point.

The extension to the Hubbard model that we will analyze, namely the dynamic Hubbard model, includes effects due to the deformation of these orbitals caused by the existence of conduction band electrons occupying that site. This gives two possible arrangements of the orbitals with two different energy levels.

We will assume that without any conduction electron present, the core electrons can change from one configuration to the other. We will assume that one configuration would increase the energy of the system (for consistency, zero energy for these two states is assumed to be in the middle so that while one configuration increases the energy of the lattice, the other would decrease it), then when two electrons occupy this site, depending on the shape of the core electrons, the on-site repulsion (due to the original Hubbard model) would be modified.

A family of this extension to the Hubbard model has been proposed. They have been analyzed by the use of site Hamiltonian eigenstates, exact diagonalization of small systems and the world line Monte Carlo method. Recently, Bonadin *et al.* showed that at finite temperature, some indication of extended s-wave can be observed using the Quantum Monte Carlo method (QMC) [12].

In the chapters related to this type of interaction, we analyze a member of explicitly electron-hole symmetry breaking models. In order to see if there is an effective nearest neighbor attraction under very high on-site repulsion, we use the density-matrix-renormalization-group (DMRG) [9, 10] a method to analyze 1D systems with open boundary systems. The DMRG method is a powerful tool to analyze 1D systems. It has been applied to many spin and electron systems. Extensions have been proposed to 2D [11], however the error grows exponentially in this case. One aspect of our model, namely the number of states per site, is the biggest constraint of our approach as computation time that increases considerably with the number of states per site and 8 states per site restricts our ability to perform extremely accurate results that is needed to suppress the exponential growth of the error in 2D.

The second paradigm we will investigate treats the states on the lattice as a small layer that interacts with an itinerant electron. This model is relevant to the interaction of a spin current with a magnetic chain.

The current data storage method in the computer industry is based on information carried by magnetic spins. A magnetic field is applied to set local spins along a certain direction to correspond to a particular binary value. To build these storage devices, a classical understanding of magnetic interactions is used. From a theoretical point

of view, the analysis is generally carried out using the Landau-Lifshitz-Gilbert (LLG) equations [13, 14]. LLG equations are a phenomenological description of magnetic interactions and are modified to accommodate specific conditions. The magnetic layer is modeled by a vector of constant length, and any modification of the vector just modifies the direction of the vector. Interaction with only magnetic field, within LLG formalism, introduces precession and an additional damping term is needed to actually flip the spin. Currently, the analytical form of the equations is disputed [15].

More recently, the use of a spin current instead of the application of a magnetic field was suggested [16, 17]. Use of a spin current would enable the production of smaller storage “bits”, as this would allow much denser storage devices. The introduction of a spin current, consisting of electrons with predetermined spin, expanded the theoretical description to include the quantum nature of the electron. The spin current is modeled with plane waves and the local spins are treated classically by a vector that can be rotated to change the magnetization in this semi-classical picture. The term involving the magnetic field is replaced with the corresponding spin of the spin current. Within this picture, interaction of the spin current and the magnetic layer would lead to a torque of the magnetic layer. Due to this effect, this framework is often referred to as “spin-torque”. Since torque is a part of the spin-torque model, no damping is required to change the orientation of a magnetic layer.

Many of the theoretical investigations today focus on this semiclassical picture as it appears to confirm many expectations [18, 19, 20, 21, 22]. The model, however, oversimplifies the behavior of the local spin. The actual spin flip interaction is, like Kondo scattering, a quantum process and especially for small enough systems, the magnetic layer cannot be simply modeled by a vector. The interaction with the spin current will form entanglement between, or among, the fermions in the spin current and the constituent local magnetic spins which is not part of this picture. A correct framework, in principle, needs to keep entanglement intact although the interaction is present only for a short amount of time.

The improvements to the experimental methods moved the current level of analysis beyond the range of the semi-classical approach. A recent experiment has shown direct measurement of spin-torque and the existence and the importance of inelastic scattering for ferromagnetic layers [23, 24]. It has been shown experimentally that observations can be made on magnetic structures as small as 2 coupled atoms [25]. For these cases, the classical picture of the local spins is not applicable. The classical description assumes many of the local spins, and any quantum effect is lost with the large number of spins.

The model we analyze in this thesis is purely quantum mechanical, and treats the existence of entanglement, inelastic scattering and quantum mechanical properties

of coupled magnetic particles. Previously this model has been utilized to model the interaction of many electrons with a magnetic layer [26], and the effect of a complex potential on entanglement [27]. In a recent analysis, Ciccarello *et al.* [28] have shown that the model and the analysis described here increases the entanglement between an electron and a local spin. Here, we will look at the emergence of a quantum state due to the existence of inelastic scattering which can change the consequences of the spin-flip interaction considerably. We will show that not only numerical results, but also an analytical derivation reveals this behavior. Most of the analysis will focus on the interaction of a spin current with spin-1/2 magnetic objects in one dimension for consistency of the thesis, but an extension to higher values of spin and higher dimensional interactions will be included. To avoid confusion, we will call the particle in the spin current the electron, which will initially have spin-up, and the magnetic layer as local spins or magnetic impurities.

Chapter 2

Models

2.1 Overview

In computational condensed matter physics, researchers aim to understand experimental observations by mathematically modeling effective interactions using the Schrodinger's equation. The operator portion of the Schrodinger's equation is called a Hamiltonian. In electronic systems, depending on the physics involved, many different effective Hamiltonian's can be written. An effective Hamiltonian is supposed to capture the essential physics in the problem of interest. In this thesis, we will focus on the interaction of itinerant fermions with local degrees of freedom. The itinerant fermions are free to move on a lattice, in one dimension in our case.

We will model the lattice using a tight binding model. In this model, atoms or molecules that repeat to form the lattice are used as the positions to which the itinerant fermion can hop, and, depending on the interaction, have different energies. The itinerant fermions are free to move to any point on the lattice, and is represented by the kinetic energy term in the Hamiltonian as:

$$T^{el} = -t_0 \sum_{\mathbf{i}\sigma} (c_{\mathbf{i}+\mathbf{1}\sigma}^\dagger c_{\mathbf{i}\sigma} + c_{\mathbf{i}\sigma}^\dagger c_{\mathbf{i}+\mathbf{1}\sigma}). \quad (2.1)$$

With this term, a fermion with spin σ can move from site \mathbf{i} to $\mathbf{i} + \mathbf{1}$ and vice versa by creation (or annihilation) of it on site \mathbf{i} by the operator $c_{\mathbf{i}}^\dagger$ (or $c_{\mathbf{i}}$). The summation ensures that all possible movements are allowed. t_0 is the hopping amplitude that is in the eV range.

We will focus on two types of fermions. The first type is the electron. These electrons are loosely bound to the atom, and can move around to reduce their energy. Electrons have intrinsic spin, which is $\hbar/2$ (we will use $\hbar = 1$ from now on). Due to Pauli exclusion principle, there can only be one electron with a given spin on each

lattice point. Electrons can have two different spins (spin-up or spin-down). When all lattice points are filled with electrons of a particular spin, we can start removing electrons to introduce the second type of fermion we will be investigating, called a hole. Creation of holes ($d_{i\sigma}^\dagger$) is defined by annihilation of the electron ($-c_{i\sigma}$) at the same site with the same spin. Even though these holes are not tangible particles, they present similar properties to the electrons. They can move on the lattice via the kinetic term:

$$T^{ho} = -t_0 \sum_{\mathbf{i}\sigma} (d_{\mathbf{i}+1\sigma}^\dagger d_{\mathbf{i}\sigma} + d_{\mathbf{i}\sigma}^\dagger d_{\mathbf{i}+1\sigma}) \quad (2.2)$$

that describes repositioning of the electrons so that it appears like the lack of an electron, i.e. a hole, moving on the lattice.

The main interaction between electrons is the Coulomb interaction that states that two electrons repel each other with strength inversely proportional to their separation. In our analysis, we take the most dominant part into consideration, the on-site component of the tight binding model. Since only one electron of each spin can occupy the same site, the Coulomb repulsion is given by the Hubbard term:

$$H^{Hub} = \sum_{\mathbf{i}} U c_{\mathbf{i}\uparrow}^\dagger c_{\mathbf{i}\uparrow} c_{\mathbf{i}\downarrow}^\dagger c_{\mathbf{i}\downarrow}. \quad (2.3)$$

The Coulomb interaction for holes will come out of a mathematical transformation that will be carried out in the next section.

The fermions that we have introduced will be modeled as interacting with local degrees of freedom. The source of the local state will differ depending on the model that is used, but we will model the local degrees of freedom using spins. The nature of the spin might be magnetic or not, but mathematically it will always have two states, up and down. The operators for these two states are S^+ that raises the spin from down to up, S^- that lowers the spin from up to down, and S^z that gives 0.5 if the state is up and -0.5 if the state is down. In addition, we have:

$$\sigma^x = S^+ + S^- \quad (2.4)$$

and

$$\sigma^z = 2 \times S^z. \quad (2.5)$$

The analysis here will be performed in the dilute limit of fermions. For the analysis of dynamic Hubbard model, we will restrict ourselves to two electron or two holes and their interaction each other and the lattice degrees of freedom. For the spin-flip interaction, we will only have one electron, and we will only focus on its spin, interacting with the local degrees of freedom.

2.2 Dynamic Hubbard Model (DHM)

The dynamic Hubbard model in the electron representation reads:

$$\begin{aligned}
H = & -t_0 \sum_{\mathbf{i}\sigma} (c_{\mathbf{i}+1\sigma}^\dagger c_{\mathbf{i}\sigma} + c_{\mathbf{i}\sigma}^\dagger c_{\mathbf{i}+1\sigma}) \\
& + \sum_{\mathbf{i}} \left[\omega_0 \sigma_{\mathbf{i}}^x + g\omega_0 \sigma_{\mathbf{i}}^z + (U - 2g\omega_0 \sigma_{\mathbf{i}}^z) c_{\mathbf{i}\uparrow}^\dagger c_{\mathbf{i}\uparrow} c_{\mathbf{i}\downarrow}^\dagger c_{\mathbf{i}\downarrow} \right]. \quad (2.6)
\end{aligned}$$

To observe that this Hamiltonian is electron-hole asymmetric, we show the transformation from electron Hamiltonian to hole Hamiltonian. We define the hole creation (annihilation) operator as the adjoint of the electron counterpart, $d_{i\sigma}^\dagger = -c_{i\sigma}$ ($d_{i\sigma} = -c_{i\sigma}^\dagger$),

$$\begin{aligned}
H = & -t_0 \sum_{\mathbf{i}\sigma} ((-d_{\mathbf{i}+1\sigma})(-d_{\mathbf{i}\sigma}^\dagger) + (-d_{\mathbf{i}\sigma})(-d_{\mathbf{i}+1\sigma}^\dagger)) \\
& + \sum_{\mathbf{i}} \left[\omega_0 \sigma_{\mathbf{i}}^x + g\omega_0 \sigma_{\mathbf{i}}^z + (U - 2g\omega_0 \sigma_{\mathbf{i}}^z) (-d_{\mathbf{i}\uparrow})(-d_{\mathbf{i}\uparrow}^\dagger)(-d_{\mathbf{i}\downarrow})(-d_{\mathbf{i}\downarrow}^\dagger) \right], \quad (2.7)
\end{aligned}$$

carrying out the multiplication leads to

$$\begin{aligned}
H = & -t_0 \sum_{\mathbf{i}\sigma} (d_{\mathbf{i}+1\sigma} d_{\mathbf{i}\sigma}^\dagger + d_{\mathbf{i}\sigma} d_{\mathbf{i}+1\sigma}^\dagger) \\
& + \sum_{\mathbf{i}} \left[\omega_0 \sigma_{\mathbf{i}}^x + g\omega_0 \sigma_{\mathbf{i}}^z + (U - 2g\omega_0 \sigma_{\mathbf{i}}^z) d_{\mathbf{i}\uparrow} d_{\mathbf{i}\uparrow}^\dagger d_{\mathbf{i}\downarrow} d_{\mathbf{i}\downarrow}^\dagger \right]. \quad (2.8)
\end{aligned}$$

For the kinetic energy term, the term with $-t_0$ in front, we have two operators acting on different sites, and they commute. For the on-site operators, we use the anticommutation relation;

$$\{d_{i\sigma}, d_{i\sigma}^\dagger\} = d_{i\sigma} d_{i\sigma}^\dagger + d_{i\sigma}^\dagger d_{i\sigma} = 1. \quad (2.9)$$

We input this into our equation:

$$\begin{aligned}
H = & -t_0 \sum_{\mathbf{i}\sigma} (d_{\mathbf{i}\sigma}^\dagger d_{\mathbf{i}+1\sigma} + d_{\mathbf{i}+1\sigma}^\dagger d_{\mathbf{i}\sigma}) \\
& + \sum_{\mathbf{i}} \left[\omega_0 \sigma_{\mathbf{i}}^x + g\omega_0 \sigma_{\mathbf{i}}^z + (U - 2g\omega_0 \sigma_{\mathbf{i}}^z) (1 - d_{\mathbf{i}\uparrow}^\dagger d_{\mathbf{i}\uparrow})(1 - d_{\mathbf{i}\downarrow}^\dagger d_{\mathbf{i}\downarrow}) \right], \quad (2.10)
\end{aligned}$$

putting in the definition of density operator,

$$H = -t_0 \sum_{\mathbf{i}\sigma} (d_{\mathbf{i}\sigma}^\dagger d_{\mathbf{i}+1\sigma} + d_{\mathbf{i}+1\sigma}^\dagger d_{\mathbf{i}\sigma})$$

$$+ \sum_{\mathbf{i}} \left[\omega_0 \sigma_{\mathbf{i}}^x + g \omega_0 \sigma_{\mathbf{i}}^z + (U - 2g\omega_0 \sigma_{\mathbf{i}}^z) (1 - n_{\mathbf{i}\uparrow})(1 - n_{\mathbf{i}\downarrow}) \right]. \quad (2.11)$$

We carry the multiplication of density operator terms to get

$$\begin{aligned} H &= -t_0 \sum_{\mathbf{i}\sigma} (d_{\mathbf{i}\sigma}^\dagger d_{\mathbf{i}+1\sigma} + d_{\mathbf{i}+1\sigma}^\dagger d_{\mathbf{i}\sigma}) \\ &+ \sum_{\mathbf{i}} \left[\omega_0 \sigma_{\mathbf{i}}^x + g \omega_0 \sigma_{\mathbf{i}}^z + (U - 2g\omega_0 \sigma_{\mathbf{i}}^z) (1 - n_{\mathbf{i}\uparrow} - n_{\mathbf{i}\downarrow} + n_{\mathbf{i}\uparrow} n_{\mathbf{i}\downarrow}) \right]. \end{aligned} \quad (2.12)$$

We rewrite the equation to separate different contributions.

$$\begin{aligned} H &= -t_0 \sum_{\mathbf{i}\sigma} (d_{\mathbf{i}\sigma}^\dagger d_{\mathbf{i}+1\sigma} + d_{\mathbf{i}+1\sigma}^\dagger d_{\mathbf{i}\sigma}) \\ &+ \sum_{\mathbf{i}} \left[\omega_0 \sigma_{\mathbf{i}}^x - g \omega_0 \sigma_{\mathbf{i}}^z + (U - 2g\omega_0 \sigma_{\mathbf{i}}^z) n_{\mathbf{i}\uparrow} n_{\mathbf{i}\downarrow} \right] \\ &+ \left(\sum_{\mathbf{i}} -2g\omega_0 \sigma_{\mathbf{i}}^z (-n_{\mathbf{i}\uparrow} - n_{\mathbf{i}\downarrow}) \right) \\ &- \left(U \sum_{\mathbf{i},\sigma} n_{\mathbf{i}\sigma} \right) + \left(\sum_{\mathbf{i}} U \right). \end{aligned} \quad (2.13)$$

Looking at the equation above, the last two terms can be omitted. The last term is just a shift in total energy due to the nature of the transformation. The term before the last term is a modification to the chemical potential due to the shift in energy, so they can be discarded from the equation. We use canonical ensemble that does not require the chemical potential to set the density. With the omissions, the main equation, Eq. 4.2 becomes

$$\begin{aligned} H &= -t_0 \sum_{\mathbf{i}\sigma} (d_{\mathbf{i}\sigma}^\dagger d_{\mathbf{i}+1\sigma} + d_{\mathbf{i}+1\sigma}^\dagger d_{\mathbf{i}\sigma}) \\ &+ \sum_{\mathbf{i}} \left[\omega_0 \sigma_{\mathbf{i}}^x - g \omega_0 \sigma_{\mathbf{i}}^z + (U - 2g\omega_0 \sigma_{\mathbf{i}}^z) n_{\mathbf{i}\uparrow} n_{\mathbf{i}\downarrow} \right] \\ &+ \left(\sum_{\mathbf{i}} -2g\omega_0 \sigma_{\mathbf{i}}^z (-n_{\mathbf{i}\uparrow} - n_{\mathbf{i}\downarrow}) \right). \end{aligned} \quad (2.14)$$

In this case, the last term is the additional hole-pseudospin interaction term that was not present for the electron representation. After combining the two terms involving σ_z^i we arrive at the hole representation equation:

$$\begin{aligned} H &= -t_0 \sum_{\mathbf{i}\sigma} (d_{\mathbf{i}\sigma}^\dagger d_{\mathbf{i}+1\sigma} + d_{\mathbf{i}+1\sigma}^\dagger d_{\mathbf{i}\sigma}) \\ &+ \sum_{\mathbf{i}} \left[\omega_0 \sigma_{\mathbf{i}}^x + g \omega_0 (2(n_{\mathbf{i}\uparrow} + n_{\mathbf{i}\downarrow}) - 1) \sigma_{\mathbf{i}}^z + (U - 2g\omega_0 \sigma_{\mathbf{i}}^z) n_{\mathbf{i}\uparrow} n_{\mathbf{i}\downarrow} \right]. \end{aligned} \quad (2.15)$$

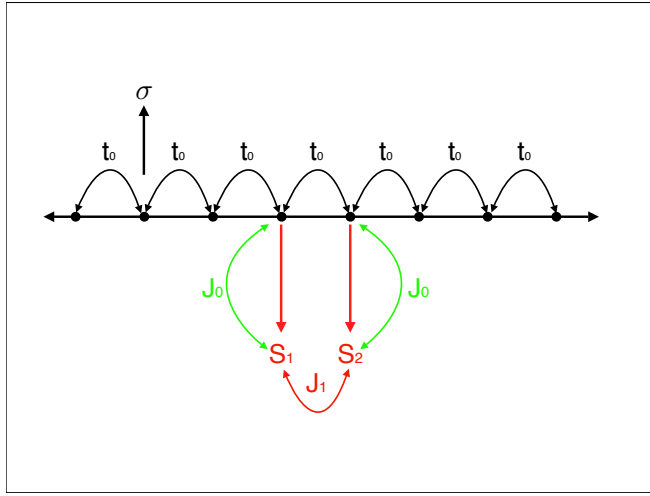


Figure 2.1: The terms of the Hamiltonian, Eq. 7.1 for the scattering of spin current off magnetic layer.

2.3 Scattering of Spin Current From Magnetic Layers

To analyze the scattering of spin current, we look at a Hamiltonian that moves the spin on a lattice. During this movement the spin encounters a stationary coupled magnetic layer. The spin current couples to the magnetic layer through a Kondo-like coupling. In second-quantized notation, the Hamiltonian can be written as:

$$H = -t_0 \sum_{\langle i,j \rangle \sigma} c_{i\sigma}^\dagger c_{j\sigma} - 2 \sum_{l=1}^{N_s} J_0 \sigma_l \cdot \mathbf{S}_l - 2 \sum_{l=1}^{N_s-1} J_1 \mathbf{S}_l \cdot \mathbf{S}_{l+1} \quad (2.16)$$

where $c_{i\sigma}^\dagger$ creates a fermion with spin σ at site i , \mathbf{S}_l is a localized spin operator at site l , t_0 is a hopping amplitude between nearest neighbor sites, so that the spin current can move along the length of the entire chain, and J_0 is the coupling between the spin current and a local spin. Note that J_0 coupling takes place only when an electron is on the site of the local spin. The parameter J_1 is a coupling between two neighboring localized spins as shown in Fig. 2.1. For a ferromagnetic chain, we have $J_1 > 0$.

This model allows inclusion of N_s local spins of size S . These two numbers are independent within the model. For every value of N_s , the total spin is fixed as the model conserves total spin;

$$J_z = \sigma_z + S_z^{tot} = -N_s * S_z + 1/2. \quad (2.17)$$

This symmetry of J_z allows the use of only a small portion of the Hilbert space, resulting in much better computational efficiency.

The energy scale used in this thesis is the hopping parameter t_0 . We set the conditions so that $t_0 = 1$, which sets the energy unit. All other energies are given in units of t_0 .

Chapter 3

Methods

3.1 Density Matrix Renormalization Group (DMRG)

The density Matrix Renormalization Group (DMRG) method was developed by Steven R. White in 1992 [9] while trying to solve a basic problem of Renormalization Group (RG) of Wilson [29]. After this method was introduced, it has been utilized in various fields of physics as a means to reach a quasi-exact solution with approximate states of strongly correlated systems [30, 31]. In this section, a general introduction to the method will be presented.

3.1.1 Terminology:

Within DMRG, several words have specific meanings. We divide the lattice into 3 different areas. There are two blocks containing several lattice points and two (or one in some cases) lattice sites.

System is the part of the lattice that has been approximated by the previous RG (or DMRG) iteration, and is being modified by the algorithm.

Environment is the remaining part of the lattice that hasn't been included in any other part. It has been approximated by an earlier DMRG iteration.

Universe is the entire lattice, including the system, the environment and the two (or one) sites between the parts.

3.1.2 The Methodology:

In the original RG, at each step of iteration, the states with the lowest energies of the previous iterations are used to effectively represent the most probable states of the system. This method was very effective to explain interactions which decrease drastically over distance, such as the Kondo effect in which the interaction dies off exponentially. However when the interaction doesn't have a center or is constant over

all the universe, the method breaks down. One of the reasons for this breakdown is that the RG iteration structure does not process and pass along the boundary conditions correctly in strongly correlated systems. To overcome this problem, Wilson introduced a method that adds one site to the system to form the universe. However, that did not help either. To correctly account for this problem, S. R. White used the following structure [9]: Instead of converting the whole universe into the system for the following iteration, he excluded some part of it and used this excluded part to describe the part that interacts with the system of the next iteration; this part is called the environment. The environment is there so that the system knows how the rest of the universe “most probably” behaves. The environment is set up by an earlier DMRG iteration to include an accurate description of the rest of the universe. This enables us to account for the full interaction. After the system is updated, we need a way to set up the most appropriate basis set. However, since the part we are interested in is interacting with the rest of the universe, we cannot use the basis set of the isolated Hamiltonian of the system. It would not account for the interaction with the environment. We cannot use the basis set of the Hamiltonian of the universe because we are not interested in some part of it. We want to use a part of the universe (system) that interacts with the rest of it (environment) plus the middle site(s). Therefore, we use the density matrix of the system [32], which commutes with the fully interacting Hamiltonian of the system and which can be obtained from the ground state of the universe by the following formula:

$$\rho_{ij} = \sum_k \Psi_{ik} \Psi_{jk}^*, \quad (3.1)$$

where the first index of the ground state of the universe, Ψ_{ik} , corresponds to a state of the system, and the second index to the environment. To explain this structure, the procedure will be described with an example.

We would like to find a property of an infinite size system at zero temperature which is described by the Hamiltonian

$$H = H^o + H^{nn}, \quad (3.2)$$

where H^o describes the on-site interaction and H^{nn} describes the nearest neighbor interaction. In principle, this can be expanded to include next-nearest neighbor and so on. However, since the basic idea is the same, those cases will not be discussed here.

We start with 4 sites as shown in Fig. 3.1. The full Hamiltonian matrix is formed as if we were doing an exact diagonalization calculation. Using a standard

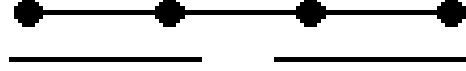


Figure 3.1: First iteration for the DMRG calculation. The two sites on the left will form the system and the two on the right will form the environment.

diagonalization method, we find the ground state eigenfunction. Afterwards, we group each element of the state in terms of the configuration of the first two sites. To elaborate on this, consider the spin-1/2 Ising Hamiltonian as an example. Each site has two states, up or down. The four-site-Hamiltonian has $2^4 = 16$ states. After we find the ground state, we group the 16 states so that each state of, say, left two sites represents one group.

There are a total of 4 states on two sites, namely $|\uparrow\uparrow\rangle, |\downarrow\uparrow\rangle, |\uparrow\downarrow\rangle, |\downarrow\downarrow\rangle$. The remaining two sites have 4 states as well. Any configuration ϕ , including all of these sites using these states can be described by ϕ_{ab} where ‘a’ refers to a state on the left, ‘b’ refers to a state on the right two sites, each running from 1 to 4. Now, we have represented any state of the universe in such a way that it has two indices, where one of them refers to the system, the other to the environment. The same, then, must be true for the ground state, Ψ . Now we can form the density matrix by:

$$\rho_{aa'} = \sum_b \Psi_{ab} \Psi_{a'b}^* \quad (3.3)$$

Returning to the general argument, since the density matrix commutes with the interacting Hamiltonian, the eigenstates of this matrix are eigenstates of the Hamiltonian as well. It is somewhat ambiguous in strongly interacting systems to describe “lowest energy levels” for some part of the universe using the Hamiltonian. However by the definition of the density matrix, the states with the larger eigenvalues are more probable. Therefore, if one chooses the first “m” states with largest eigenvalues, one can accurately, maybe not precisely, represent the system. Using these states, one forms the rectangular matrix O with dimensions m x n, where “n” is the size of the original system Hamiltonian. O has the form:

$$\hat{O}_{ij} = (\phi_i)_j, \quad (3.4)$$

where ϕ_i is the i^{th} eigenstate of the density matrix.

Using this matrix, one projects the system Hamiltonian onto the considered eigenstates of the density matrix by the following:

For reasons of simplicity, only the Ising Model will be shown here, as the model has few elements. Any given Hamiltonian can be written as an on-site interaction part (H^o) and nearest neighbor interaction part (H^{nn}). For the Ising Hamiltonian, for a specific site:

$$H_i^o = 0 \quad H_{i,i+1}^{nn} = S_i^z S_{i+1}^z. \quad (3.5)$$

The four site Hamiltonian can be written as:

$$H = H_1^o + H_2^o + H_3^o + H_4^o + H_{12}^{nn} + H_{23}^{nn} + H_{34}^{nn}. \quad (3.6)$$

Even though, on-site components are zero, for purposes that will be clear later, we keep them. One can put all parts consisting of only indices 1 and/or 2 into an on-site Hamiltonian of the system H_L^o and interactions of these sites with other sites into H_L^{nn} . H_L^o is written in the following way:

$$(H_L^o)_{ii'jj'} = (H_1^o)_{ij}\delta_{i'j'} + (H_2^o)_{i'j'}\delta_{ij} + (S_1)_{ij}(S_2)_{i'j'}. \quad (3.7)$$

Here, ii' and jj' represent one number each. Assuming the leading dimension of the matrix H_2^o is N , the indices are;

$$ii' = (i - 1) * N + i' \quad (3.8)$$

and

$$jj' = (j - 1) * N + j'. \quad (3.9)$$

For spin-1/2 Ising model, $N = 2$. Delta functions are present because we are taking a direct product [33]. If one keeps including more and more sites like this, the calculation would be exact.

Then, we perform the projection operation, using the eigenvectors of the density matrix of the system from the ground state of the universe:

$$(H_L^o)^{new} = \hat{O}H_L^o\hat{O}^\dagger. \quad (3.10)$$

For the part involving the interaction with outside, S^z is operated the same way:

$$(S_L^z)_{ii'jj'} = (S_2^z)_{i'j'}\delta_{ij}. \quad (3.11)$$

Then the projection:

$$(S_L^z)^{new} = \hat{O}S_L^z\hat{O}^\dagger. \quad (3.12)$$

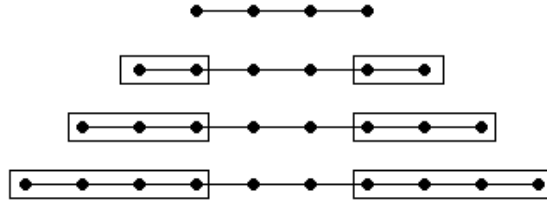


Figure 3.2: Procedure for infinite size systems. At each iteration, the neighboring sites are added to system (or environment) to increase its size by one. This is continued until convergence.

The reason we have only S_2^z is because only the second site is at the border of the group. We do the same for the two sites on the right to expand the environment as well to get operators with subscript R .

Now, we have all the operators we need. We write the Hamiltonian for the universe with the new matrices as:

$$H = (H_L^o)^{new} + H_3^o + H_4^o + (H_R^o)^{new} + (S_L^z)^{new} S_3^z + S_3^z S_4^z + S_4^z (S_R^z)^{new}. \quad (3.13)$$

This Hamiltonian is the same as before, Eq. 3.6, with right-most and left-most sites replaced with the modified states. Now this Hamiltonian describes a universe of 6-sites, two sites in index L, two sites in the middle and two in index R.

We repeat the same DMRG procedure to make the universe 8, 10, 12, 14 sites, as shown in Fig. 3.2, until the increase in size does not change the property that we are looking for, within the error.

3.1.3 Finite Size

If the target size is not infinite, then when the desired size is reached, the size of the universe should be kept constant. How this is to be done is described in Fig. 3.3.

We start with the standard infinite system algorithm. When the desired size is reached, we begin reducing the size of the environment in order to keep the size of the universe constant. There is no systematic way to get a smaller environment from an earlier stage. Therefore, we use the environment we calculated before for the size we need. However, since this smaller size of environment has been formed when the universe was smaller in size, it does not contain the exact information we need. Therefore, after we perform the DMRG iteration for the system, we go back and do the same for the environment. The group of iterations that goes from one end to the other is called a sweep. This is continued until we get to the desired convergence.

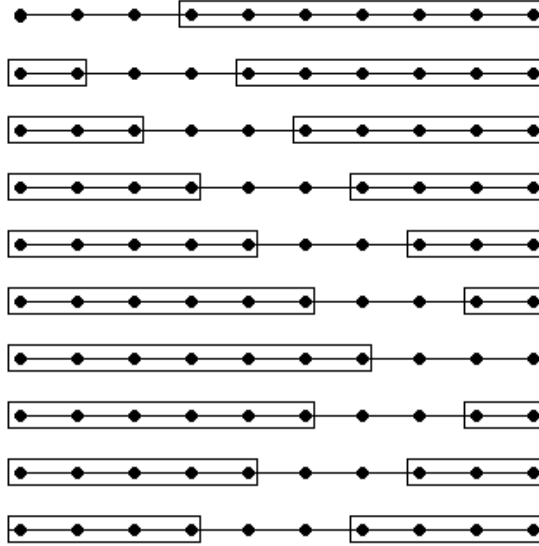


Figure 3.3: Procedure for finite size systems after the system size is reached. When one sweep is completed for the system, it is done for the environment as well.

3.1.4 Calculation of Observables:

Most of the observables we deal with are site-dependent. Therefore, we show the calculation of this type of observables. There are two ways of calculating the observables. Here, we present both of them.

In the first way, after we reach convergence, we perform one more sweep to get the observables. At each iteration, we calculate the expectation value of the observable we are interested in, A_i , using the ground state wave-function of the universe. We calculate the expectation value on one of the sites that we treat exactly for that point of iteration or between the sites,

$$A_i = \Psi^* \hat{A}_i \Psi. \quad (3.14)$$

This way enables us to use an exact operator to get the observable since the site operators are exact. However, this method means that we need to perform an additional sweep, causing the calculation to take longer.

The second method, which was originally suggested by White [33], does all the calculations when the convergence is reached. In this method, we need the observable for each site ready. Therefore, it is important to have the observable in the basis of the block it is in. For instance, for the Ising model, if we are looking for the expectation value of S_i^2 for the second site, from the very first iteration we need to perform the

extension and projection operations;

$$(A_2^1)_{ii'jj'} = \delta_{ij}(S_2^z)_{i'j'} \quad (3.15)$$

$$(A_2^1)^{new} = \hat{O}A_2^1\hat{O}^\dagger. \quad (3.16)$$

For the next point in iteration, we again expand and then project using the corresponding projection operator.

$$(A_2^2)_{ii'jj'} = (A_1^1)_{ij}^{new} \delta_{i'j'} \quad (3.17)$$

$$(A_2^2)^{new} = \hat{O}A_2^2\hat{O}^\dagger. \quad (3.18)$$

that we performed for the parts of the Hamiltonian. This way we keep the operator in the basis set that we work with. When we reach the convergence, we use the following calculation just like we did in the first way:

$$A_i = \Psi^* \hat{A}_i \Psi. \quad (3.19)$$

One needs to pay attention to which part of the universe is being measured. Depending on the location, the summation shown above acquires some changes as shown by White [33].

3.1.5 Variation to Standard Approach

In this thesis, the method is varied from what is described above. As the model we would like to apply has many states in one site, any reduction in the effective number of sites is an improvement in the numerical efficiency. We follow the arguments described in Ref. [50]. In the standard DMRG algorithm, the system and the environment are separated by two sites. As the sweeps are carried out, one of these sites is added to the system, and the other to the environment. Having two sites as a "buffer zone" allows DMRG to account for unconverged properties of the environment by including the fluctuations from the current configuration of the environment.

We have tried to remove the second site in the middle in our calculations. We hope to reduce the size of the Hamiltonian of the universe, by a factor of 8 in case of the dynamic Hubbard model, and therefore reduce the computational time considerably. However, the system converged to a local minimum, not the true ground state.

When the second site is removed, the fluctuations are needed to be taken into account in another way. This is done by allowing the component of the Hamiltonian connecting the edge site of the system (or environment) block to the central site through particle-particle interaction terms to fluctuate. In our case of DHM, only the

hopping term is particle-particle interaction in neighboring sites, therefore, when the density matrix is formed to decide which states are the most important states, the fluctuations are added;

$$\Delta\rho = \sum_{\sigma} c_{\sigma L}^{\dagger} \rho c_{\sigma L} + c_{\sigma L} \rho c_{\sigma L}^{\dagger}. \quad (3.20)$$

With these fluctuations added to the density matrix, the possible ‘‘convergence’’ to a local minimum is prevented, and true convergence is achieved.

3.2 Chebyshev Polynomial Expansions

For time-dependent calculations of a wavepacket and dynamic properties of the dynamic Hubbard model, we will use a series expansion of operators.

3.2.1 General Arguments

For any series expansion, one can define:

$$f(x) = w(x) \sum_{n=-\infty}^{\infty} a_n g_n(x) \quad (3.21)$$

where f is the function we would like to calculate, but having difficulty in its explicit form, g is a set of well defined, complete and, preferably, orthogonal functions and $w(x)$ is a weighting function. The coefficients are then found using;

$$a_n = \int f(x) g_n(x) dx. \quad (3.22)$$

We begin by defining a set of functions that satisfies the mentioned conditions. One set of functions, the Chebyshev polynomials, is given by:

$$g_n(x) = T_n(x) = \cos(n \times \arccos(x)) \quad (3.23)$$

for any value of x in the range $[-1 : 1]$. For weighting function, we will use

$$w(x) = \frac{1}{\pi \sqrt{1-x^2}}. \quad (3.24)$$

The values of this function for a given argument x are:

$$\begin{aligned} T_0(x) &= 1 \\ T_1(x) &= x \\ T_k(x) &= 2xT_{k-1}(x) - T_{k-2}(x) \end{aligned} \quad (3.25)$$

Please note the similarity of the functional form to a Taylor series expansion and the recursion form to a Lanczos iterative structure. As the function, Eq. 3.23, is symmetric with respect to n , Eq. 3.21 is often written as:

$$f(x) = w(x)(a_0 T_0(x) + 2 \sum_{n=1}^{\infty} a_n T_n(x)) \quad (3.26)$$

The coefficients a_n depend on the function being evaluated and can change the structure of the calculation considerably.

In this thesis, we will use the Chebyshev polynomials for calculation of the time evolution of a wavepacket and dynamic properties of the dynamic Hubbard model.

3.2.2 Time Evolution of a Wavepacket

To evaluate the time evolution of a wavepacket, we define the wave packet at any time as:

$$\Psi(t, x) = e^{-i\hat{H}t} \varphi(x), \quad (3.27)$$

where $\varphi(x)$ defines the initial packet that is formed, and $\Psi(t, x)$ the wavepacket at time t and position x . The complicated function we would like to evaluate in this case is:

$$f(\hat{H}) = e^{-i\hat{H}t}. \quad (3.28)$$

This function is very different looking then the form we want, shown in Eq. 3.21. For Chebyshev expansion, we need to make some changes to this function. Firstly, The argument needs to lie in the range $[-1 : 1]$. For this purpose, we make a change of variables:

$$\begin{aligned} f(\hat{H}) &= e^{i\frac{\hat{H}}{\delta}\delta t}, \\ f(x) &= e^{ixy}, \end{aligned} \quad (3.29)$$

where we defined $y = \delta t$, and $x = \frac{\hat{H}}{\delta}$ so that the argument of the function lies in the desired range. Since the argument of the function, x , is a matrix, a modified meaning of normalization is understood. As a series expansion will be carried out, the matrix needs to stay finite for an arbitrary power of the Hamiltonian. For this purpose, we normalize the Hamiltonian matrix so that all eigenvalues of it lie within the desired range of $[-1 : 1]$. Looking at the current way we have defined the function, we realize that it is still impossible to evaluate the expansion function, Eq. 3.23, with the current argument as the argument of the function f is a matrix, not a number. Therefore, we do not use the actual definition of the Chebyshev polynomials, rather the recursion relation, Eq. 3.25, to form the set of expansion functions.

The coefficients in this case can be found by evaluating the integral in Eq. 3.22. The integral becomes:

$$a_n = \int_{-1}^1 \frac{T_n e^{ixy}}{\pi \sqrt{1-x^2}} dx = \int_{-1}^1 \frac{\cos(ncos^{-1}(x)) e^{ixy}}{\pi \sqrt{1-x^2}} dx = (-i)^n J_n(y), \quad (3.30)$$

where $J_n(y)$ is the n^{th} order Bessel function of the first kind. This means that, a complete time evolution can be calculated by storing, in some form, the expansion functions $T_n(x)$ and calculating the wavepacket using the Bessel functions for that particular time, y .

3.2.3 The Dynamic Response Functions

A similar set of arguments can be made for the calculation of the dynamic response functions. The quantity we are interested in is:

$$A_X(\omega) = \frac{1}{\pi} \lim_{\epsilon \rightarrow 0} \text{Im}(\langle \Psi_0 | X^\dagger \frac{1}{\omega - i\epsilon - H} X | \Psi_0 \rangle), \quad (3.31)$$

where $A_X(\omega)$ is the response function of the operator X at frequency ω for the ground state, Ψ_0 of the Hamiltonian H .

Before continuing any further, we realize that we need to normalize the Hamiltonian like we did for the time evolution case, and rewrite the equation as:

$$A_X(\omega) = \frac{1}{\pi} \lim_{\epsilon \rightarrow 0} \text{Im}(\langle \Psi_0 | X^\dagger \frac{1/\delta}{\frac{\omega}{\delta} - i\frac{\epsilon}{\delta} - \frac{H}{\delta}} X | \Psi_0 \rangle), \quad (3.32)$$

or

$$A_X(\omega) = \frac{1}{\pi\delta} \lim_{\tilde{\epsilon} \rightarrow 0} \text{Im}(\langle \Psi_0 | X^\dagger \frac{1}{\tilde{\omega} - i\tilde{\epsilon} - \tilde{H}} X | \Psi_0 \rangle), \quad (3.33)$$

or

$$A_X(\omega) = \frac{1}{\delta} \sum_k \langle \Psi_0 | X^\dagger | k \rangle \langle k | X | \Psi_0 \rangle \delta(\tilde{\omega} - \tilde{E}_k), \quad (3.34)$$

where $\tilde{\omega} = \frac{\omega}{\delta}$, $\tilde{\epsilon} = \frac{\epsilon}{\delta}$, $\tilde{H} = \frac{H}{\delta}$ and $\tilde{E}_k = \frac{E_k}{\delta}$. We will expand this general function in terms of Chebyshev polynomials.

$$A_X(\omega) = \frac{1}{\pi \sqrt{1-\omega^2}} (a_0 T_0(\omega) + 2 \sum_{n=1}^{\infty} a_n T_n(\omega)). \quad (3.35)$$

The coefficients a_n are:

$$a_n = \int A_X(\omega) T_n(\omega) d\omega, \quad (3.36)$$

$$a_n = \int \frac{1}{\delta} \sum_k \langle \Psi_0 | X^\dagger | k \rangle \langle k | X | \Psi_0 \rangle \delta(\tilde{\omega} - \tilde{E}_k) T_n(\omega) d\omega, \quad (3.37)$$

using the properties of the delta function, we find

$$a_n = \frac{1}{\delta} \langle \Psi_0 | X^\dagger T_n(\tilde{H}) X | \Psi_0 \rangle. \quad (3.38)$$

We will use this expansion to calculate two functions, the spectral function and the optical conductivity. For the spectral function, the complete form is

$$A^-(k, \omega) = \frac{1}{\pi} \lim_{\epsilon \rightarrow 0} \text{Im} \left(\langle \Psi_0 | c_k^\dagger \frac{1}{\omega - i\epsilon - H} c_k | \Psi_0 \rangle \right). \quad (3.39)$$

For this function the coefficients of the expansion become

$$a_n = \frac{1}{\delta} \langle \Psi_0 | c_k^\dagger T_n(\tilde{H}) c_k | \Psi_0 \rangle. \quad (3.40)$$

For optical conductivity, the complete form is:

$$\sigma(\omega) = \sum_{k \neq 0} \frac{\langle \Psi_0 | J^\dagger | k \rangle \langle k | J | \Psi_0 \rangle}{E_k - E_0} \delta(\omega - (E_k - E_0)), \quad (3.41)$$

where J is the current operator;

$$J = -it_0 \sum_{i,\sigma} (c_{i,\sigma}^\dagger c_{i+1,\sigma} - H.c.). \quad (3.42)$$

Utilizing the property of the delta function, we can set $E_k - E_0 = \omega$ to rewrite the equation for the optical conductivity as:

$$\sigma(\omega) = \frac{1}{\omega} \sum_{k \neq 0} \langle \Psi_0 | J^\dagger | k \rangle \langle k | J | \Psi_0 \rangle \delta(\omega - (E_k - E_0)). \quad (3.43)$$

Even though the optical conductivity itself would not obey our formalism that was defined for the spectral function due to the additional ω at the denominator, the reduced optical conductivity, $\omega\sigma(\omega)$ would follow the same procedure with $X = J$

$$\omega\sigma(\omega) = \sum_{k \neq 0} \langle \Psi_0 | J^\dagger | k \rangle \langle k | J | \Psi_0 \rangle \delta(\omega - (E_k - E_0)). \quad (3.44)$$

In this case, the coefficients become:

$$a_n = \frac{1}{\delta} \langle \Psi_0 | J^\dagger T_n(\tilde{H}) J | \Psi_0 \rangle. \quad (3.45)$$

In our calculations, the ground state, $|\Psi_0\rangle$, is calculated using the computational package ARPACK. This state is then acted upon by the operator of the response function. We will call the resulting state $|\phi_0\rangle$. As we only need the expectation

value of the Chebyshev polynomials for the coefficients, instead of calculating each polynomial, the resulting vector is used in the following manner:

$$\begin{aligned}
a_0 &= \frac{1}{\delta} \langle \phi_0 | \phi_0 \rangle, \\
|\phi_1\rangle &= \tilde{H} |\phi_0\rangle, \\
a_1 &= \frac{1}{\delta} \langle \phi_0 | \phi_1 \rangle, \\
|\phi_{k+1}\rangle &= 2\tilde{H} |\phi_k\rangle - |\phi_{k-1}\rangle \\
a_{k+1} &= \frac{1}{\delta} \langle \phi_0 | \phi_{k+1} \rangle
\end{aligned} \tag{3.46}$$

In practice, as the $\frac{1}{\delta}$ is common to every coefficient, only the final result of $\omega\sigma(\omega)$ is scaled with it. For any intermediate calculation the factor $\frac{1}{\delta}$ is ignored

3.2.4 Handling the Delta Function

The dynamic response functions are defined in the limit that the infinitesimal imaginary part in the denominator of Eq. 3.31 vanishes. However, in numerical evaluation of these functions, one needs a finite value of ϵ in order to observe the peaks of resulting delta functions as we sweep the frequency values. Every method of evaluation of these functions has its own way of defining this widening function. In Chebyshev polynomials, as the coefficients are the result of delta function integration, the widening is applied to the coefficients

$$\tilde{a}_n = w_n a_n, \tag{3.47}$$

making the equation for expansion:

$$A_X(\omega) = \frac{1}{\pi\sqrt{1-\omega^2}} (w_0 a_0 T_0(\omega) + 2 \sum_{n=1}^{\infty} w_n a_n T_n(\omega)). \tag{3.48}$$

In general, the widening is done via Lorentzian broadening of the delta function. In Chebyshev polynomial expansion, the normalized hyperbolic sine function is used instead

$$w_n = \frac{\sinh(\tilde{\epsilon}N - n\tilde{\epsilon})}{\sinh(\tilde{\epsilon}N)} = \frac{e^{(\tilde{\epsilon}N - n\tilde{\epsilon})} - e^{-(\tilde{\epsilon}N - n\tilde{\epsilon})}}{e^{\tilde{\epsilon}N} - e^{-\tilde{\epsilon}N}} = \frac{e^{-n\tilde{\epsilon}} - e^{-(2\tilde{\epsilon}N - n\tilde{\epsilon})}}{1 - e^{-2\tilde{\epsilon}N}}, \tag{3.49}$$

where N is the cutoff of the expansion. The $\tilde{\epsilon}$ used in the above equation is related to the Lorentzian broadening parameter ϵ through the normalization, $\tilde{\epsilon} = \frac{\epsilon}{\delta}$. For the spectral function, we used $\epsilon = 0.1$ and for the optical conductivity, we have used $\epsilon = 0.25$.

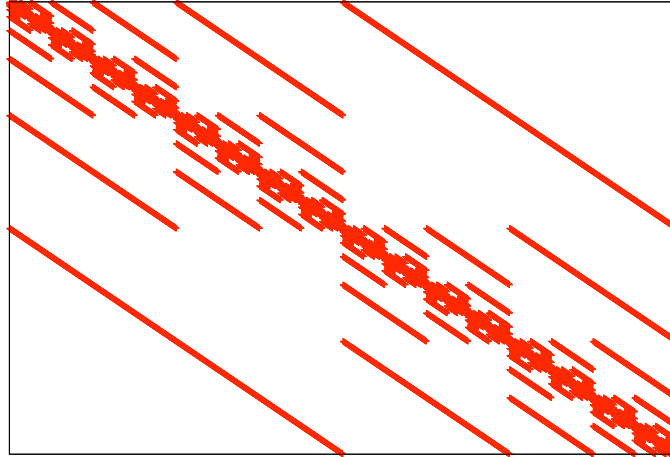


Figure 3.4: The profile of interaction of pseudo-spin basis states within the dynamic Hubbard model. Non-zero elements of the Hamiltonian for this subspace are shown. This particular plot is for a 12 site system.

3.3 Computational Details

3.3.1 DMRG

DMRG relies on iterative analysis of the model on the lattice. Each calculation starts with four (or three in the case of single site DMRG) sites and from the result of this starting lattice configuration, larger lattices are formed. Our model, the dynamic Hubbard model, has a pseudo-spin component that has two states per site in addition to four states of the electron (or hole). The Hamiltonian does not have any symmetry to group these states, as the term $\omega_0\sigma^x$ can change the state of the pseudo-spins in an uncorrelated manner to the pseudo-spin at any other site. A distribution of interaction of the basis states for only pseudo-spin space in the Hamiltonian matrix is given in Fig. 3.4. The pseudo-spins are correlated through their interactions with the itinerant fermions. Extraction of the most probable states through the density matrix formalism is not always accurate and may lead to instability on two fronts.

The first extreme is when the coupling approaches zero. As the coupling is reduced, the communication among the pseudo-spins reduces, making each site independent from the other sites. At this limit, to properly represent each site, one needs both of the states per site, or ALL states of pseudo-spin subspace. This is required because both states are equally important due to the term $\omega_0\sigma^x$. This property renders the density matrix formalism useless as we need to identify a small portion of eigenstates of the density matrix at each iteration.

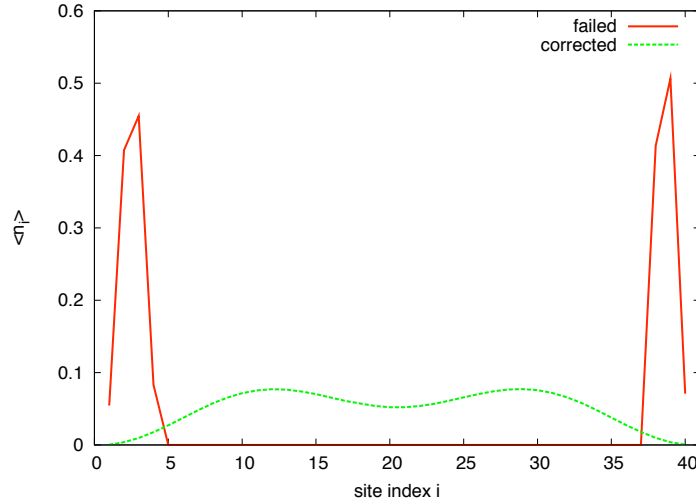


Figure 3.5: The density profile for $U = 16$ and $g = 4.0$. Failed and successful results are shown for comparison.

To avoid non-convergent results, the smallest coupling we use to reference the decoupled fermion-pseudo-spin case is 0.01. At this coupling, though non-zero, we do not expect any qualitative change from the decoupled system.

The other extreme is when both the on-site repulsion, U , and fermion-pseudo-spin coupling are very high. At this extreme, there are two effects that combine to cause computational inaccuracy. For fermions, the high on-site repulsion pushes the particles away from each other and the distribution of density in the ground state is pushed to the edges of the lattice. For pseudo-spins, the basis states that interact with the basis states of the fermions within the dynamic Hubbard model, already pushed to the edge of the lattice, will have the highest contribution to the ground state of the universe. This contribution results in higher eigenvalue, or weight of states with the mentioned configuration. As their presence is weighted for the next point in iteration, the distribution of fermions remains skewed and even though the process is marked as successful by DMRG checks, we identify these runs as failed cases. An example of this “failed” run and the corrected one is given in Fig. 3.5. In these cases, the desired convergence is achieved gradually. First, the on-site repulsion is set to a relatively lower value, and, after one full sweep, the on-site repulsion is increased by a small amount. Another sweep is carried with these parameters. The procedure is repeated until the desired repulsion is reached, and then convergence is sought.

One might argue that all states can be carried with an equal weight for the first few iterations in standard DMRG calculations. However, we have 8 states per site within DMRG, and we cannot carry forward all these states beyond three iterations. This

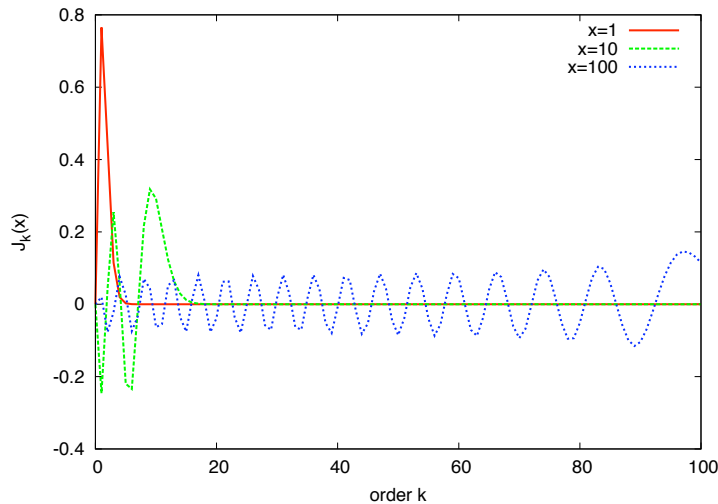


Figure 3.6: The Bessel function evaluated at indicated values over a range of orders.

limits our ability to form large lattices with accurate representation of pseudo-spins in these ranges.

For our calculations, we have kept up to 300 states in the density matrix formalism. We have avoided calculation of absolute values as that requires additional extrapolation [34]. This is not required for any observable we are interested in. We would like to note that as our model has eight states per site, for our largest system, the size of the density matrix is 2400x2400. Of this size, only a fraction of states are kept at each stage.

3.3.2 Chebyshev Polynomial Expansion

In this thesis, the Chebyshev polynomials are used for two different purposes, and since each procedure and coefficients are qualitatively different, the numerical details, and hence the accuracy checks, are different.

For the time evolution of wave packets, we need the order of the polynomials to exist for the order of the Bessel function that is non-zero. Each term in the expansion is multiplied with the corresponding Bessel function of that level. As seen in Fig. 3.6, although for small arguments (in this case corresponding to time) higher order terms are negligible, however, for large arguments, the coefficients are non-zero for a range of orders. This results in the requirement to have higher order terms in the expansion of the Hamiltonian. Ignoring to do so results in failure of the calculation. As our wave packet is normalized, it is easy to detect this failure. Each term in the expansion is orthogonal to the other. Addition of new terms to the expansion makes the normalization satisfied better. If the coefficients, the Bessel functions, are

negligible for these terms, the contribution to normalization will be negligible. If not, we will have, and need, non-zero contribution from these terms to get, and satisfy, normalization of the wavepacket for a given time.

In short, when we do not use enough terms in our expansion of the wave packet, the norm of the wave packet deviates from unity. On the other hand, if we use more than enough terms, the decay in the value of Bessel functions enables us to discard these terms. They do not cause any inaccuracy, theoretically, in calculations, though they would slow down our program.

In addition to longer computational time, using higher order terms in the expansion has undesired effects in the accuracy of the numerical calculation of Bessel functions. The calculation of Bessel functions is carried out iteratively. Our current subroutine cannot calculate the argument larger than 5000 accurately at the moment. So use of higher terms would result in inaccurate results. For time evolution, we have transformed the expansion of the Chebyshev polynomials to have smaller power of the Hamiltonian in the equations as explained in Appendix A. For the use of this trick to have any benefit over the standard expansion, we need to store a relatively dense matrix. For this purpose we have restricted ourselves to have small time expansion, requiring smaller arguments of the Bessel functions. However, the argument of the Bessel function is not the actual time, so the upper limit of time is different depending on the value of the normalization term δ of the Hamiltonian. This is not an acceptable ambiguity. We need to time evolve the wave packet to a certain time for every set of Hamiltonian parameters so that the wave packet travels to the same distance, for the most part, from the local spins. We need this to be able to compare the same quantity for every set. To achieve this, after one set of time evolution, the final wave packet is used as the initial wave packet and the calculation is repeated. We are happy to note that, this additional step only requires a small number of matrix vector multiplications because of the trick we mentioned above.

For the case of the calculation of the dynamical response functions, the level of expansion is determined in a different manner. As mentioned earlier, we are dealing with delta functions. If these functions are not handled accurately, we would have Gibbs oscillations in our results, as seen in Fig. 3.7. These oscillations are artifacts of expansion and can be avoided. To this end, we use a sufficient number of points, up to 100,000, so that we wash out any additional oscillations that might happen, and we form a proper expansion of the delta function, as shown in Fig. 3.7. It is also important to note that the number of points in the expansion depends heavily on the value of ϵ . As ϵ gets smaller, for the same accuracy a higher order of expansion should be used.

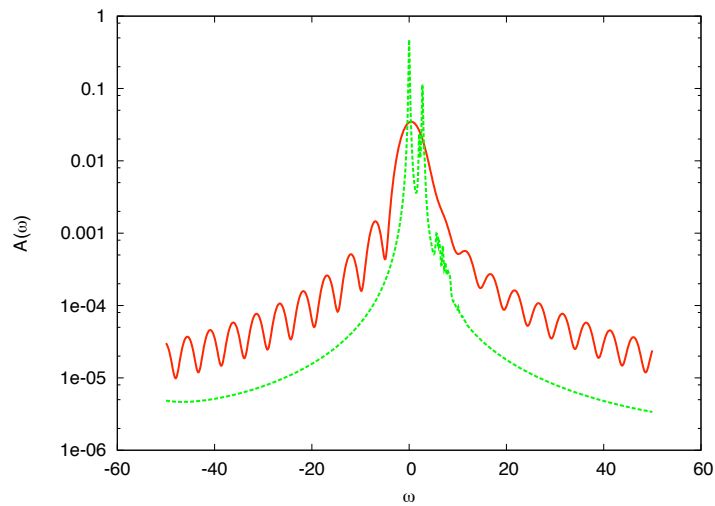


Figure 3.7: The appearance of oscillatory behavior when the expansion is not accurate in the case of the spectral function. Dashed (green) line is as it appears in Fig. 5.3b for $U = 0$ and $g = 3$. The solid (red) curve is an inaccurate representation of dashed (green) curve.

Chapter 4

Static Properties of the DHM

4.1 Introduction

In this chapter, we investigate the possibility of attraction between holes through a member of the dynamic Hubbard model family [35, 36]. The dynamic Hubbard model family is a family of Hamiltonians that can describe electron-hole symmetry breaking, ranging from modulated hopping [37, 38, 39, 40] to background oscillator [41]. We specifically look at the asymmetry through an auxiliary spin degree of freedom [42, 43].

The model, in its general form, investigates the effect of core electron distribution on the fermions that are free to move around the system. The resulting effect is different for holes and electrons. For most cases, electrons experience enhanced repulsion whereas holes experience attraction for some range of coupling [42, 43, 44, 45, 46]. The modulated hopping dynamic Hubbard model, which is the antiadiabatic limit of the pseudo-spin model with $\omega \rightarrow \infty$, has been used to show many of the limiting fermionic results. Kemper *et al.* [47] utilized Density matrix renormalization group to analyze the modulated hopping model for the insulator-superconductor transition. Temperature dependence has been analyzed using transfer matrix density matrix renormalization group [48].

It has been previously shown that single site and small lattices exhibit dressing of holes with the pseudo-spin with the use of exact diagonalization and world-line Monte Carlo [44]. Quantum Monte Carlo has been used to investigate the pseudo-spin Hamiltonian to show attraction in the extended s -wave pairing vertex [12]. A variation of pseudo-spin Hamiltonian was used to show that energy of the pseudo-spin enhances the tendency towards superconductivity [46].

This chapter is arranged as follows: in Section 4.2, we introduce the model, in Section 4.3, we look at the dynamic Hubbard model (DHM) and Hubbard model for density profile and correlation functions of density, in Section 4.4, we look at relative

positions, we conclude with discussion in Section 4.5.

4.2 Model

One of the most popular Hamiltonians used in theoretical condensed matter physics is the Hubbard model:

$$H = -t \sum_{\langle i,j \rangle \sigma} (c_{j\sigma}^\dagger c_{i\sigma} + c_{i\sigma}^\dagger c_{j\sigma}) + \sum_{\mathbf{i}} U n_{i\uparrow} n_{i\downarrow}, \quad (4.1)$$

where electrons, or holes, are free to move on a lattice, but it costs the energy U to have two of these fermions on the same site.

The dynamic Hubbard model for the electrons can be written, in canonical form as,

$$\begin{aligned} H = & -t \sum_{\langle i,j \rangle \sigma} (c_{j\sigma}^\dagger c_{i\sigma} + c_{i\sigma}^\dagger c_{j\sigma}) \\ & + \sum_{\mathbf{i}} \left[\omega_0 \sigma_{\mathbf{i}}^x + g\omega_0 \sigma_{\mathbf{i}}^z + (U - 2g\omega_0 \sigma_{\mathbf{i}}^z) n_{i\uparrow} n_{i\downarrow} \right], \end{aligned} \quad (4.2)$$

which becomes

$$\begin{aligned} H = & -t \sum_{i,\sigma} [d_{i\sigma}^\dagger d_{i+1,\sigma} + h.c.] + \sum_i \left[(U - 2g\omega_0 \sigma_z^i) n_{i\uparrow} n_{i\downarrow} \right. \\ & \left. + \omega_0 \sigma_x^i + g\omega_0 (2(n_{i\uparrow} + n_{i\downarrow}) - 1) \sigma_z^i \right], \end{aligned} \quad (4.3)$$

in the hole representation. In this Hamiltonian, the first term refers to hopping of the holes (t will be our energy unit from now on for any other energy parameter), σ_x , σ_z refer to corresponding Pauli matrices, ω_0 is the energy difference of having two different type of orbitals, g is the dimensionless coupling constant of the spins to fermions.

This Hamiltonian reduces to the modulated hopping dynamic Hubbard model as ω_0 approaches infinity. The modulated hopping Hamiltonian has already been analyzed with DMRG [47, 49]. The way the coupling works is through two parameters, g and ω_0 . For electrons, as seen in equation 4.2, there is only modification to the on-site repulsion via σ^z . On the other hand, holes couple to the pseudo-spins through both single and double occupancy.

We look at the possibility of pairing between two holes. Therefore, we will restrict our analysis to the interaction between one spin up and one spin down hole. We will calculate several quantities to observe the competition between the on-site repulsion and hole-spin interaction.

We will use the DMRG formalism with the single-site algorithm [50] in canonical form. Since DMRG is best suitable for 1D systems, we will look at correlations in 1D. All the calculations presented here are DMRG results with up to 300 states kept at each DMRG update.

4.3 Density Profile

In order to understand how holes behave under the interactions of the dynamic Hubbard model, we first look at the location of the holes individually as a function of interaction parameters,

$$\langle n_i \rangle = \langle n_{i\uparrow} \rangle + \langle n_{i\downarrow} \rangle = \langle \psi_0 | c_{i\uparrow}^\dagger c_{i\uparrow} | \psi_0 \rangle + \langle \psi_0 | c_{i\downarrow}^\dagger c_{i\downarrow} | \psi_0 \rangle, \quad (4.4)$$

where $|\psi_0\rangle$ is the ground state of the lattice.

Since the purpose of this exercise is only to observe the location of the particles, we go to extremes for the on-site repulsion. Unless noted otherwise, the frequency of the spins is $\omega_0 = 0.5$. The Hamiltonian treats each site equally within the system, except for the edge points due to open boundary conditions. Therefore, we expect the solution for the density operator to be symmetric.

We use open boundary conditions since DMRG works better with it. Simple quantum mechanics tells us that particles will want to stay away from the end points, giving the final result of a particle-in-a-box function for the non-interacting case as shown in an earlier analytical work [51].

We start with the Hubbard model. Firstly, we show the result for 20 sites in Fig. 4.1. There is qualitatively no difference between this and any bigger system. In Fig. 4.2, we show the same calculation for 40 sites. Since there is no qualitative change after the system size is doubled, we conclude that the system size of 40 is large enough to see large scale effects. As seen in Figs. 4.1 and 4.2, for a non-interacting system we recover the particle-in-a-box result since the profile follows $\sin^2(i/(Ns+1))$, whereas for increasing on-site repulsion within the Hubbard model, we see that the holes want to avoid the centre, still preserving its parity symmetry. The symmetry is preserved for any on-site repulsion (we plot the total of the spin up and the spin down to symmetrize the density profile). The change is continuous and structureless, and therefore does not tell us much about the details of the system. As the on-site repulsion increases, the preferred location moves from the centre of the system (site 20) to the centre of each half, Fig. 4.4. For identifying the extreme conditions, very high on-site repulsion cases are plotted in these figures. We show that even for very large on-site repulsion, the weight at the centre of the system does not diminish to

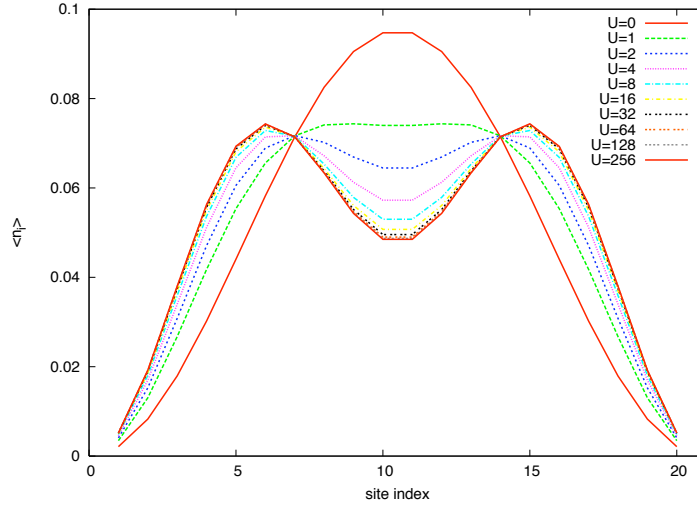


Figure 4.1: Density profile of the Hubbard model for 20 sites. The profile is valid for both electron and hole.

zero. For our analysis, we will focus on much smaller values, shown in Fig. 4.3.

At this point, we turn on the electron-spin interaction. For two electrons, Fig. 4.5, the effective repulsion is enhanced considerably due to the electron-spin interaction, and the well-defined two peaks for any value of the on-site repulsion can be interpreted as electrons staying far away from each other. When we look at the interaction of two holes, the behavior is very different. We see an effective reduction of the on-site repulsion, in Fig. 4.6 for finite U . This does not, however, show us whether or not the effect of coupling to spins leads to a reduction of the effective on-site repulsion. The dip that is supposed to occur as the on-site repulsion is increased is reduced for small values of hole-spin interaction and, for intermediate to strong coupling, the peak is enhanced further with the introduction of the on-site repulsion.

We look at these profiles in detail to compare the effect of the on-site repulsion and hole-spin coupling. Firstly, there is no difference between weak and strong coupling for very high on-site repulsion, Fig. 4.7a, as the order of magnitude difference between the coupling and the on-site repulsion renders any effect of coupling ineffective. For very low on-site repulsion, when the coupling approaches unity, the holes are pushed to the centre of the system, forming a more concentrated peak.

Neither of the cases described above is crucial to the validity of the proposed attraction between the holes. The extreme values of the on-site repulsion is not within the range of attraction in the dynamic Hubbard model. The range of interest is intermediate to strong on-site repulsion. These very strong on-site repulsion cases are given as a reference to what happens at very large on-site repulsion.

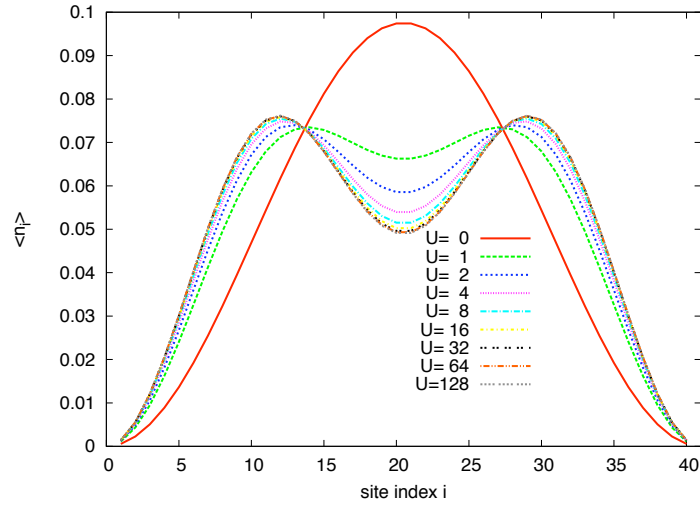


Figure 4.2: Density profile of the Hubbard model for 40 sites, very low to very large on-site repulsions. The profile is valid for both electron and hole.

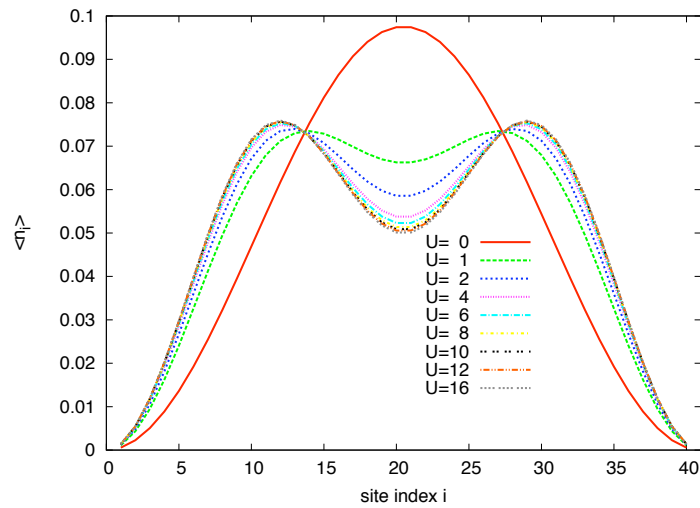


Figure 4.3: Density profile of the Hubbard model for 40 sites, using realistic on-site repulsions. The profile is valid for both electron and hole.

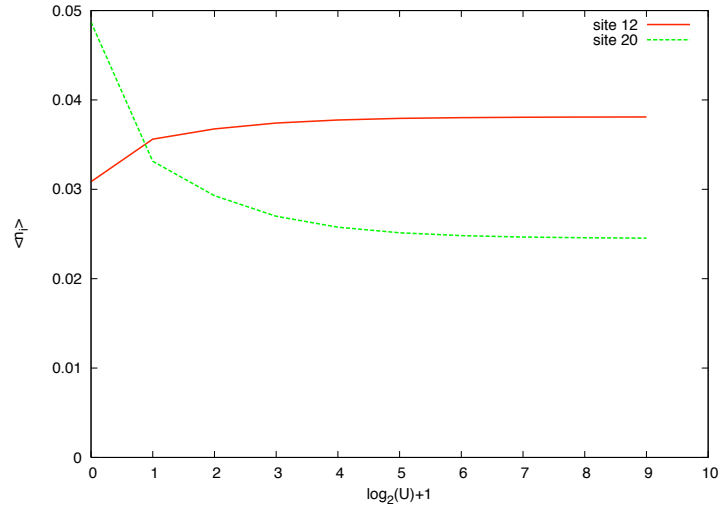


Figure 4.4: Change in the magnitude of the density for centre of the system (site 20) and centre of half system (site 12). The profile is valid for both electron and hole.

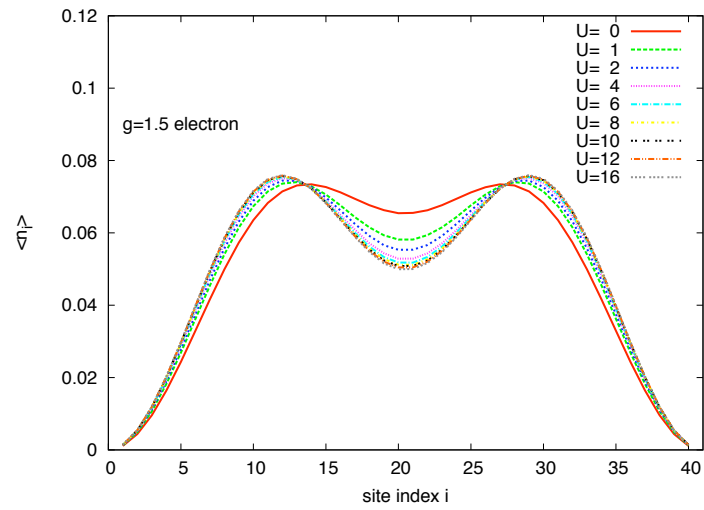


Figure 4.5: Density profile for DHM for electrons.

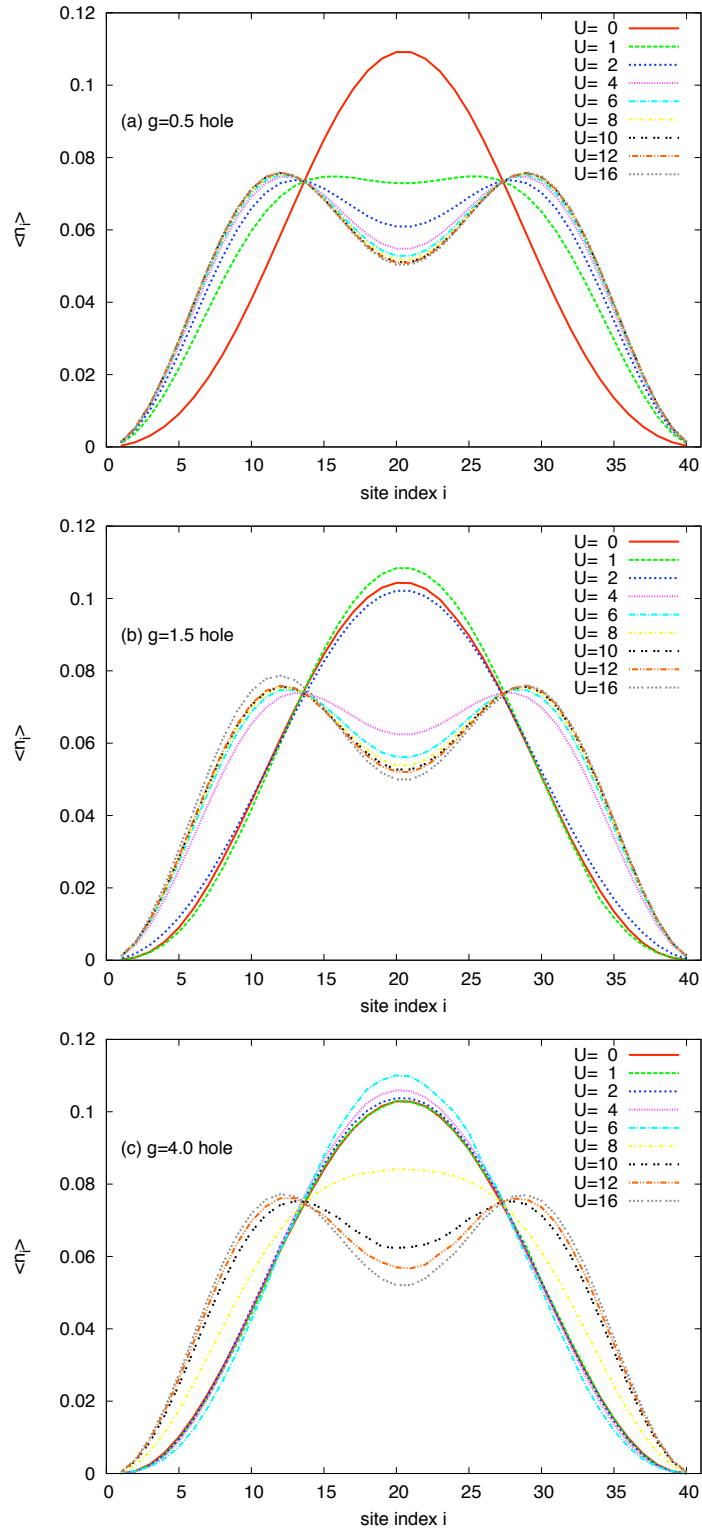


Figure 4.6: Density profile for DHM for holes for coupling constants a) $g = 0.5$, b) $g = 1.5$ and c) $g = 4.0$. Note the similarity of weak coupling (a) to the Hubbard model.

Two values for very low and very high on-site repulsion are plotted in Figs. 4.7b and c, respectively. For low value, $U = 4$, the dip and humps are slowly replaced by the concentrated peak at the centre. We see a distinction between weak and strong coupling. For high value of the on-site repulsion, $U = 16$, the strength of the repulsion is slightly reduced, and only for strong coupling.

The density profile shows that introduction of the hole-spin coupling gives rise to some interaction resulting in the change in shape, however, it does not prove the existence of pairing or give any indication to the mechanism or details of it. On the other hand, it shows that introduction of the on-site repulsion, for on-site repulsion less than $g\omega_0$, in the presence of hole-spin coupling exhibits a more concentrated peak indicating enhancement of attraction with the introduction of the on-site repulsion.

4.4 Relative Positions of the holes

To understand the details of an effective attraction between the holes, we will look at the relative positioning of the holes. When there is repulsion, holes would want to stay away from each other. In case of attraction, they will tend to form some kind of correlation.

We first show the density-density correlation function for several sites

$$\langle n_i n_j \rangle = \langle \psi_0 | c_{i\uparrow}^\dagger c_{i\uparrow} c_{j\downarrow}^\dagger c_{j\downarrow} | \psi_0 \rangle + \langle \psi_0 | c_{i\downarrow}^\dagger c_{i\downarrow} c_{j\uparrow}^\dagger c_{j\uparrow} | \psi_0 \rangle. \quad (4.5)$$

A way to look at this correlation function is to see the magnitude of the correlation, though not normalized, as the probability of finding one hole at a certain site, i , given that the other one is at a reference point, j . From now on, this view will be taken. The correlation function will be calculated with respect to a reference site.

With open boundary conditions, the density profile is very site dependent. This changes the result of the correlation function. However, each site interacts with any other site only once. This improves the relevance of our results. For instance, with open boundary conditions, if we are looking for correlation between sites 5 and 35 on a 40 site system, the correlation function will show the correlation of particles 20 sites apart. If we were to use periodic boundary conditions, the same correlation function would show this point as 10 sites apart rather than 20s site apart due to the connection of the left-most site to the right-most site.

We repeat the same analysis as for the density operator to see how the effects of the on-site repulsion and hole-spin interaction can be observed for the three Hamiltonians mentioned, Eqs. 4.1, 4.2, and 4.3.

We again perform the calculations for a 40-site system, as this system is big

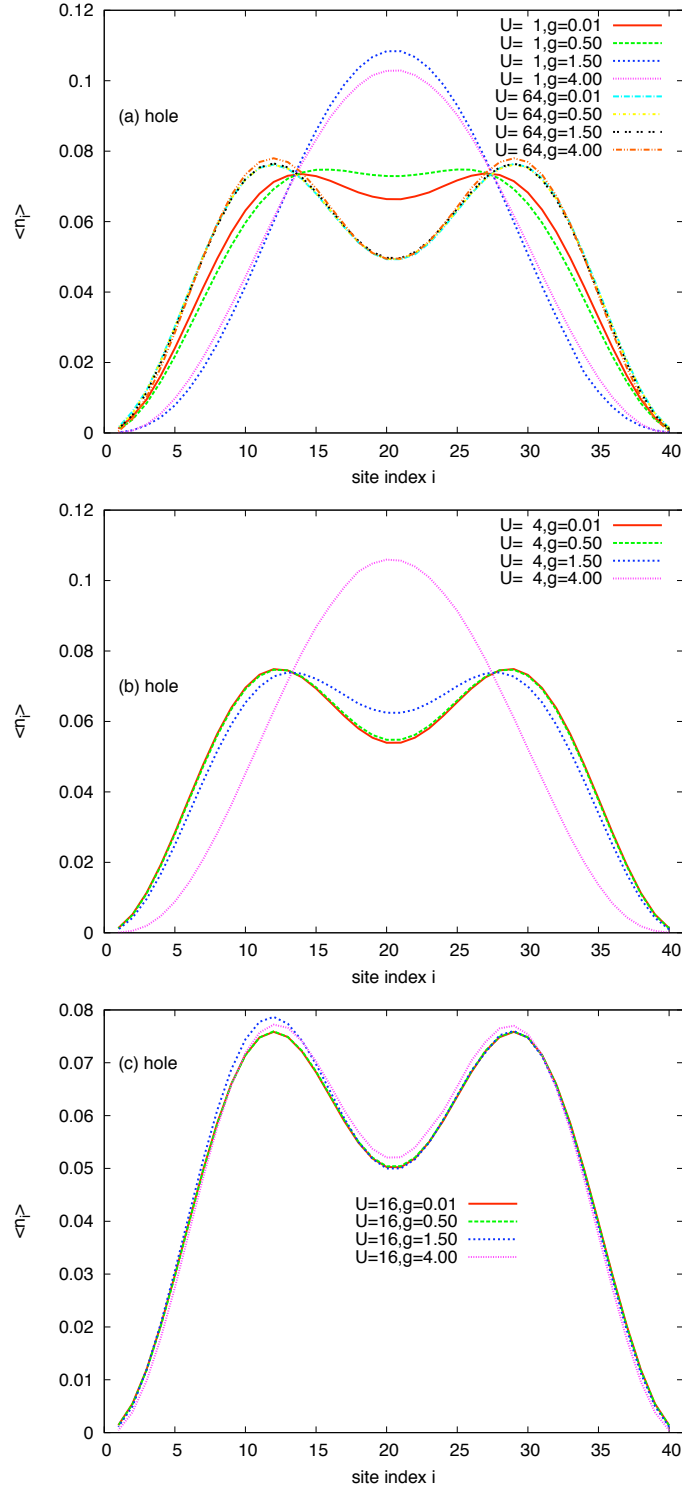


Figure 4.7: Density profile for holes interacting via the dynamic Hubbard model. a) Extreme values of on-site repulsion for the onset of attraction (peaking) and repulsion (splitting) for different on-site repulsion. $g = 0.01$ is essentially identical to the Hubbard model. b) With increasing g , attractive behavior is observed for $U = 4$. c) When $U = 16$, we see effective repulsion for every coupling plotted.

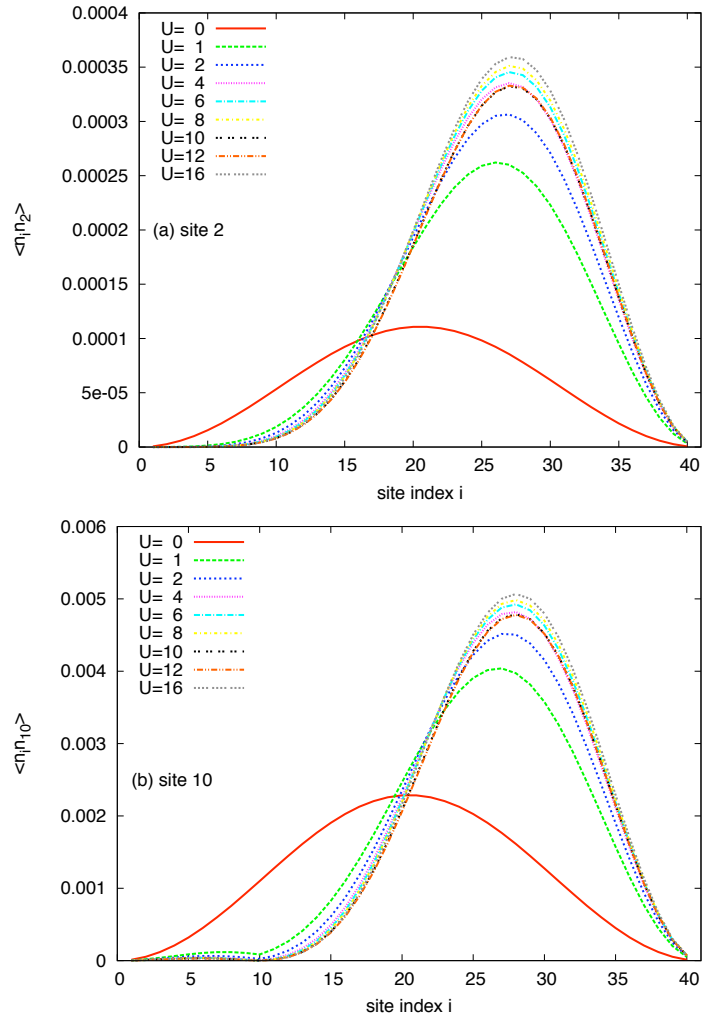


Figure 4.8: Density-density correlation function for a 40-site system for the Hubbard model, for a) site 2 and b) site 10. The correlation is valid for both electrons and holes.

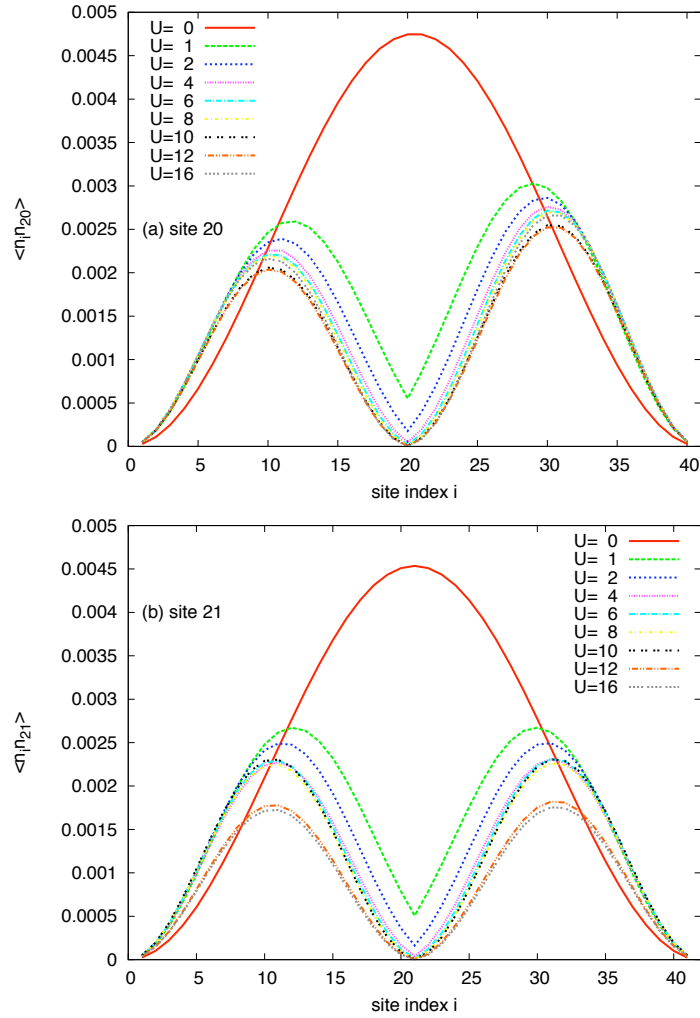


Figure 4.9: Density-density correlation function for a) site 20 of a 40-site and b) site 21 of a 41-site system for the Hubbard model. The correlation is valid for both electrons and holes.

enough to see the effects in the thermodynamic limit. We first look at the case with only on-site repulsion, the Hubbard model. We would like to establish how the holes, or electrons, behave under this potential and then observe the changes the fermion-pseudo-spin interaction cause with the dynamic Hubbard model. For the non-interacting system, $U = 0$, we see in Figs. 4.8, 4.9 that we recover the density profile, Fig. 4.3, with amplitude changed due to an additional density multiplier. This shows that there is no correlation between the holes when the interaction is zero, as expected.

As we turn on the on-site repulsion, the on-site contribution to the correlation function reduces, and becomes zero as $U \rightarrow \infty$. There are two different regimes for different locations of the reference hole. In Fig. 4.8, the reference hole is away from centre of the system, whereas for Fig. 4.9, the reference point is almost at the centre.

When the reference is at one side of the system, the correlation function shows that as the on-site repulsion increases, the other hole does not want to be on the same site as the reference hole. As the cost of being on the same site increases, the other hole pushes itself further away. The maximum of the correlation is pushed to the other half of the system. This is one of the reasons for getting a dip at the centre of the density profile, Fig. 4.3. For the two particular examples shown in Fig. 4.8, the probability of finding the other hole at site 27 and 28 is maximum given that one of the holes is at site 2 and 10 respectively, for large U . In Fig. 4.9, the maximum probability occurs at site 31 for a reference site of 20. Even though the reference point changes through the half of the system, the location of the other hole barely changes. This behavior can be explained by looking at the density profile.

For very large on-site repulsion, the density profile, Fig. 4.3, shows two peaks with a dip in the middle. The two peaks correspond to the locations of the maximum of the correlation function since the overall density profile affects the correlation function.

For site 20, there is an additional probability for finding the other hole in the same half as the reference hole. In Fig. 4.9, the same calculation is performed for a system of 41 sites to see this effect for the centre site (site 21). As the on-site repulsion increases, two peaks form on either side of the system, following the shape of the density function, showing that there is no preferred side for the other hole. For very large values of U , two smaller systems form. However, the separation from the reference site does not reach the values it does for the other reference sites, as the system is divided into the two smallest possible subsystems. Therefore, it is not favorable for the hole at the reference site to be at the centre of the system. This is another reason for the dip at the centre of the density profile of the system, Fig. 4.3.

In Fig. 4.10, we show the same plot for the site 21 for two electrons interacting

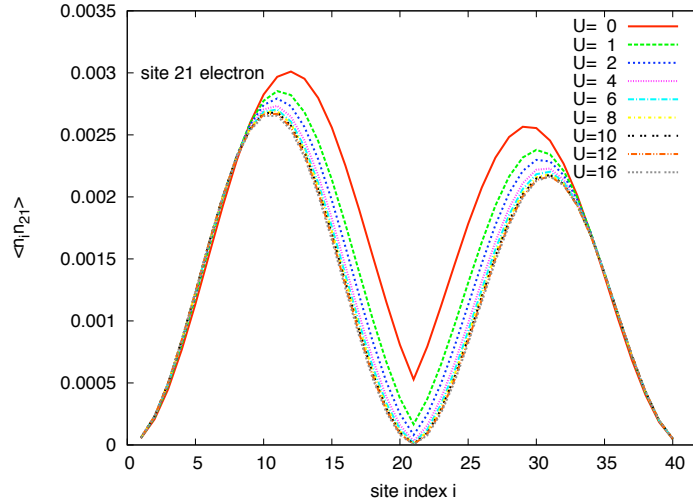


Figure 4.10: Density-density correlation function of a 40-site system for the dynamic Hubbard model for electrons, $g = 1.5$.

via the dynamic Hubbard model. The dip at the reference site is present even for zero on-site repulsion and the increase of the on-site repulsion enhances this effective repulsion. When we look at the interaction of the holes, the behavior is very different than the electrons of the dynamic Hubbard model, as seen in Figs 4.11 and 4.12. For zero on-site repulsion, we get a peak forming at the reference site for all finite values of hole-pseudo-spin interaction. As the on-site repulsion is introduced, we see different behavior depending on the strength of the hole-pseudo-spin interaction. For weak coupling, $g = 0.5$, the repulsive behavior dominates even for $U = 1$, pushing the other hole to the other half of the system. For intermediate to strong coupling, the repulsive behavior is observed strongly for the on-site component, whereas the nearest neighbors attract some of the weight and form the peaks seen in Figs 4.11 and 4.12.

The introduction of the on-site repulsion effectively produces a nearest neighbor attraction. For strong coupling, $g = 4$, the peaks on the nearest neighbors and the dip for the on-site interaction are very pronounced and persist for a range of U . The formation of a nearest neighbor peak and its enhancement with the increasing on-site repulsion is the first indication that the existence of hole-pseudo-spin interaction not only reduces the effective on-site repulsion, but also uses U to enhance the nearest neighbor attraction.

For the systems shown in Figs 4.11, 4.12, the overall magnitudes of the correlation function are different depending on the reference site, and so is the behavior. Depending on which sites are surveyed, the density profile affects the results. We would like

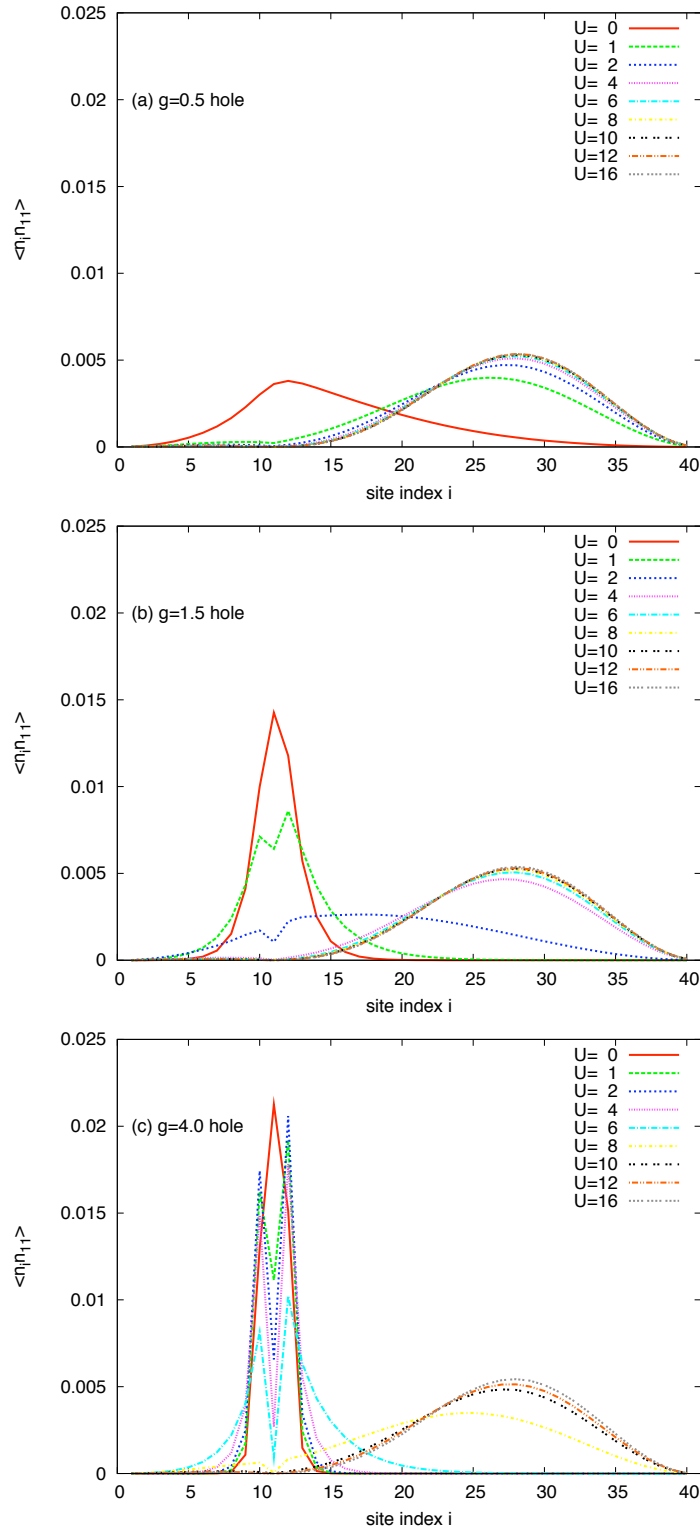


Figure 4.11: Density-density correlation function of holes for site 11 in a 40-site system for the dynamic Hubbard model for a) $g = 0.5$, b) $g = 1.5$ and c) $g = 4.0$. For intermediate (b) and strong coupling (c), formation of nearest neighbor peaks, though non-symmetric, is observed.

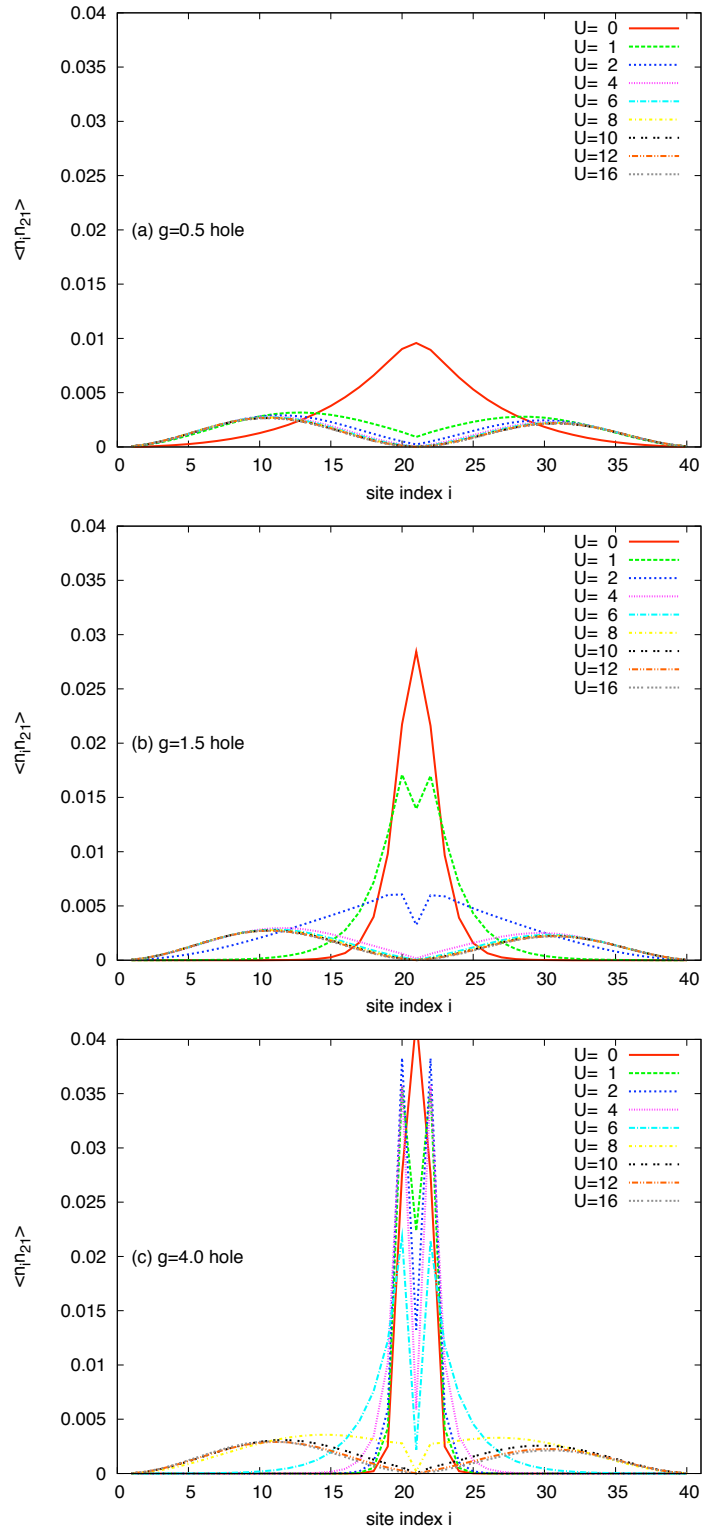


Figure 4.12: Density-density correlation function of holes for site 21 of 40-site system for the dynamic Hubbard model for a) $g = 0.5$, b) $g = 1.5$ and c) $g = 4.0$. Values are larger with respect to Fig. 4.11 since the reference site is much closer to the higher density region.

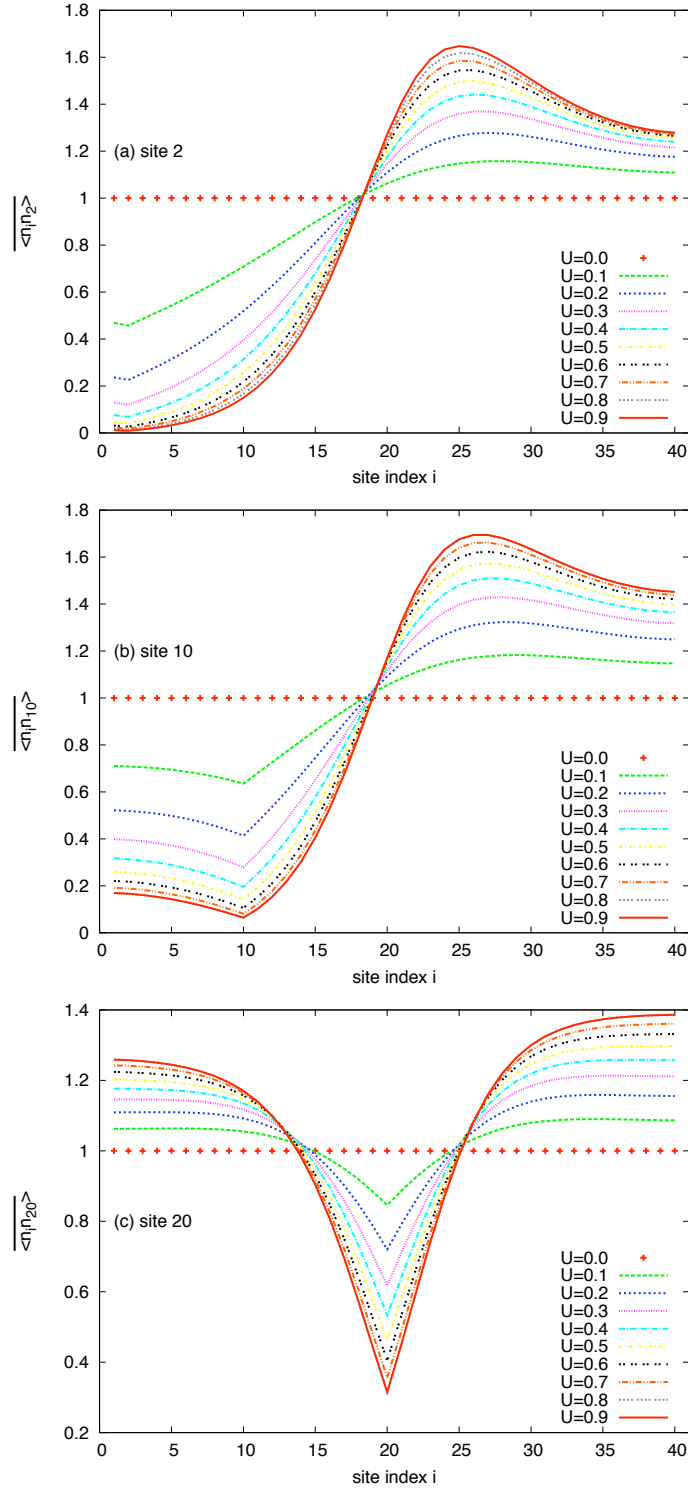


Figure 4.13: Normalized density-density correlation function (see text) for the Hubbard model for the onset of the on-site repulsion for a) site 2, b) site 10 and c) site 20. The density-density correlation function is divided by the the value of the density at the reference site and at the site it is measured. The results are valid for both electrons and holes.

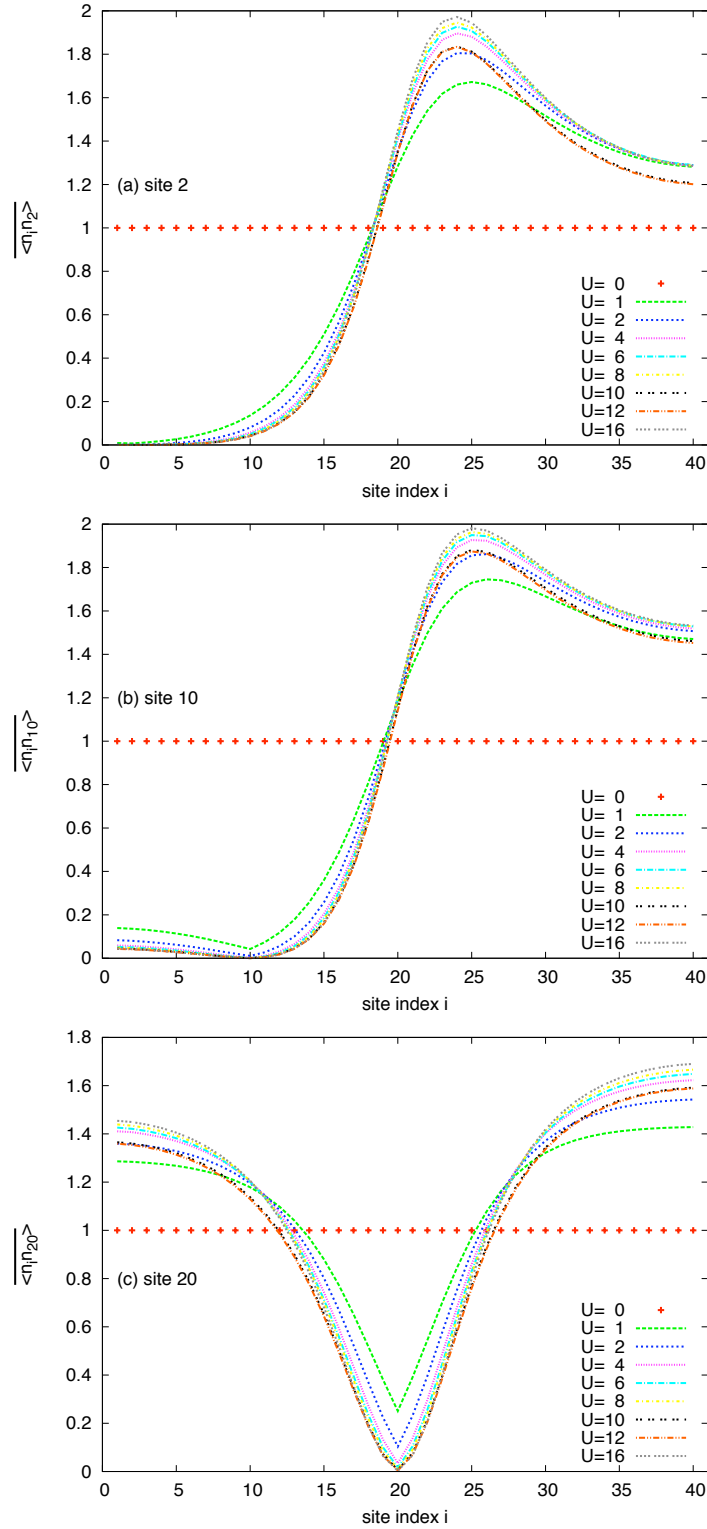


Figure 4.14: Normalized density-density correlation function (see text) for the Hubbard model for a) site 2, b) site 10 and c) site 20. The density-density correlation function is divided by the the value of the density at the reference site and at the site it is measured. The results are valid for both electrons and holes.

to investigate the behavior of holes with respect to each other, and not how density profile affects their behavior. To eliminate this unwanted feature, we examine the normalized version of the function:

$$\overline{\langle n_i n_j \rangle} = \frac{\langle \psi | n_i n_j | \psi \rangle}{\langle n_i \rangle \langle n_j \rangle}. \quad (4.6)$$

This function is unity if there is no correlation between the particles, less than unity if there is an effective repulsive interaction, and larger than one if there is an effective attractive interaction close to the reference site. On the other hand, away from the reference site, this function is larger than unity if there is an effective repulsive interaction, and less than one if there is an effective attractive interaction.

For completeness and consistency, we start with the simple Hubbard model, in Figs. 4.13 and 4.14. For zero on-site repulsion, we observe the function to be one. For small values of on-site repulsion, Fig. 4.13, the weight at the reference site drops and the sites on the other side of the system attain a weight larger than one. As the reference site moves towards the middle of the system, the weight on the same side as the reference site, though still away from the reference site, increases. For values of on-site repulsion comparable to Figs. 4.8 and 4.9, the decrease at the reference site is apparent and more pronounced compared to unnormalized case. The biggest change occur at the onset of the interaction.

In Fig. 4.14, we see that as the on-site repulsion is increased, the probability of finding both fermions on the same site decreases rapidly, as expected. For very large values of the on-site repulsion, the correlation becomes that of two repelling particles and pushed to opposite halves of the system. The first effect to notice is the maximum value of the function as a function of site. Even though it does not change for the regular correlation function, Fig. 4.8 and 4.9, the site with the maximum amplitude moves further and further as the reference point moves toward the centre. The peak is split and the height, and so the probability of finding the other hole on the other side of the system, is reduced in magnitude. The behavior for the case where the reference site is in the middle of the system is very different than the sides. This is consistent with the conclusion that particles are confined in smaller systems. The maximum increase as a function of the on-site repulsion happens for the smallest probability (edge) points, resulting in maximum increase in the normalized correlation function. Any apparent finite size and open boundary condition effect is suppressed, but the location and the height of the peak still show dependence on the system size, as there is a limit for the fermions to push each other.

From this point on, we will omit the electron case for the dynamic Hubbard model because we have already established that the dynamic Hubbard model gives enhanced

repulsion for the interaction of electrons.

We show, in Figs. 4.15 and 4.16, the same results as Figs. 4.11 and 4.12 with the corresponding normalization factors, but for holes interacting via the dynamic Hubbard model. We see that for any hole-spin coupling plotted, for large enough on-site repulsion, the on-site repulsion dominates and therefore the correlation function is qualitatively similar to that of the Hubbard model. In relatively smaller on-site repulsion, the peaks are very well established, especially in the strong coupling regime. Without on-site repulsion, the holes are highly correlated to stay together. We observe the peak in the correlation function to be quite wide, making it difficult to assess if the attraction, the well established peak, is on-site or longer ranged. As the on-site repulsion is increased, the holes are pushed apart. The level of influence of the on-site repulsion depends on the hole-pseudo-spin coupling. For weak coupling, with the introduction of the on-site repulsion, any attraction disappears, whereas for intermediate to strong coupling a well formed nearest neighbor peak occurs. For the strong coupling case, the formed nearest neighbor peak is enhanced with the introduction of the on-site repulsion, and gets stronger for a small range of U , when it is increased as seen in Fig. 4.15c and 4.16c.

The picture drawn here so far is very much site-dependent. In order to understand how the holes are affected by the attraction, it is important to look at the correlation as a function of relative distance. We define the relative positioning of the holes by the total density-density correlation function for a certain distance of the holes over the entire system as:

$$F(j) = \sum_i \langle n_{i \pm j} n_i \rangle, \quad (4.7)$$

with the condition that each site must be contained within the system.

One way to look at this function is as the separation distance of the two holes. Since the definition of the function sums over all sites, the site dependent properties are averaged over. The Hubbard model doesn't have any interaction other than repulsion and therefore separation, the average distance will gradually increase with increasing on-site repulsion, and therefore results for only the dynamic Hubbard model are plotted in Fig. 4.17.

Since the range of j depends on the system size, the large on-site repulsion limit will be represented poorly. On the other hand, the resulting attraction is over a few sites, and the point of this calculation is to see this attraction for the overall system. The system size is going to affect results for intermediate to strong on-site repulsion. Calculations will be performed for systems of 40 sites. Looking at Fig. 4.7, for very large on-site repulsion, the holes are pushed to each half of the system, forming two peaks. The two peak maxima are approximately 15 sites apart. We will see this for

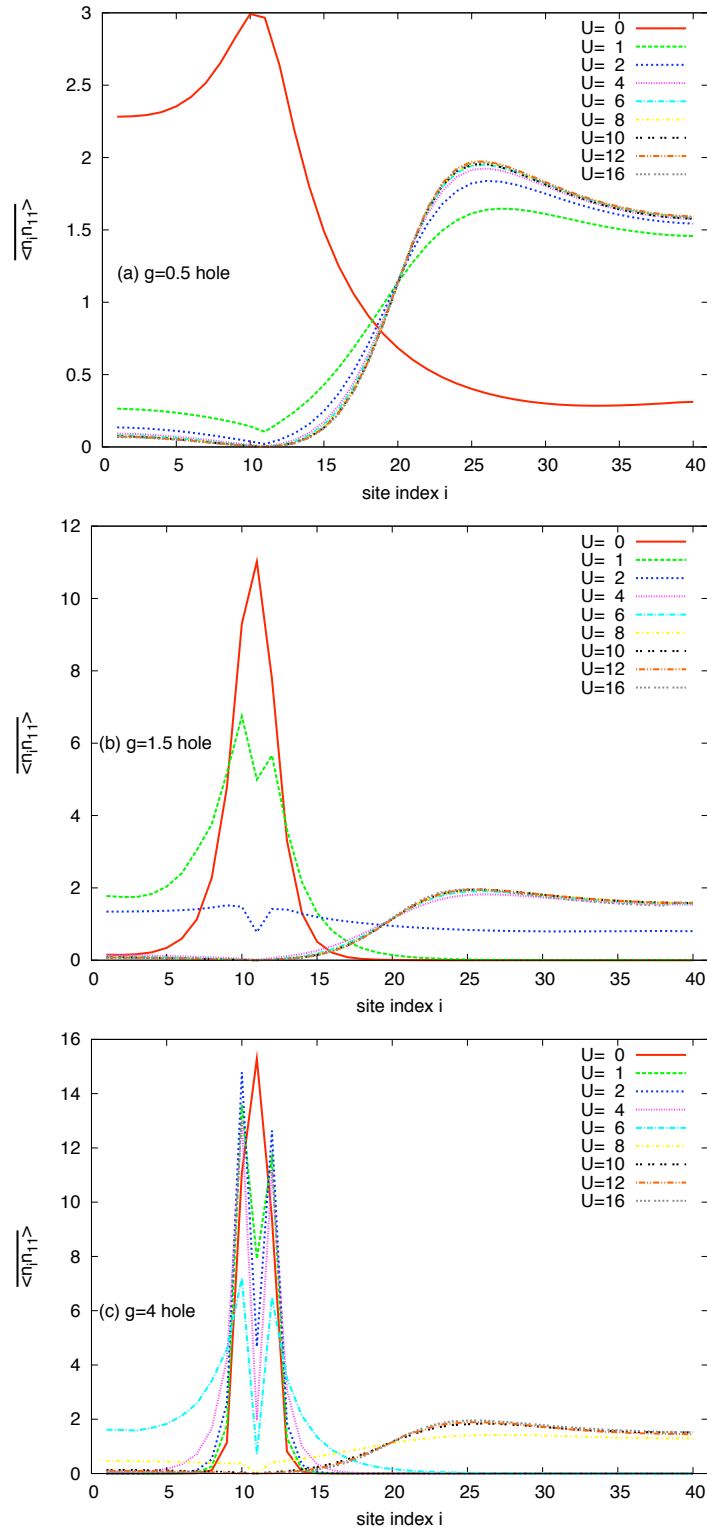


Figure 4.15: Normalized density-density correlation function (see text) for the same system as Fig. 4.11. Unity is no-correlation. Attraction is observed for a wide range of the on-site repulsion for intermediate (b) to strong coupling (c).

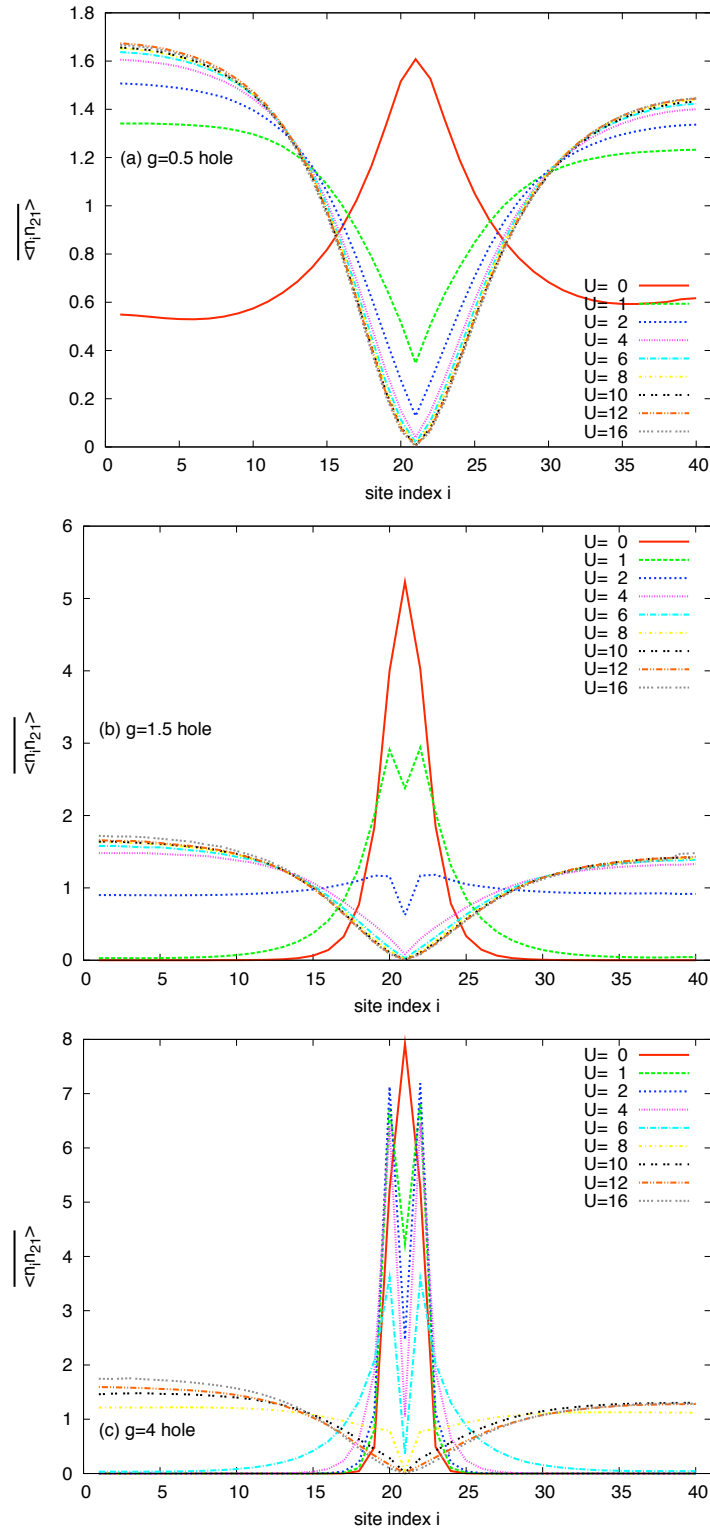


Figure 4.16: Normalized density-density correlation function (see text) for the same system as Fig. 4.12. Unity is no-correlation. Attraction is observed for a wide range of the on-site repulsion for intermediate (b) to strong coupling (c).

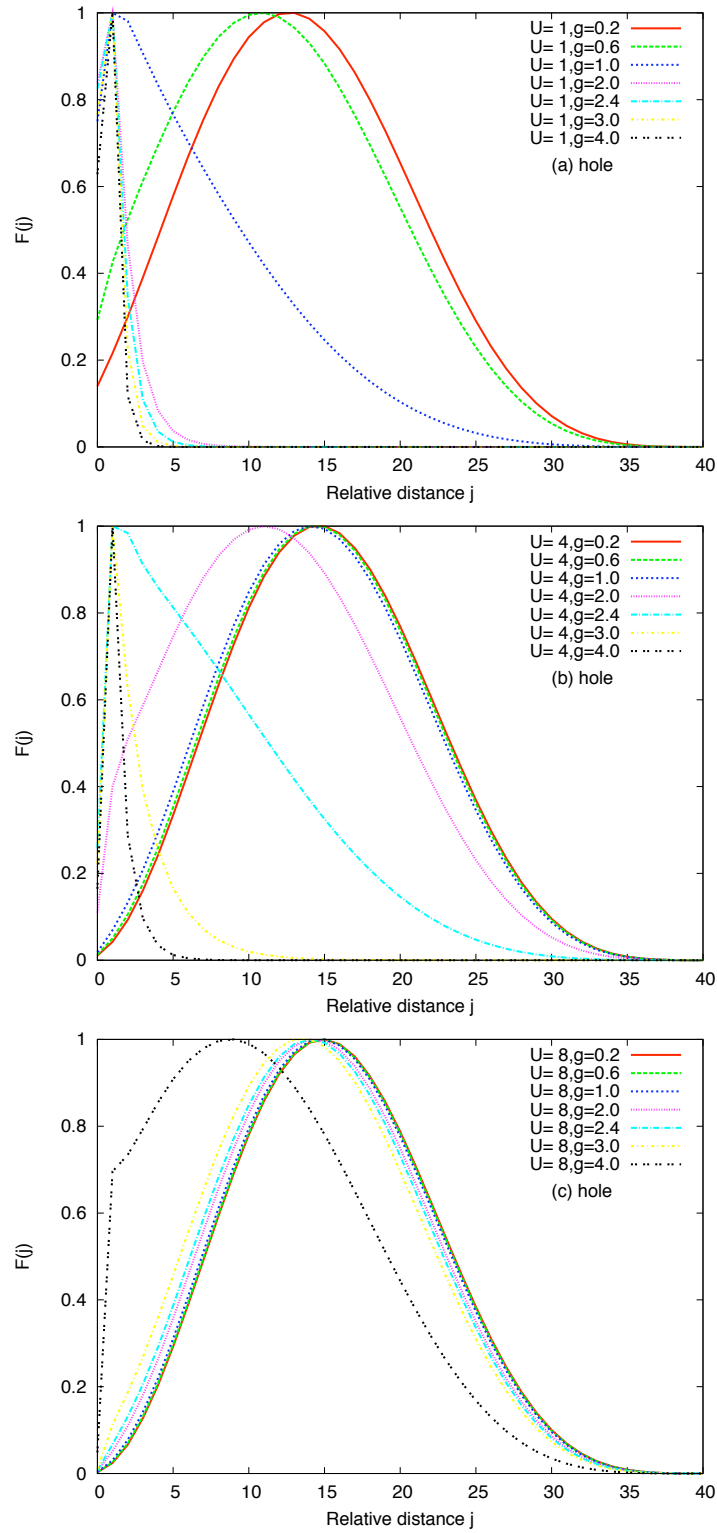


Figure 4.17: Relative location of two holes for a 40-site system interacting via the dynamic Hubbard model with small (a), intermediate (b) and strong (c) on-site repulsion. Nearest neighbor attraction persists even for $U = 8$ with $g = 4$.

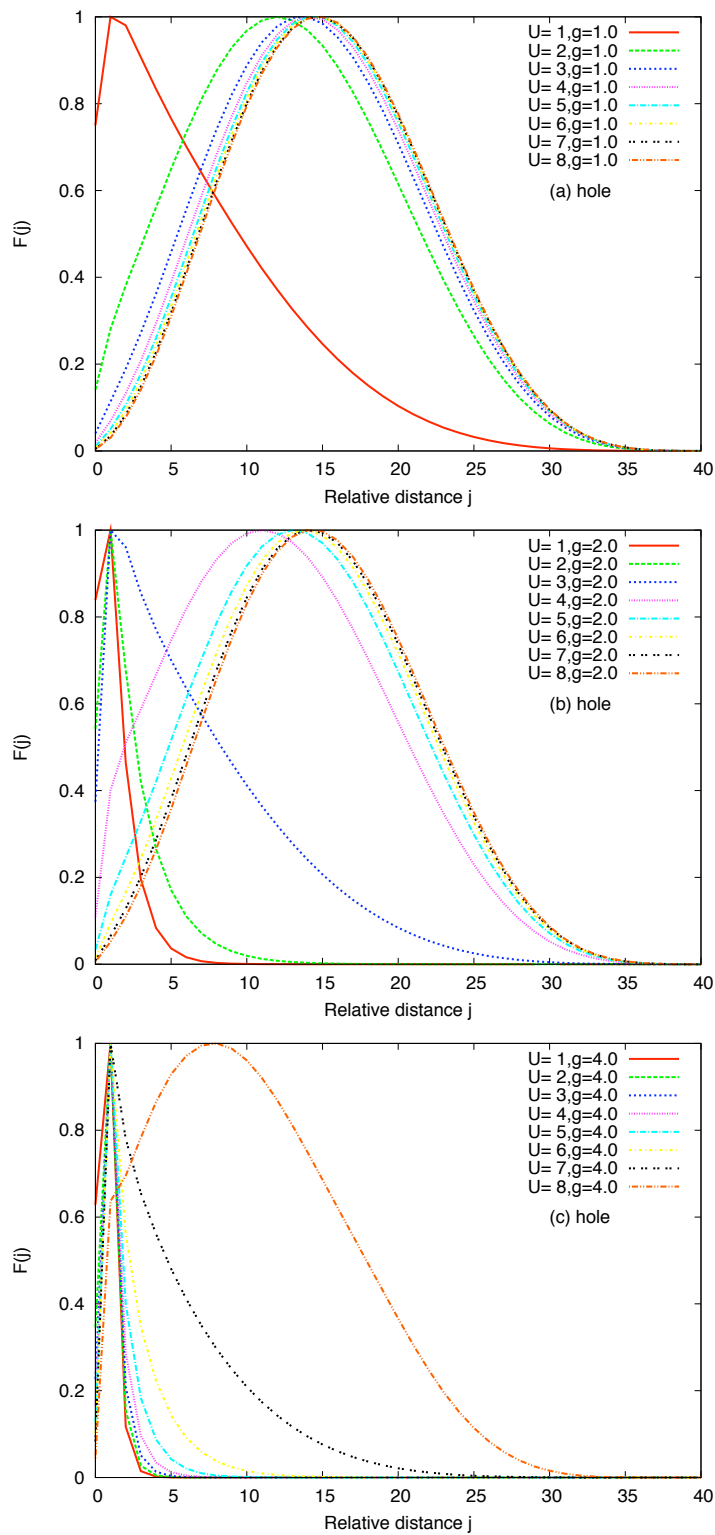


Figure 4.18: Change from attraction to repulsion by increasing on-site repulsion of two holes for a 40-site system interacting via the dynamic Hubbard model with small (a), intermediate (b) and strong (c) coupling. Attraction dies off at different points for different coupling constants

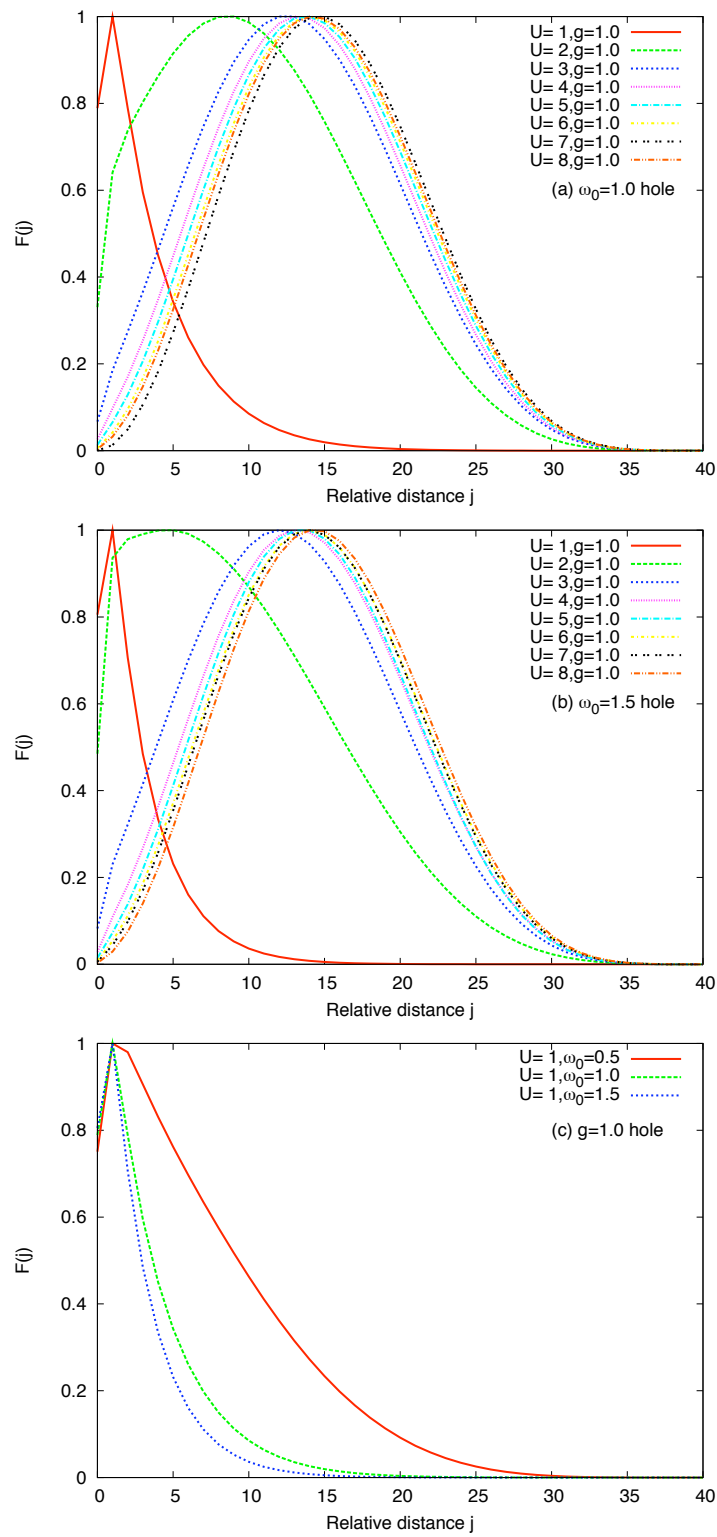


Figure 4.19: Effect of spin frequency, ω_0 . For $\omega_0 = 0.5$, refer to Fig. 4.18a.

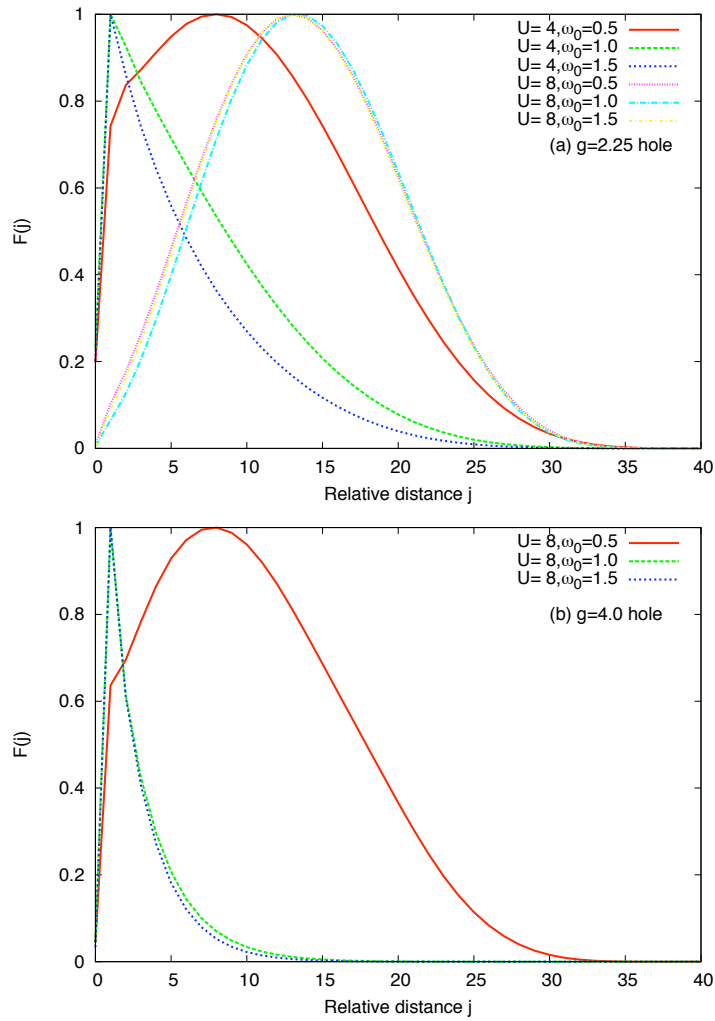


Figure 4.20: Coupling to spins as affected from ω_0 . Counter intuitive behavior is observed for the effect of frequency.

very high on-site repulsion. This is the limit that gives maximum separation. We will take this as the absolute repulsion of the holes. When there is attraction, holes will want to stay closer to each other. Depending on how close they are, the effective attraction will be different. As seen in Figs. 4.11, 4.12, 4.15, and 4.16, the attraction can be on-site or effective nearest neighbor. There is a big difference in magnitude of the correlations depending on how the coupling of the holes enhances the correlation function. Therefore the results by themselves are not very informative. To scale them, we set the maximum of each correlation function to unity and scaled the rest respectively. This way, we can tell, with respect to the maximum, how each distance is preferred.

We plot how the introduction of the hole-pseudo-spin interaction affects the relative location for three different regimes of the on-site repulsion in Fig. 4.17. For low on-site repulsion, attraction is formed for weak coupling. Since the repulsion is not strong enough, we cannot tell if this is on-site or nearest-neighbor. For intermediate on-site repulsion, on the other hand, the magnitude for the same site nearly vanishes, and introduction of the coupling builds a well-defined nearest neighbor peak, that appears for only strong coupling at high on-site repulsion.

For weak coupling, attraction occurs for only very small on-site repulsion, as seen in Fig. 4.18. For stronger couplings, attraction persists for larger on-site repulsion. For $g = 4$, there is a very well defined nearest neighbor peak or existence of attraction for all on-site repulsions shown in the figure.

We have looked at how changing the coupling constant affects on-site and nearest neighbor attraction. Another factor appears to be the frequency of pseudo-spins. The frequency enters the model both through the coupling and determining the energy of the spins. Even though the coupling is affected by $g\omega_0$ that has both the coupling constant and the energy of the pseudo-spins, each of them has different type of contribution to the interaction.

We repeat the calculation for $g = 1$ in Fig. 4.19 for larger frequency, ω_0 . For low on-site repulsion, $U = 1$, we see that the attraction is enhanced in comparison to lower ω_0 , as the tail for larger relative distances drops sharper. For $U = 2$, at $\omega_0 = 0.5$, there is a slight tendency towards attraction. This tendency is enhanced and for $\omega_0 = 1.5$, a well established attraction (though not completely nearest neighbor) is formed. This shows that if there is a sign that there might be attractive interaction between the holes, increase of the frequency enhances it. On the other hand, for $U > 2$, we do not see any qualitative change to the behavior of the holes. We plot a comparison of two different on-site repulsion in Fig. 4.20.

For $g = 2.25$, we examine the case with $U = 4$ and 8 and $\omega_0 = 0.5, 1, \text{ and } 1.5$. As shown in Fig. 4.20, we have no signature for attractive behavior for $U = 8$ $g = 2.25$

for any plotted frequency value. For $U = 8$, we also plot larger hole-spin coupling, $g = 4$, for comparison of change of coupling versus change of frequency. When the coupling is increased, we see attractive behavior even for $\omega_0 = 0.5$. Increasing the frequency, ω_0 causes the difference between two spin energy levels to grow. Additional energy changes the way spins interact with the holes causing the coupling to become more costly. It is this additional cost that prevents the system from having the same effect for the change of coupling and change of the energy, ω_0 , of the spins.

Chapter 5

Dynamical Response Functions of the DHM

In this chapter, we analyze the dynamic Hubbard model through dynamical response functions. The dynamical behavior of the dynamic Hubbard model is expected to be different than any electron-hole symmetric version of a fermion-pseudo-spin Hamiltonian. The details will be analyzed in this chapter.

In particular, we will look at the optical conductivity and the spectral function to observe the differences between the dynamic Hubbard model for electrons and the dynamic Hubbard model for holes. To identify any feature that is specific to electron-hole asymmetry we repeat the analysis for an electron-hole symmetric model as well. In order to satisfy the same conditions as the electron-hole asymmetric model, the on-site repulsion will be changed to attraction as this model is expected to exhibit dressing of Landau quasiparticles.

In the previous chapter, we established that the introduction of the pseudo-spin modifies the behavior of electrons (or holes) through the coupling, g . We have established that the modification is towards binding for holes but towards repulsion for electrons.

Dynamical response functions will enable us to see whether the effective attraction between the fermions (only for holes in this case) represents the dressing of Landau quasiparticles which suggests that attraction between fermions will lead to a higher effective mass of the fermions and a decrease of quasiparticle residue as the attraction is formed.

We will use Chebyshev polynomials to analyze these response functions. The main restriction in this case, again, is that the number of states grows exponentially as the system size is increased. The largest system we analyzed is 16 sites for one dimensional systems. The majority of the results are for a system size of 10 sites, and

we show a combination of results from many calculations, and the matrix size of the Hamiltonian grows faster than exponential.

Dynamic response functions, the spectral function and the optical conductivity, have been calculated for the dynamic Hubbard model through exact diagonalization for four sites, for pseudo-spin model [43] and modulated hopping model [45]. The analysis done for the pseudo-spin model follows closely what will be presented in this chapter. However, due to the small system size, it is not shown there.

5.1 Spectral Function

We first look at the spectral function for the models mentioned. The spectral function has two components;

$$A^-(k, \omega) = \frac{1}{\pi} \lim_{\epsilon \rightarrow 0} \text{Im}(\langle \Psi_0^n | c_k^\dagger \frac{1}{\omega - i\epsilon - (H^{n-1} - E_0^{n-1})} c_k | \Psi_0^n \rangle), \quad (5.1)$$

$$A^+(k, \omega) = \frac{1}{\pi} \lim_{\epsilon \rightarrow 0} \text{Im}(\langle \Psi_0^n | c_k \frac{1}{\omega - i\epsilon - (H^{n+1} - E_0^{n+1})} c_k^\dagger | \Psi_0^n \rangle), \quad (5.2)$$

where the Hamiltonian and the ground state are calculated for their respective subspace of the total Hilbert space. We are interested in the competition between the on-site repulsion and the electron-pseudo-spin interaction. We will only calculate the fermion destruction component of the spectral function. We will restrict ourselves to the $k = 0$ case, so the momentum index of the spectral function will be dropped, $A^-(k, \omega) \rightarrow A^-(\omega)$.

We will focus on how the quasiparticle weight is modified with the introduction of interaction. Within standard theory, Landau quasiparticles have maximum weight for non-interacting fermions, and the weight is reduced with the onset of the coupling.

The value of the spectral function at zero frequency (after the limit is taken) is related to the total quasiparticle weight. In the rigorous formulation, there is a delta function at $\omega = 0$, where strength represents the total quasiparticle weight. In numerical analysis, we calculate the response function at certain frequencies. In addition, we will approximate the response function by a finite summation, which will generate oscillatory results (Gibbs oscillations) for the delta function. To avoid these problems, rewrite the delta function as a limit of a Lorentzian function.

$$z\delta(\omega) = z \lim_{\epsilon \rightarrow 0} \frac{1}{\pi} \frac{\epsilon}{\omega^2 + \epsilon^2}. \quad (5.3)$$

The total weight of both sides is z . Therefore, for a given broadening ϵ , the value of

the function at $\omega = 0$ is;

$$A^-(0) = \frac{z}{\epsilon\pi}, \quad (5.4)$$

and therefore the total weight z can be deduced from the value of the spectral function at $\omega = 0$ with the broadening factor of $\epsilon = 0.1$ that was used for the analysis of the spectral function.

We start with the dynamic Hubbard model for electrons. In Fig. 5.1, we plot the $A^-(\omega)$ component of the spectral function, for $U = -4, 0, 4$ and 8 for $g = 1$ and 3 with $\omega_0 = 0.5$. The only feature we observe is the quasiparticle peak at zero frequency. There is an additional peak forming as we increase U . However, the latter is very small in comparison to the quasiparticle peak. The weight is changed as the parameters are changed. In Fig. 5.2, we plot the peak value for each value of U for a range of electron-pseudo-spin couplings. We note two features. As U is increased, we observe an increase followed by a decrease. The decrease is not as pronounced as the increase. We have already established that this case results in repulsive behavior. The direction of change, (the increase in quasiparticle peak) is indicative that as the on-site repulsion is increased (starting from very negative values), the effect of electron-pseudo-spin interaction between the electrons is reduced, and gradually replaced with the on-site repulsion. For completeness, in Fig. 5.2, we also plot one case with larger ω_0 . The behavior closely follows that of the corresponding larger g . The existence of the peak in Fig. 5.2, and the movement of it as g and ω_0 is changed, will be analyzed together with the hole case.

The behavior of the holes is very different. In Fig. 5.3, we plot the spectral function with the same parameters as Fig. 5.1, but for holes. For $g = 1$, we note that the behavior for the quasiparticle peak appears to be very similar to the electron case. The very small incoherent part for electrons is more pronounced in this case than for the electrons. As g and ω_0 are small, the incoherent part is very close to the ground state quasiparticle peak, and is small in magnitude in comparison to the quasiparticle residue. This is in accordance with expectations from interacting systems that as the interaction is increased, the quasiparticle peak is expected to diminish and the incoherent part to grow. This does not require that the interaction is attractive. For larger value of hole-quasi-spin coupling, $g = 3$, unlike electrons, there is a much smaller change to the quasiparticle residue. On the other hand the incoherent part is much stronger, as expected, and appears at higher frequencies. The relative peak maxima for the incoherent part change considerably with changing on-site repulsion. Focusing on the quasiparticle peak, we see a similar behavior to the electrons with small g . On the other hand, large values of g exhibit very little change. The on-site repulsion is expected to be a negating factor in the interaction,

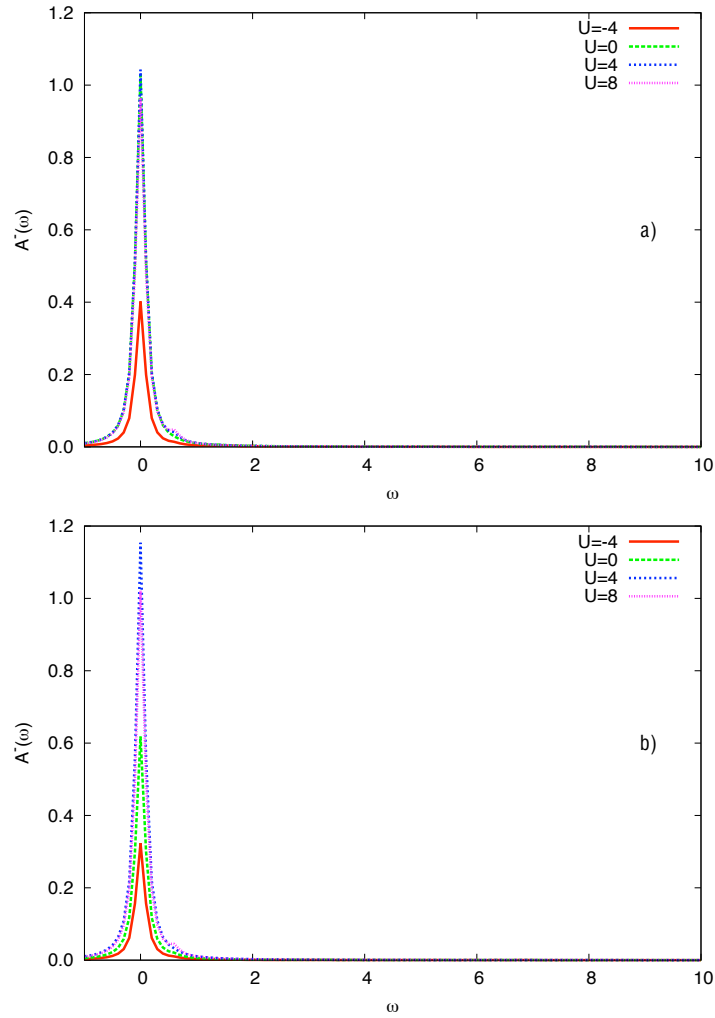


Figure 5.1: The $A^-(\omega)$ component of the spectral function for electrons interacting via the dynamic Hubbard model for a) $g = 1$ and b) $g = 3$ for a 12-site system with Hilbert space of 589,824. In both cases, the behavior is similar.

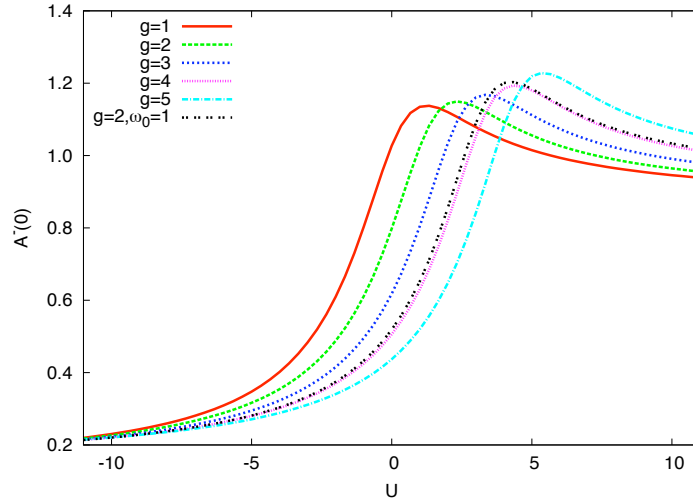


Figure 5.2: The value of the $A^-(\omega)$ component of the spectral function at $\omega = 0$ for electrons interacting via the dynamic Hubbard model for a 10-site system with Hilbert space of 102,400. The increase in energy scale of pseudo-spin has the same effect as changing the coupling. $\omega_0 = 0.5$ except as indicated.

and increasing the repulsion works against the existing hole-pseudo-spin coupling. We plot the peak value of the zero frequency weight in Fig. 5.4. For completeness, a larger value of ω_0 is also shown in Fig. 5.4. Starting from $U = 0$ in the case of $g = 1$ for both electrons and holes, increasing the on-site repulsion negates the effect of the coupling first, pushing the quasiparticle peak higher. Then, the on-site repulsion part takes over and the quasiparticle peak diminishes as the interaction with the on-site repulsion becomes dominant. For larger values of g , as seen in Fig. 5.4, we see a similar behavior, decrease of quasiparticle residue, right from the onset of the on-site repulsion, $U = 0$. However, this decrease is not of the same type as the low g case. We have already shown in the previous chapter that, for large values of g , the introduction of the on-site repulsion enhances the correlation between the holes. The reduction in quasiparticle peak is an enhancement to the already present coupling, enhancing the effect of the hole-pseudo-spin interaction. The reduction we see at low positive U for large g is the result of that effect. The two different behaviors at low positive U , going up or down as U is increased, is a continuous change from the on-site repulsion negating the hole-pseudo-spin interaction to one that is enhancing the interaction. As we increase U further, we note a peak still exists but at higher frequencies. This frequency that the peak occurs corresponds to the value of U_{eff} plotted in Fig. 5.5. In this figure, we plot the generic definition of attraction;

$$U_{eff} = (E(2) - E(1)) - (E(1) - E(0)) = E(2) + E(0) - 2E(1), \quad (5.5)$$

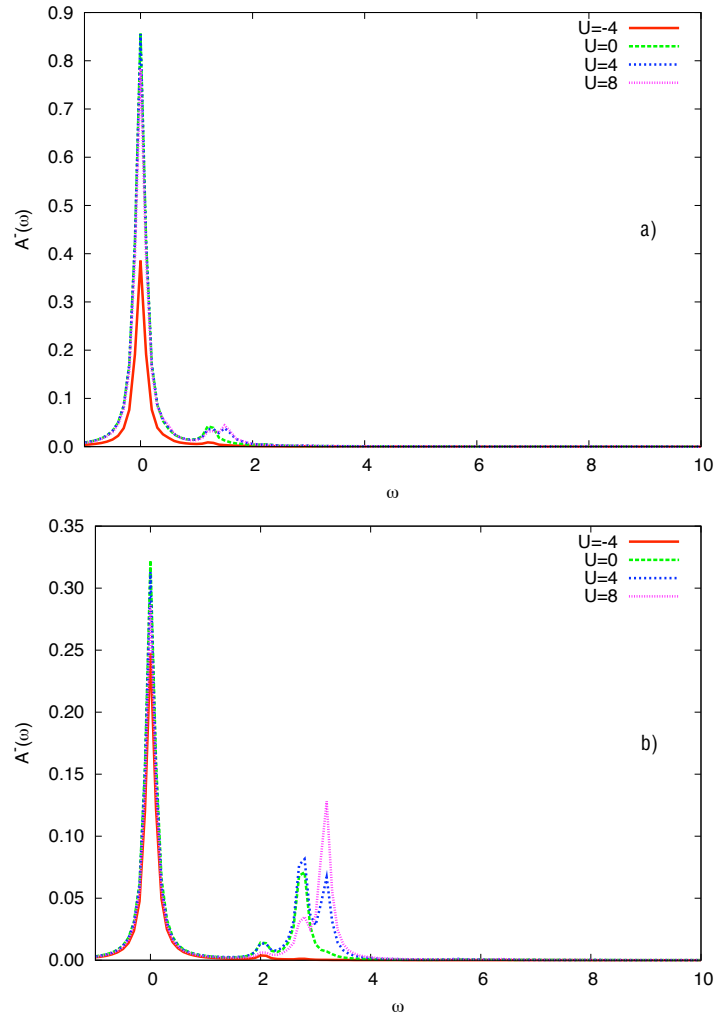


Figure 5.3: The $A^-(\omega)$ component of the spectral function for two holes interacting via the dynamic Hubbard model for a) $g = 1$ and b) $g = 3$ for a 12-site system with Hilbert space of 589,824. The incoherent part is considerably enhanced with higher coupling.

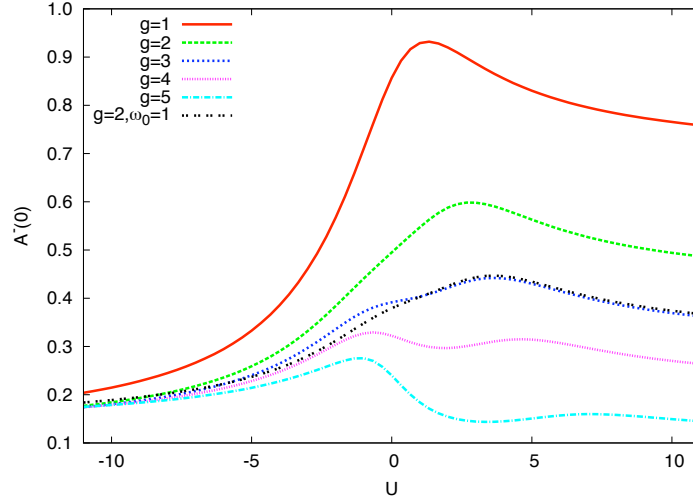


Figure 5.4: The value of the $A^-(\omega)$ component of the spectral function at $\omega = 0$ for holes interacting via the dynamic Hubbard model for a 10-site system with Hilbert space of 102,400. As the coupling is increased, the peak at positive U moves to higher values and peak at negative U is revealed. The increase in energy scale of pseudo-spin has the same effect as changing the coupling for negative U , but only shows relatively lower enhancement to coupling.

where $E(n)$ is the ground state energy of the Hamiltonian with n particles. The ground state energy for one and two holes are calculated using numerical subroutines, whereas, the zero hole case is given by product of the single site result with the number of sites [43];

$$E(0) = -N_s \omega_0 \sqrt{1 + g^2}. \quad (5.6)$$

When U_{eff} is negative, adding the second hole is energetically more favorable indicating that there is an attraction between the holes. Figs. 5.5 and 5.6 show that attraction is present for a range of the on-site repulsion. The value of U at which U_{eff} becomes repulsive follows closely the peak that on-site repulsion becomes the dominant interaction as seen in Fig. 5.4 for the corresponding g . This indicates that after this value of the on-site repulsion, the reduction of the quasiparticle peak is due to the dominant interaction becoming the on-site repulsion.

To compare these results with what is expected from the electron-hole symmetric model, we employ an electron-hole symmetric model, named the static Hubbard model [43]

$$H = -t \sum_{i\sigma} (c_{i\sigma}^\dagger c_{i+1\sigma} + c_{i+1\sigma}^\dagger c_{i\sigma})$$

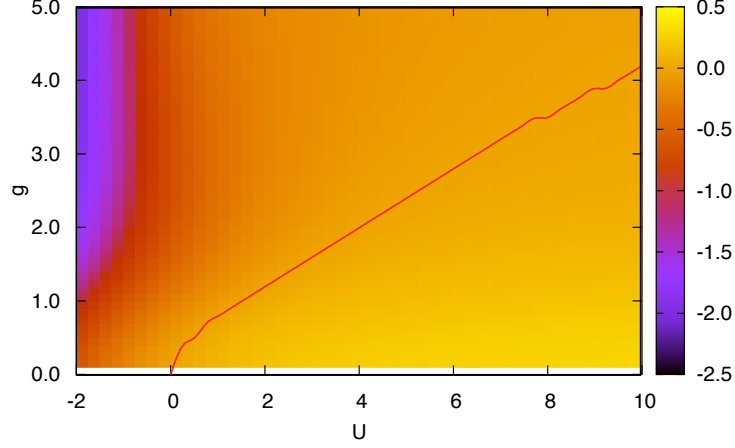


Figure 5.5: The value of effective interaction U_{eff} for holes interacting via the dynamic Hubbard model for a 10-site system with Hilbert space of 102,400. The line shows where U_{eff} changes sign.

$$+ \sum_{\mathbf{i}} \left[\omega_0 \sigma_{\mathbf{i}}^x + g \omega_0 (n_{\mathbf{i}\uparrow} + n_{\mathbf{i}\downarrow} - 1) \sigma_{\mathbf{i}}^z + U n_{\mathbf{i}\uparrow} n_{\mathbf{i}\downarrow} \right]. \quad (5.7)$$

As this model is electron-hole symmetric, we again show the results only for holes (they hold for electrons as well). However, it is not clear at this point whether we are referring to the same interaction strength, comparing the same quantities or not. Since these two Hamiltonians, Eqs. 4.2 and 5.7, will give different attraction for the same set of parameters, see Fig. 5.5 vs. Fig. 5.7 or Fig. 5.6 vs. Fig. 5.8, we need to have the same attraction for the two system. In Table 5.1, we show the value of U_{eff} for the same parameters with the dynamic (for holes) and the static Hubbard model. Since there is a large difference in the value of U_{eff} , the two models for the same parameters do not correspond to the same interaction of the fermions. We would like to have the same value of U_{eff} for both models to compare attraction mechanisms. To eliminate this discrepancy, we also tabulate the values of the on-site repulsion to give the same U_{eff} in table 5.2. Any numeric comparison for frequency dependence will be done for these values of U so that U_{eff} and so the interaction strength is identical. As seen in Fig. 5.10, as one changes the electron-pseudo-spin coupling, the quasiparticle peak changes similar to that of electrons of the dynamic Hubbard model, Fig. 5.1. Looking at the spectral function as a function of frequency, Fig. 5.9, reveals similar behavior. This indicates that the static model does not show the transition from weak coupling to strong coupling that the holes exhibit. On the other hand,

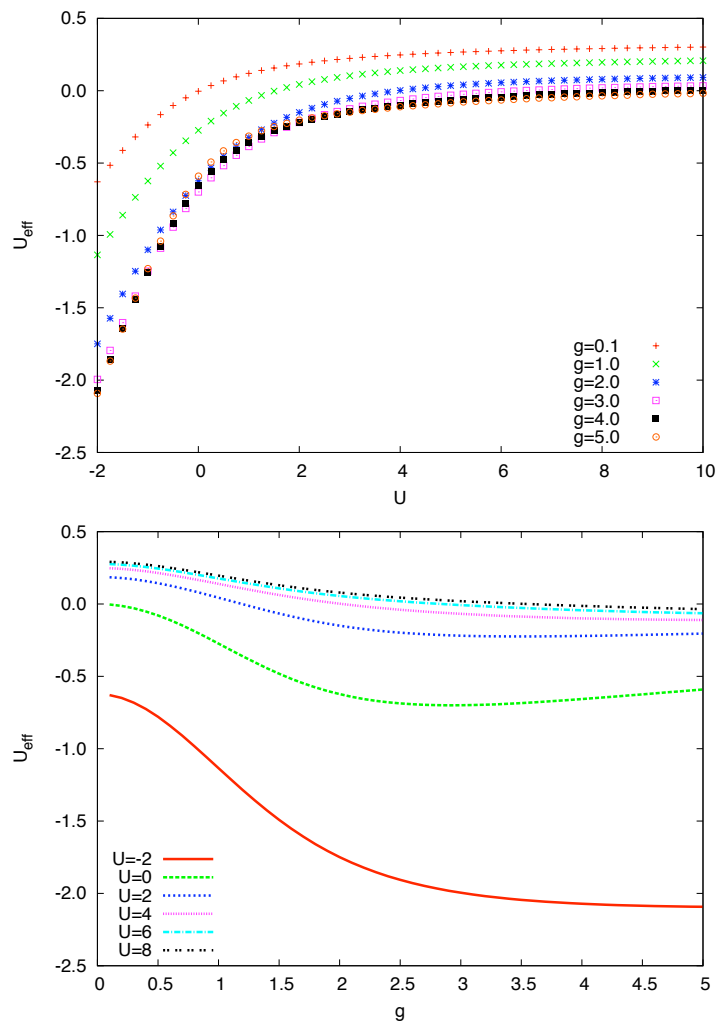


Figure 5.6: The value of effective interaction U_{eff} for holes interacting via the dynamic Hubbard model as a function of the parameters U and g for a 10-site system with Hilbert space of 102,400.

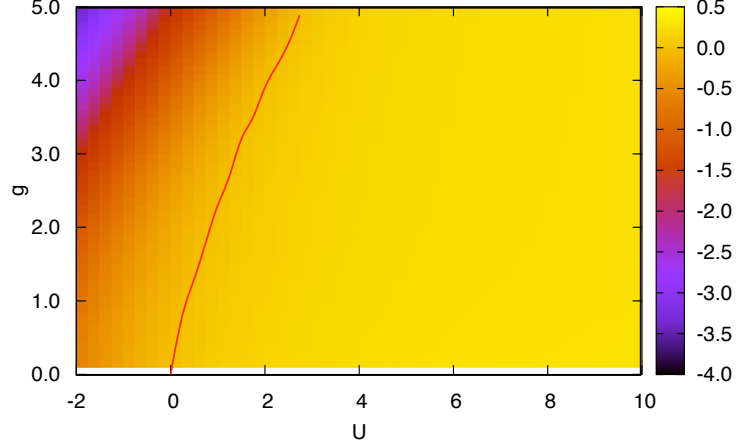


Figure 5.7: The value of effective interaction U_{eff} for fermions interacting via the static Hubbard model for a 10-site system with Hilbert space of 102,400. The line shows where U_{eff} changes sign.

U	U_{eff} (Eq. 4.3)	U_{eff} (Eq. 5.7)
-4	-3.534	-3.538
0	-0.7107	-0.4806
4	-0.0463	0.2088
8	0.0521	0.2678

Table 5.1: The value of U_{eff} of the interacting holes, for the corresponding value of U for each model with $g = 3$ and $\omega_0 = 0.5$.

the behavior of the static Hubbard model is a very similar, though not quantitatively exact match, to that of electrons within the dynamic Hubbard model.

5.2 Optical Conductivity

We repeat the same analysis for the optical conductivity of the two models. We start with the dynamic Hubbard model. The optical conductivity we will calculate has the form:

$$\sigma(\omega) = \sum_{k \neq 0} \frac{\langle \Psi_0 | J^\dagger | k \rangle \langle k | J | \Psi_0 \rangle}{E_k - E_0} \delta(\omega - (E_k - E_0)). \quad (5.8)$$

where $|k\rangle$ is the eigenstate of the Hamiltonian with energy E_k and J is the current

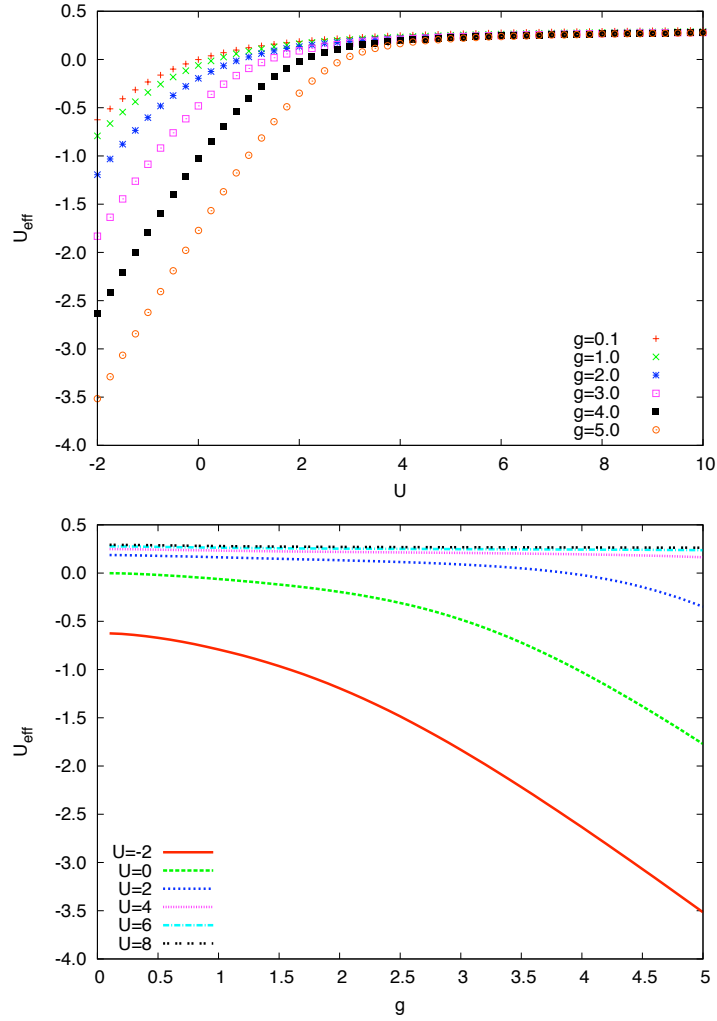


Figure 5.8: The value of effective interaction U_{eff} for fermions interacting via the static Hubbard model as a function of the parameters U and g for a 10-site system with Hilbert space of 102,400.

U_{eff} (Eq. 5.7)	U
-3.534	-3.996
-0.7107	-0.417
-0.0463	1.184
0.0521	1.713

Table 5.2: The value of U of the interacting fermions, for the corresponding value of U_{eff} for the static Hubbard model with $g = 3$ and $\omega_0 = 0.5$.

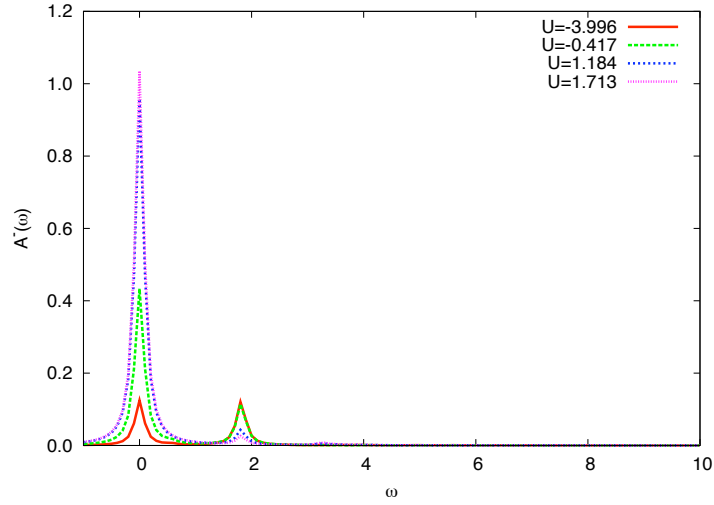


Figure 5.9: The $A^-(\omega)$ component of the spectral function for fermions interacting via static Hubbard model for $g = 3$ for a 12-site system with Hilbert space of 589,824.

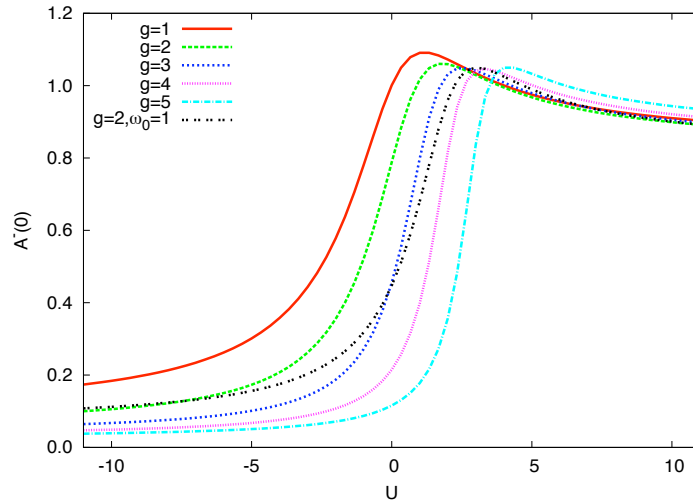


Figure 5.10: The value of the $A^-(\omega)$ component of the spectral function at $\omega = 0$ for fermions interacting via the static Hubbard model. The behavior is similar to that of electrons in the dynamic Hubbard model for a 10-site system with Hilbert space of 102,400.

operator;

$$J = -it_0 \sum_{i,\sigma} (c_{i,\sigma}^\dagger c_{i+1,\sigma} - H.c). \quad (5.9)$$

In this function, the optical conductivity, there are two parts. We are interested in the low (non-zero) frequency contribution from the intraband absorption [43] that is related to the kinetic energy. The high frequency part is interband optical weight.

We use the property of the delta function to replace the denominator, so that it can be pulled out of the summation

$$\sigma(\omega) = \frac{1}{\omega} \sum_{k \neq 0} \langle \Psi_0 | J^\dagger | k \rangle \langle k | J | \Psi_0 \rangle \delta(\omega - (E_k - E_0)). \quad (5.10)$$

This function would have a singularity at zero frequency (DC limit) if the $k = 0$ was included in the summation, though the definition omits that point. The transformation we use includes the $k = 0$ point since we use the Hamiltonian rather than the eigenstates. In addition, we will broaden the delta functions, causing the summation to have a non-zero component at zero frequency, enhancing the singularity. However, this is not what we are interested in. So, to negate the effect of the singularity, we first plot the reduced optical conductivity, $\omega\sigma(\omega)$. As long as we do not compare different frequencies, this function is very similar to the optical conductivity.

This quantity overemphasizes high frequency values, but hides the low frequency singularity. For most of the analysis, we will look at low frequencies, close to $\omega = 0$. In Fig. 5.11, we plot the reduced optical conductivity for small and large g to contrast behavioral differences. For low g , Fig 5.11a, starting from $U = 0$, as $|U|$ is increased, more weight is pushed to higher frequencies. The same effect is more pronounced for the larger value, $g = 3$, plotted in Fig. 5.11b. We see a peak forming around $\omega = 3$ for $U = 0$. This peak is pushed to higher frequencies as U is changed in either direction. We see another peak at much smaller frequencies, around $\omega = 0$. We note that the exact location of the peak is not at $\omega = 0$, so this is not an artifact of the method that includes the ground state in the calculation. Even though the overall magnitude of the peak at the low frequency is reduced in magnitude as the coupling is increased, the overall change of behavior is similar to the spectral function. We plot the highest value of this peak, changing the frequency as needed, in Fig. 5.12. We see the similarity to the spectral function here as well. For low g , as the on-site repulsion gets repulsive, the peak value increases. For large g , the highest value happens around $U = 0$, and the repulsive side behaves similarly to the attractive side. Again, the change from monotonic increase of the peak maximum to formation of a peak around $U = 0$ is gradual. We also plot the higher energy of pseudo-spin, $g = 2$ and $\omega_0 = 1.0$. Although the coupling strength is similar to $g = 4$ and $\omega_0 = 0.5$, the

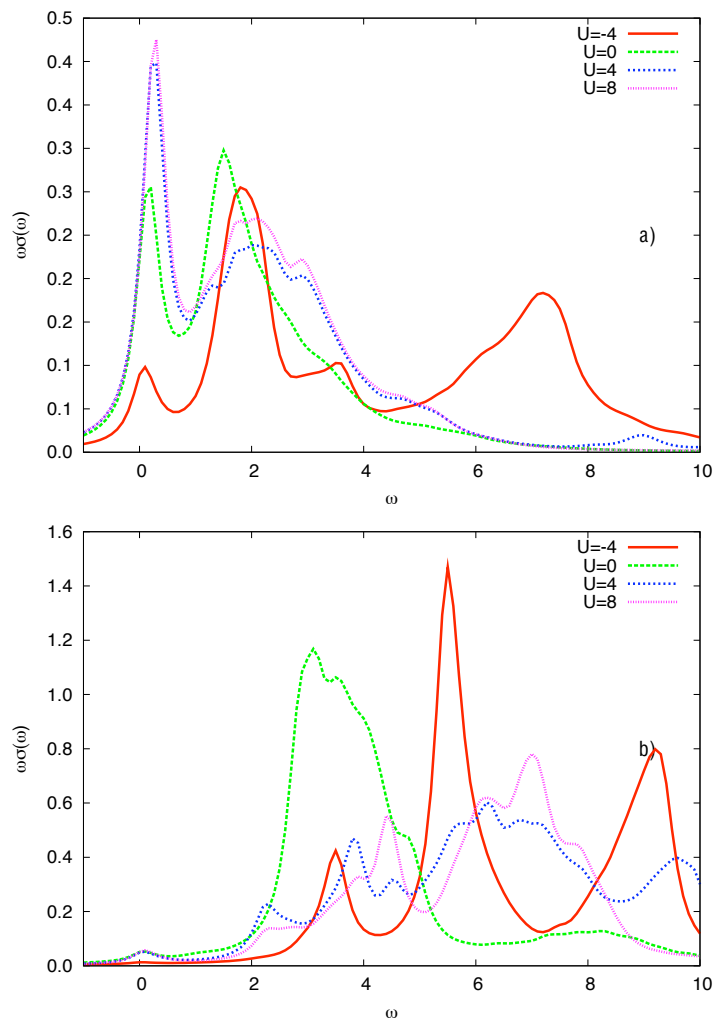


Figure 5.11: Reduced optical conductivity for holes interacting via the dynamic Hubbard model for a) $g = 1$ and b) $g = 3$ for a 12-site system with Hilbert space of 589,824. As the magnitude of the on-site repulsion is increased, the weight is pushed to higher frequencies especially at strong coupling.

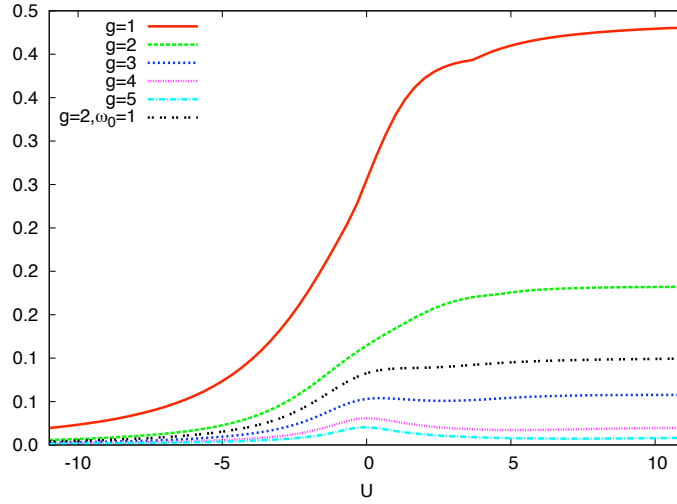


Figure 5.12: The maximum of the reduced optical conductivity around $\omega = 0$ for holes interacting via the dynamic Hubbard model for a 10-site system with Hilbert space of 102,400. As the coupling is increased, the behavior for positive U is modified considerably. For strong coupling, a peak around $U = 0$ is formed.

peak around $U = 0$ is not formed even though the energy equivalent of the coupling is increased.

In Fig. 5.13, we plot the optical conductivity as a function of frequency. The zero frequency divergence is overwhelming, so the scaling is set so that only higher frequency results are emphasized. In this case, again, introduction of the on-site repulsion pushes the weight to higher frequencies.

In Figs. 5.14 and 5.15, we repeat the same analysis for the static Hubbard model. Reduced optical conductivity as a function of frequency, Fig. 5.14, shows that the weight is pushed to the lower frequencies. The height of the peak around zero frequency is enhanced with increasing U . The height of the peak around $\omega = 0$ is plotted in Fig. 5.15. We note that the overall behavior is similar to the spectral function, Fig. 5.10. The peak height is enhanced as the on-site repulsion is increased. As seen in Fig. 5.14, not only the peak at zero frequency is enhanced, but also additional weight is pushed from higher frequencies to lower frequencies.

For completeness, we also show that the optical conductivity, Fig. 5.16, follows the same trend for static Hubbard model that with increasing U , the weight is pushed to the lower frequencies.

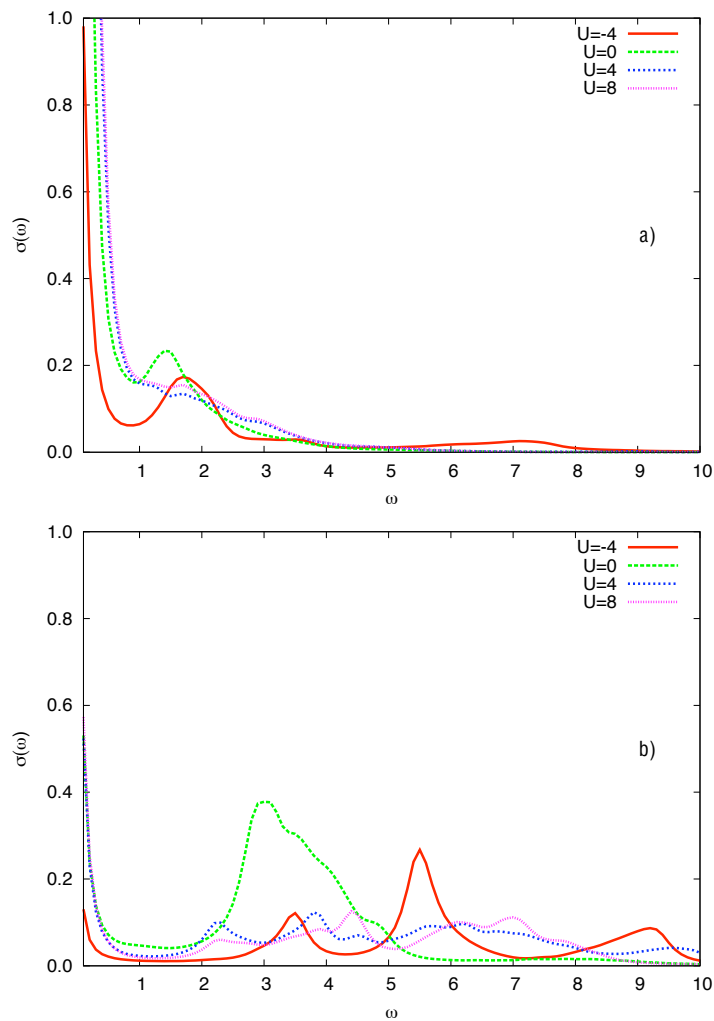


Figure 5.13: Optical conductivity for holes interacting via the dynamic Hubbard model for a) $g = 1$ and b) $g = 3$ for a 12-site system with Hilbert space of 589,824. As the magnitude of the on-site repulsion is increased, the weight is pushed to higher frequencies especially at strong coupling.

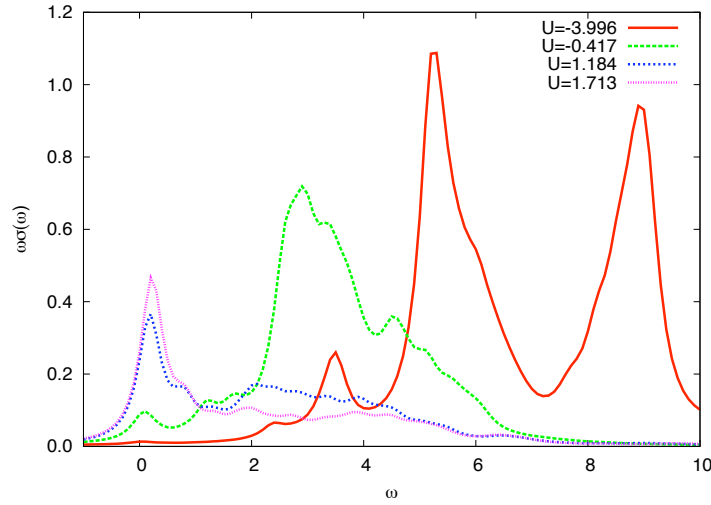


Figure 5.14: Reduced optical conductivity for fermions interacting via static Hubbard model for $g = 3$ for a 12-site system with Hilbert space of 589,824. As the on-site repulsion is increased, the weight is pushed to lower frequencies.

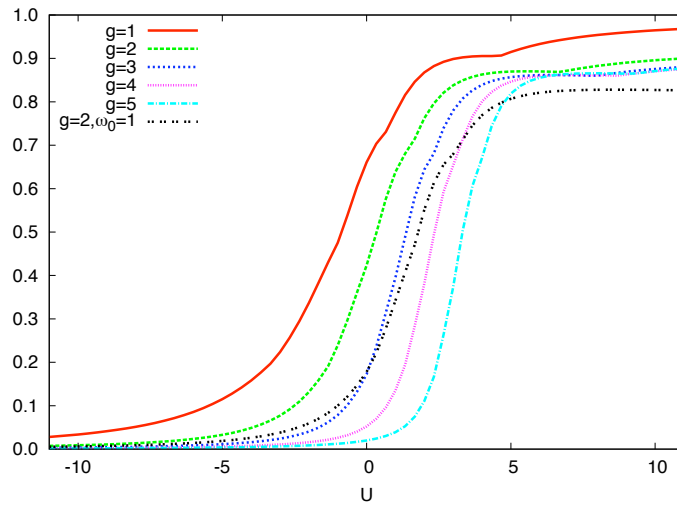


Figure 5.15: The maximum of the reduced optical conductivity around $\omega = 0$ for fermions interacting via static Hubbard model for a 10-site system with Hilbert space of 102,400. As the coupling is increased, the trend is shifted to higher on-site repulsions.

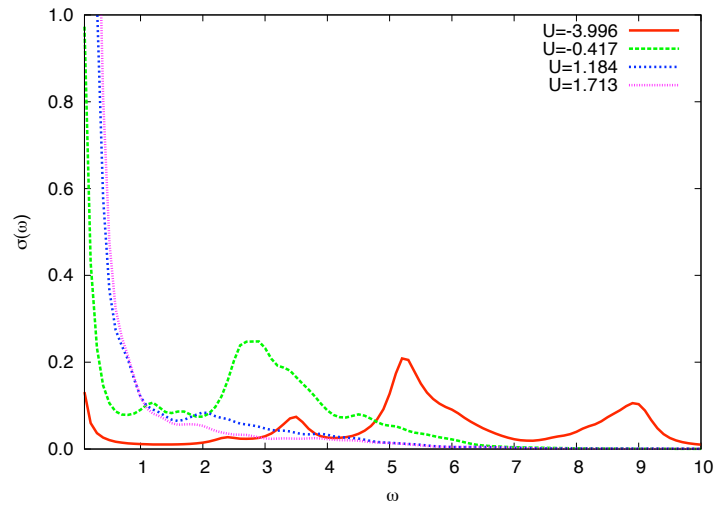


Figure 5.16: Optical conductivity for fermions interacting via static Hubbard model for $g = 3$ for a 12-site system with Hilbert space of 589,824.

Chapter 6

Conclusions on the Dynamic Hubbard Model

In the previous two chapters, through a comparative analysis, we have modeled the different effects the core electrons would have on two electrons and two holes through the dynamic Hubbard model. The dynamic Hubbard model shows repulsive behavior for electrons and, depending on the coupling constant, g , attraction between holes is possible. The coupling exhibits an effective nearest neighbor attraction even in the presence of the on-site repulsion.

Dynamic response functions, the spectral function and the optical conductivity, have shown that for electrons, interacting via the dynamic Hubbard model, the on-site repulsion negates the electron-pseudo-spin coupling gradually, and becomes the dominant interaction of the system. Density profile and density-density correlation functions show that even when the on-site repulsion is not present, we observe repulsion between two electrons.

For small hole-pseudo-spin coupling, a similar behavior to electrons is observed for dynamic response functions, though in the case of the spectral function, considerable weight appears for the incoherent, $\omega \neq 0$, part. The density profile and density density correlation function, on the other hand, show contrasting behavior. Holes are effectively attracted to each other in the presence of the coupling. When no on-site repulsion is present, attraction appears to be on-site; however, with the introduction of the on-site repulsion, effective nearest neighbor attraction is observed. As the on-site repulsion becomes larger, the nearest neighbor attraction is dominated by the on-site repulsion, and we get a similar behavior to electrons for large on-site repulsion. For large hole-pseudo-spin coupling, (strong coupling, $g > 2.5$), both dynamic response functions and density-density correlation functions show different behavior. They indicate that non-zero U would first enhance the interaction. This is

shown in the dynamic response functions with the decrease of the quasi-particle weight indicating that the interaction is enhanced. The density-density correlation function shows a considerable increase to the nearest neighbor peak with the introduction of on-site repulsion. Also, the more pronounced peak in the density profile indicates the enhancement of attraction due to the on-site repulsion.

In order to compare with the electron-hole symmetric model, the density profile and the density-density correlation function have been compared to the Hubbard model. The dynamic response functions have been compared to the fermion-pseudo-spin coupling of single occupancy, namely the static Hubbard model. This model has the additional piece of the dynamic Hubbard model for holes (coupling to single occupancy) and does not have the piece of the dynamic Hubbard model for electrons (coupling to double occupancy). Neither of these electron-hole symmetric models show behavior similar to the holes interacting via the dynamic Hubbard model while electrons interacting via the dynamic Hubbard model show similar trends to electron-hole symmetric model.

We conclude from these aspects of the models that the dynamic Hubbard model exhibit attraction that is the result of it being a electron-hole asymmetric model, while Hamiltonians with very similar structure fail to do so.

Chapter 7

Non-Equilibrium Bound State

7.1 Introduction

In this chapter, we look at a fully quantum mechanical analysis of an itinerant spin current interacting with a ferromagnetic layer. The itinerant spin current is modeled via a spin wave packet and the magnetic layer is modeled via coupled local spins. Then, the spin current is coupled to the magnetic layer via a Kondo-like interaction:

$$H = -t_0 \sum_{\langle i,j \rangle \sigma} c_{i\sigma}^\dagger c_{j\sigma} - 2 \sum_{l=1}^{N_s} J_0 \sigma_l \cdot \mathbf{S}_l - 2 \sum_{l=1}^{N_s-1} J_1 \mathbf{S}_l \cdot \mathbf{S}_{l+1}, \quad (7.1)$$

where $c_{i\sigma}^\dagger$ creates an itinerant particle with spin σ at site i , \mathbf{S}_l is a localized spin operator at site l , t_0 is a hopping amplitude between nearest neighbor sites, so that the itinerant spin can move along the length of the entire chain, and J_0 is the coupling between the electron spin and a local spin. Note that J_0 coupling takes place only when an electron is on the site of the local spin. The parameter J_1 is a coupling between two neighboring localized spins. For a ferromagnetic chain, we have $J_1 > 0$.

The wave packet consists, in general, of many spins, interacting with the local spins. Many itinerant spins are needed to change the orientation of the local spins to have the same direction with the local spins. Using density matrices to account for entanglement, we have shown [26] that the wave packet changes the direction, gradually, of local spins.

We have analyzed the common practice of using a complex potential to eliminate entanglement of the wave packet to the local spins. Our analysis of absorption of the wave packet by the complex potential [27] showed features of “action at a distance” due to absorption of the entangled wave packet by the complex potential.

This chapter focuses on the nature of the entanglement between the incoming wave packet and local spins. As done previously, we will restrict ourselves to one dimension.

However, from an analytical point of view, the arguments can be expanded to higher dimensions. We start with the method we use in this chapter in Sec. 7.2. Then we show the numerical results of a spin-up wave packet interacting with two local spins (both initially pointing down) focusing on the wave packet and the local spin, separately in Sec. 7.3, and together in Sec 7.4. In Sec. 7.5, we repeat the analysis in the entangled basis that combines the states of the wave packet with the states of the local spins. We conclude in Sec. 7.7.

7.2 Method

For a time-dependent interaction of a wave packet with local spins, the initial state is represented by a function,

$$\varphi(x) = \frac{1}{\sqrt{2\pi a^2}} e^{ik(x-x_0)} e^{-\frac{(x-x_0)^2}{2a^2}}, \quad (7.2)$$

where the right hand side defines a Gaussian distribution centered around x_0 with a width of a moving with a wave vector k . There are several ways we can calculate the properties of the constituents before, during and after the interactions. In this chapter, we will use Hamiltonians with a large number of basis states. To avoid having to fully diagonalize the large Hamiltonian matrices, which is required by the standard way of time evolution, we will use a series expansion of the time evolution operator;

$$e^{-i\hat{H}t} = \sum_n a_n \hat{Y}_n, \quad (7.3)$$

where a_n are the coefficients of a complete orthogonal series of Y_n . Whatever orthogonal set is used, this expansion is helpful because it is easier to deal with a polynomial.

The choice for orthonormal basis that we use is Chebyshev polynomials, $T_n(X) = \cos(n \arccos(X))$ with $T_0(X) = 1, T_1(X) = X$ and $T_n(X) = 2XT_{n-1}(X) - T_{n-2}(X)$ [53]. For these polynomials, the argument needs to be less than one, so we need to renormalize the Hamiltonian.

$$e^{i\frac{\hat{H}}{\delta}\delta t} = \sum_{n=0}^{\infty} a_n(\delta t) T_n\left(\frac{\hat{H}}{\delta}\right) = \sum_{n=0}^{\infty} a_n(y) T_n(X), \quad (7.4)$$

where we redefined $y = \delta t$, and $X = \frac{\hat{H}}{\delta}$ for simplicity.

There are two reasons for choosing this particular basis. For this orthogonal set, the coefficients, $a_n(y)$ are

$$a_n(y) = \frac{2 - \delta_{n0}}{\pi} \int_{-1}^1 \frac{dx}{\sqrt{1-x^2}} T_n(x) \exp(ixy),$$

$$a_n(y) = (2 - \delta_{0n})i^n J_n(y) \quad (7.5)$$

with $J_n(y)$ being the Bessel function of first kind and order n [54]. Since the argument of the polynomials is a matrix, the trigonometric definition of the polynomials is not useful. For our purposes, we will only use the recursive relations. The polynomials have another recursion relation that allows us to use a more compact way to calculate the expansion of the exponential of the Hamiltonian,

$$T_{n+m}(X) = 2T_n(X)T_m(X) - T_{|n-m|}(X). \quad (7.6)$$

Using this equation we can rewrite the expansion up to a given order, N^2 as:

$$e^{i\frac{\hat{H}}{\delta}\delta t} \cong \sum_0^{N^2} a_i T_i = \sum_0^N b_i^0 T_i + T_N \left(\sum_1^N b_i^1 T_i + \dots + T_N \left(\sum_1^N b_i^k T_i + \dots + T_N \sum_1^N b_i^{N-1} T_i \right) \dots \right), \quad (7.7)$$

with

$$b_i^k = \sum_{j=0}^{N-k} (\text{mod}(j, 2) * A(j+k, k) a_{((j+k+1)*N-i) + \text{mod}(j+1, 2) * A(j+k, k) a_{((j+k)*N+i)}), \quad (7.8)$$

where:

$$A(i, j) = \begin{cases} A(i-1, j) + 2 * A(i-1, j-1) & \text{mod}(i-j, 2) = 0 \\ -A(i-1, j) & \text{mod}(i-j, 2) = 1 \\ 0 & i < j \end{cases} \quad (7.9)$$

with $A(0, 0) = 1$ [56] as explained in Appendix A. In this chapter, we have set $N = 12$.

7.3 Numerical Results

We simulate the interaction of the spin wave packet with an array of local spins by analyzing the time evolution of a spin wave packet as shown in Fig. 7.1. At $t = 0$, the centre of the Gaussian shaped wave packet is set to $x_0 = 700$ with a width of $a = 16$, moving with wave vector $k = \frac{\pi}{2}$ to the right on a 1600 site system with Hilbert space of 4800 unless noted otherwise. In general, any confined packet broadens with time evolution. When the wave vector is $\frac{\pi}{2}$, due to the nature of the dispersion relation, this broadening does not occur. To avoid the complication of broadening, we will not change this value. A smaller value of a is possible. The calculations done here can be repeated for any value of a as small as 6, while any smaller number results in an unnormalized, when integrated over all space, wave packet. We tried to put the wave

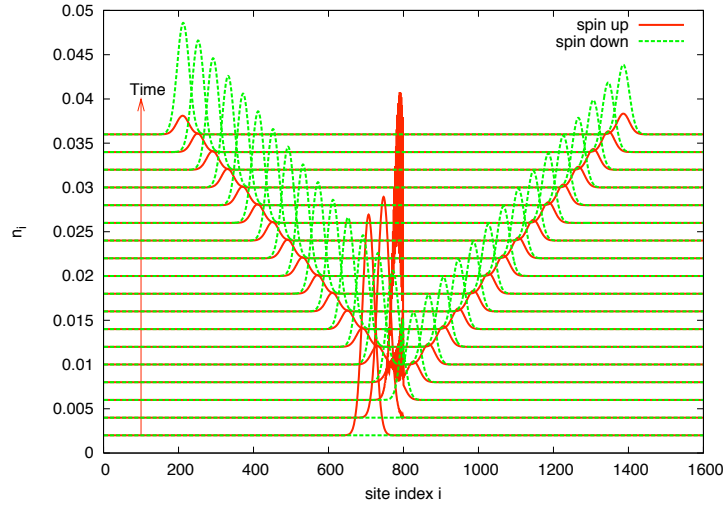


Figure 7.1: Time evolution of a wave packet, originally centered around site 700. The wave packet moves towards two local spins positioned at site indices 800 and 801, and interacts with the local spins with $J_0 = 2.0$, and $J_1 = 0.0$. After the interaction, some portion of the wave packet reflects back, and some of it transmits through with either spin.

packet as close as possible to the local spins to reduce computation time. x_0 can be any value less than 700. The wave packet with spin up starts by moving towards the local spins. After the interaction, due to spin flip interaction, some part of the spin wave packet changes spin, and a spin down component for the spin wave packet is generated. Some component of the spin wave packet transmits through, and some part reflects. Even though most of the wave packet moves away after a short time interaction, some component of the wave packet might remain in the vicinity of the local spins. To allow all parts of the wave packet to interact with the local spins, we calculate the final state of the spin wave packet long after it interacts with the local spin.

Our aim is to understand how spin chain structures interact with the incoming wave packet to simulate effects of a spin current on a magnetic layer. The internal coupling of the magnetic layer affects the layer's interaction with the spin current. For a large magnetic layer, looking at an individual local spin is too complicated and arbitrary looking that interpreting the results would be difficult. Therefore, we look at what happens to the wave packet after it interacts with the local spins, see Fig. 7.1. In Fig. 7.2, we show the value of the z-component of the wave packet spin long after its interaction with a 20 site uniform local spin system. Even though we see many structures, it is not easy to understand where each of these structures is coming from. One dominant feature is a wiggle-like structure as J_1 is changed for a constant and

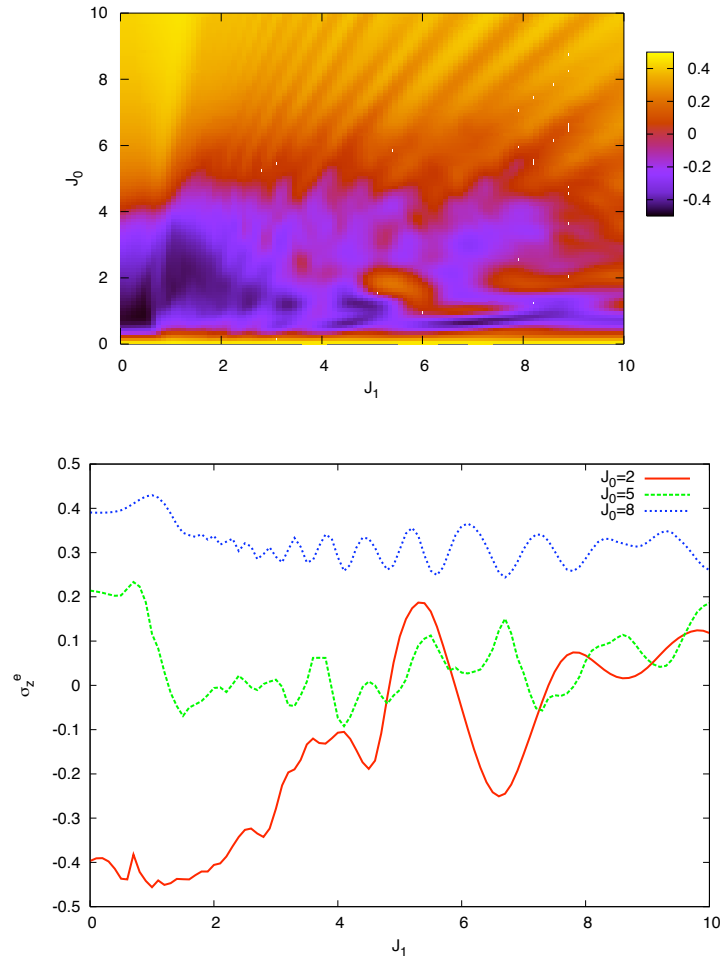


Figure 7.2: Wave packet spin long after the wave packet interacts with the local spins. Top panel: As a function of both wave packet-spin, J_0 , and spin-spin interaction, J_1 , for 20 local spins. Bottom panel: Slices through J_1 for several constant values of J_0 . Many features are present, very difficult to interpret. For computational accuracy, 3000 site lattice is used with Hilbert space of 630,000.

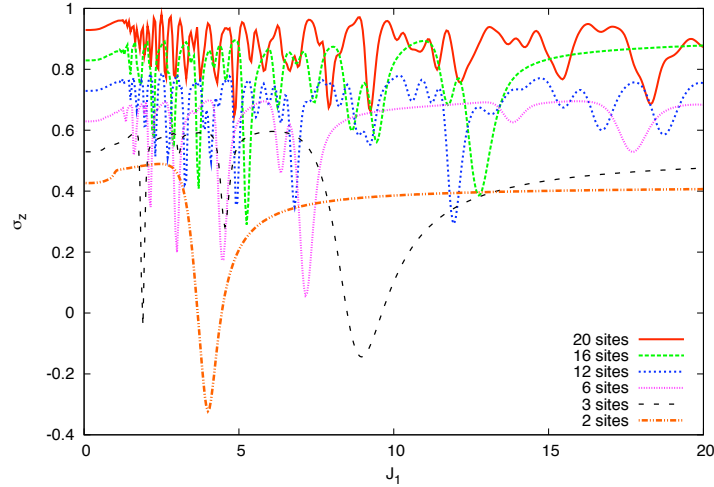


Figure 7.3: Wave packet spin long after the wave packet interacts with the local spins. Slices through J_1 for $J_0 = 10$. Many features are present, and very difficult to interpret. With a smaller number of sites the wiggles are reduced in numbers. For three sites, there are three visible ones. Note that the y-axis is shifted for better visualization. Lowest J_1 point is the same for all curves.

high J_0 . To identify the structures, we reduced the number of local spins from 20 to 2 and plotted the z-component of the wave packet spin as a function of J_1 for $J_0 = 10$ in Fig. 7.3. We note that the wiggly-like structures move and reduce in number with decreasing number of local spins. For the smallest system plotted, $N_s = 2$, the wiggly is replaced with a single ridge separating two regions of interaction. For any larger number of local spins, additional ridges establish the wiggly-like structure. This indicates that the existence of these ridges depend on having interacting local spins. To be able to focus on the origin and the effects of the ridges, we will perform the analysis on a system of size $N_s = 2$. The most general result for a 2 local spin system is shown in Fig. 7.4. We show the z-component of the wave packet spin and slices of constant J_0 . For the rest of the chapter, we will focus on this result and identify different regions and features and try to extend these features to longer local spin chains and spin chains with higher S .

We identify the following three regions. One region is the low J_1 range where we have a small change to independent local spins with the introduction of J_1 . The second region is very high J_1 , where the behavior as a function of J_0 is similar to low J_1 . The third region is the region of the ridge where the z-component of spin of the wave packet is modified considerably with respect to neighboring parts, especially for large J_0 .

We begin with the first region where J_1 is low. A good reference point in this

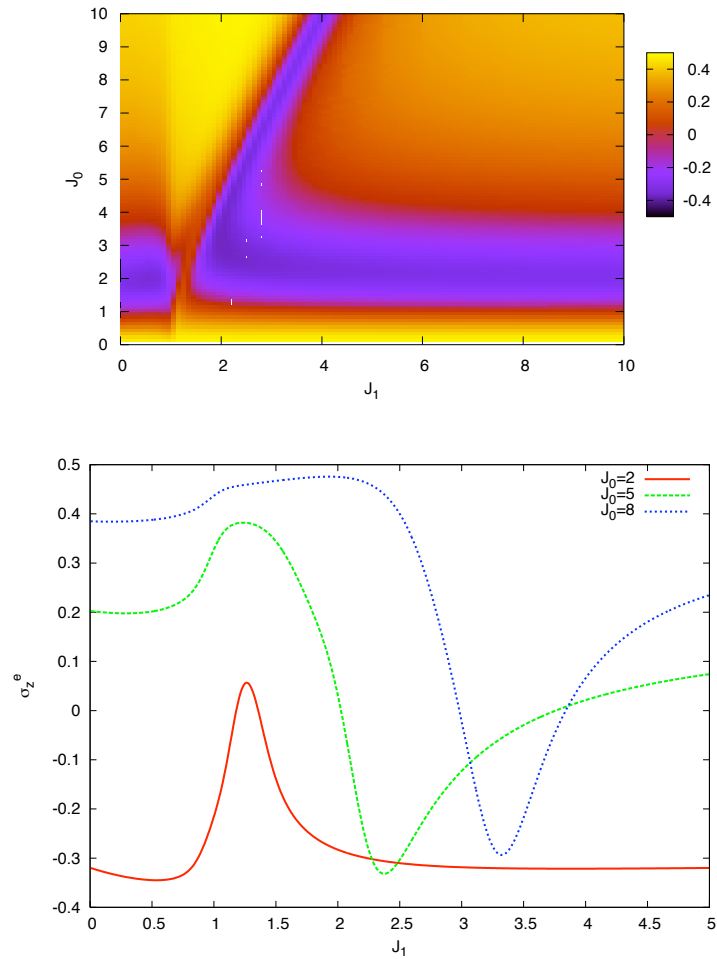


Figure 7.4: Wave packet spin long after the wave packet interacts with the local spins. Top panel: As a function of both wave packet-spin, J_0 , and spin-spin interaction, J_1 , for 2 local spins. Bottom panel: Slices through J_1 for several constant values of J_0 . Three regions are readily identified, low J_1 , very high J_1 and the ridge that is function of both J_0 and J_1 .

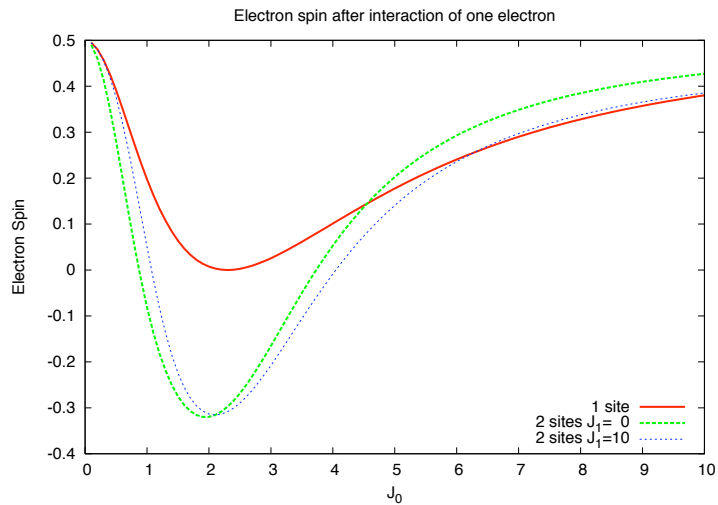


Figure 7.5: The resulting wave packet spin long after wave packet interacts with local spin(s). Results with a single local spin and two local spins are shown.

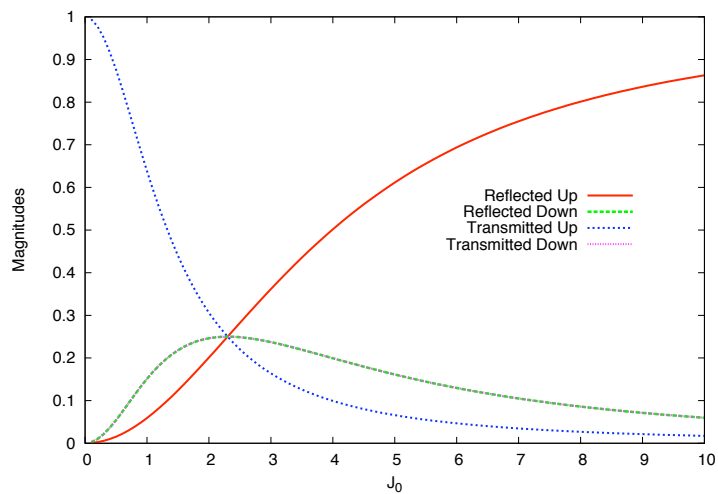


Figure 7.6: The resulting reflected and transmitted components of an incoming spin up wave packet long after wave packet interacts with local spin for a single local spin.

case is $J_1 = 0$, as the local spins are independent of one another in this case. The wave packet experiences a single local spin twice. The single local spin case has been explained elsewhere [52]. We summarize the relevant results from that analysis in Fig. 7.5. For a single local spin, we see that the interaction changes the wave packet spin. As J_0 , wave packet-spin interaction, is introduced, the down component for the z-component of the spin of the wave packet is introduced through the Kondo-like spin flip interaction. With increasing J_0 , the total z-component of the wave packet reduces down to a certain value [27]. As J_0 is increased further, the wave packet prefers to reflect back, as shown in Fig. 7.6, the interaction of the z-components (through $\sigma_z S_z$) dominates, rather than interacting with the local spin via spin flip interaction. In the case of two local spins, also plotted in Fig. 7.5, when the Kondo-like spin flip interaction is maximized, both of the local spins interact with the wave packet to a maximum change of the spin of the wave packet. Although the single spin case cannot reduce the z-component of the spin of the wave packet below zero, two local spins can reduce the spin of the wave packet much closer to pointing down. Although the change to the wave packet is larger, the change for the local spins, on average, is less. For larger values of J_0 , the barrier effect becomes stronger. As the wave packet interacts with the first spin, the reflected part, without spin flip, gets stronger, a small portion of the wave packet moves through, and interacts with the second local spin. At this point, the second local spin is unaffected by the spin-flip interaction, and pointing down, the part of the wave packet that passed through the first spin points in the same direction and does not go through another spin flip interaction. That part only experiences the barrier effect, and mostly reflects back. This reflected part from the second local spin interacts with the first local spin again to reduce the effective interaction. This secondary interaction causes the final spin of the wave packet to have a larger value than in the single spin case.

With the introduction of the Heisenberg-like spin-spin interaction between the local spins, J_1 , we note a very small change to the z-component of the spin of the wave packet until J_1 approaches t_0 , as seen in Fig. 7.7. The change in the local spin is more prominent, as shown in Fig. 7.8. For $J_1 = 0$, the two local spins behave independently from each other. For very small values of J_1 , there is communication between the local spins and this communication changes the value of the z-component of the local spins with time. Although this resembles closely the motion of precession for a classical spin under a magnetic field, the source and the interaction are very different. The wave packet interacts with the left spin first (labeled as spin 1), right spin later (labeled as spin 2). Due to this delay, the amount of spin transfer due to spin-flip interaction is smaller for the latter causing a difference in values of z-component of the local spin. The interaction that causes the oscillatory behavior is

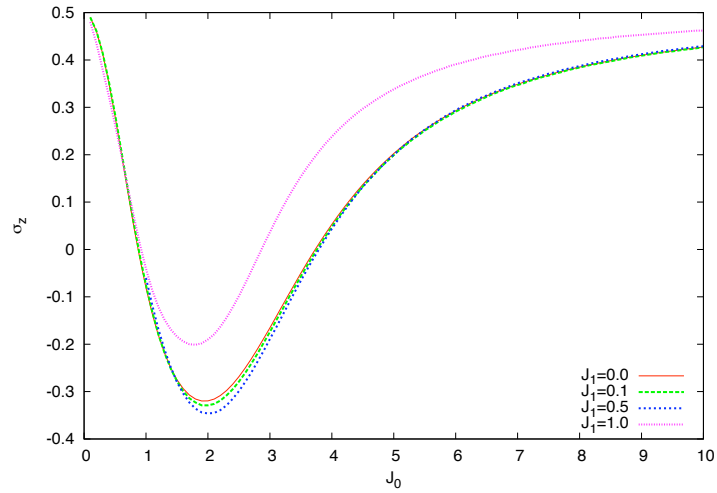


Figure 7.7: z -component of the wave packet spin for different wave packet-spin interaction strengths for several fixed J_1 . The behavior barely changes with the onset of spin-spin interaction. With larger values of J_1 , effectiveness of the spin flip interaction is reduced, following the trend shown in Fig. 7.4b.

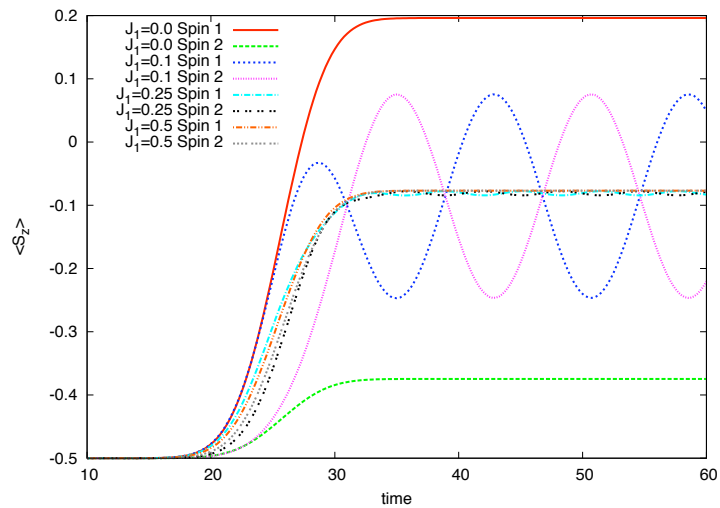


Figure 7.8: z -component of local spins for different spin-spin interaction strength for $J_0 = 2$. The introduction of spin-spin interaction changes the behavior of the local spins considerably.

the Heisenberg-like spin-spin interaction that governs the coupling between the local spins. The interaction (spin-spin interaction between the local spins) does not modify the total spin of the local spins, but, changes the value of each local spin periodically. As J_1 is increased the magnitude of the oscillations drop to zero. Even though the internal way the local spins behave changes with the change of J_1 , we see a minimal change in the value of the total z-component of the local spins, which translates to very little change for the spin of the wave packet. Around $J_0 = t_0$, there are no longer any visible oscillations. As will be shown later, the oscillations are still present though.

Concerning the wave packet, the introduction of J_1 imposes radical changes to the way the wave packet travels. In comparison to independent local spins, Fig. 7.1, there is an additional piece of the wave packet for the spin-down component of the wave packet, as shown in Figs. 7.9 and 7.10, traveling at a slower speed with respect to the incoming wave packet, that we will refer to as the additional piece. The change experienced by the incoming wave packet shows that for $J_1 = 0.25$, as shown in Fig. 7.1 vs. 7.9a, the additional piece is still present since some of the resulting magnitude of the wavepacket for $J_1 = 0$ is shifted to become the additional piece with the introduction of J_1 . The speed of the additional piece decreases with increasing J_1 , Fig. 7.9 and 7.10. The slowly moving piece exists even for $J_1 \geq t_0$ as shown with the very small bump to the left of the centre of the lattice moving very slowly a long time after the interaction in Fig. 7.13. The slowly moving piece has lower momentum, and energy, in comparison to original wave packet. Since the momentum is no longer $\frac{\pi}{2}$, broadening is observed for this component. The missing energy of the wave packet is transferred to the local spins. The oscillatory motion of the local spins is how local spins use the additional energy.

As J_1 is increased much further, neither the slower moving piece for the wave packet nor the oscillations for the local spins are present. Fig. 7.11 shows that for very large J_1 , the two local spins act together. As soon as the wave packet interacts with the first spin, the second one starts to change direction as well. For this range, comparison to the $J_1 = 0$ case is possible for the spin of the wave packet. The qualitative behavior is very similar for low to intermediate J_0 , as shown in Fig. 7.5. For large J_0 , the barrier effect that reduces the overall spin flip efficiency is not as pronounced.

For intermediate values of J_1 , there is a third region of interest that changes location as a function of both J_0 and J_1 . This region is a ridge for these parameters. This indicates that the existence of this ridge depends on both wave packet-spin and spin-spin interactions. To understand this feature, we first look at relatively high value of wave packet-spin coupling, $J_0 = 8$. Fig. 7.12 shows that for a set of interaction

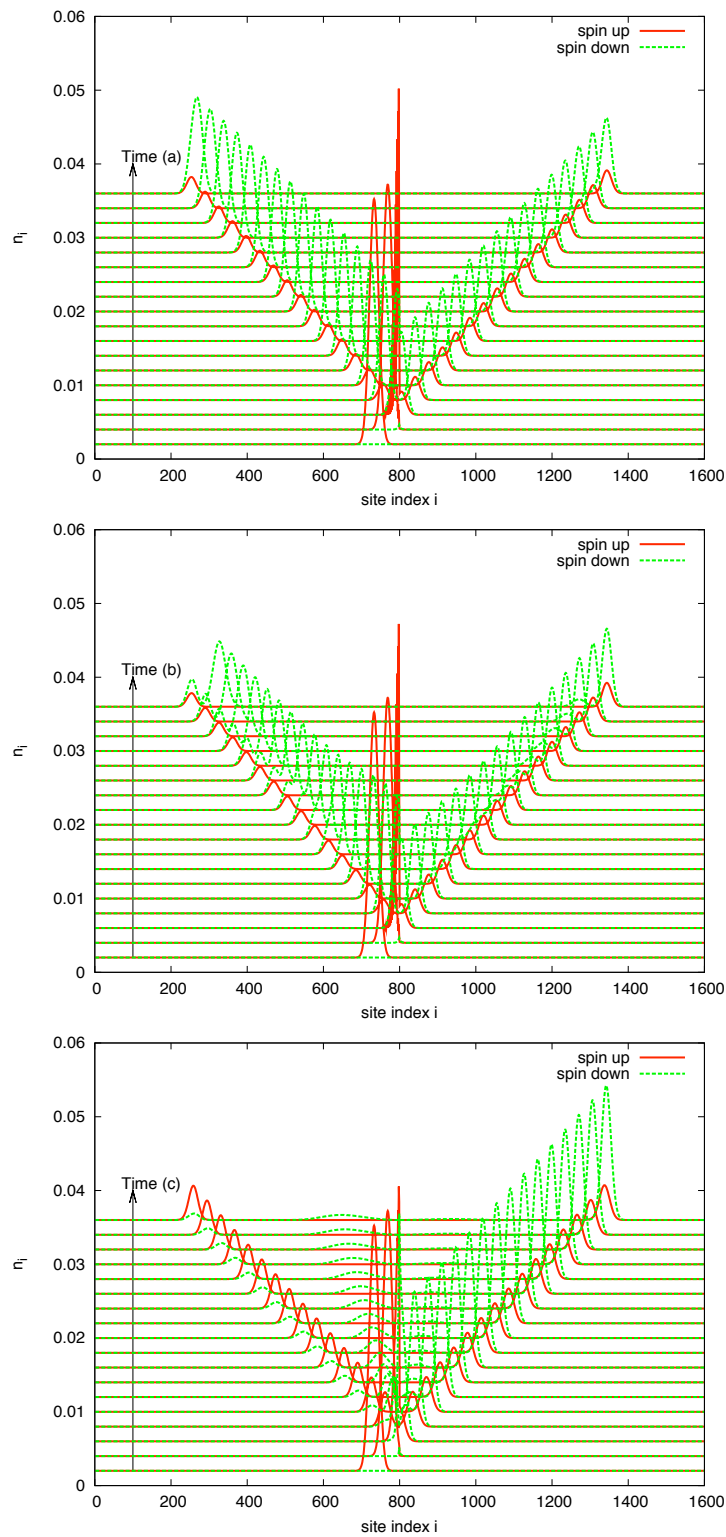


Figure 7.9: Time evolution of a wave packet, interacting with two local spins with $J_0 = 2.0$ with the same conditions as Fig. 7.1. The cases shown are a) $J_1 = 0.25$, b) $J_1 = 0.5$ and c) $J_1 = 1.0$.

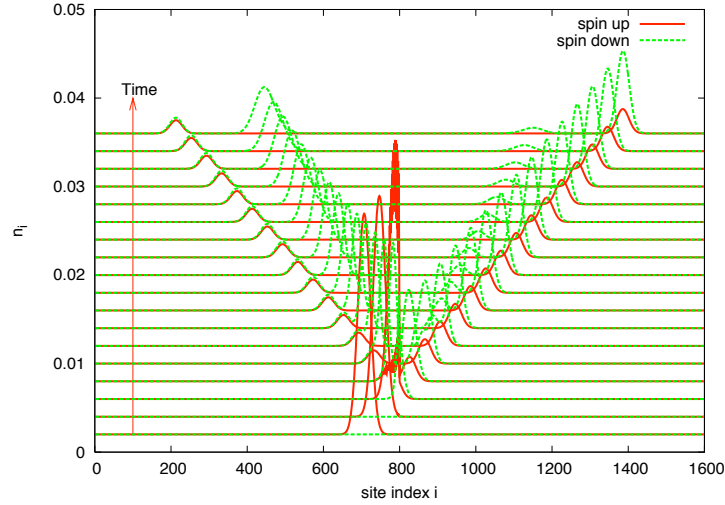


Figure 7.10: Time evolution of a wave packet, interacting with two local spins with $J_0 = 2.0$, and $J_1 = 0.8$ with the same conditions as Fig. 7.1.

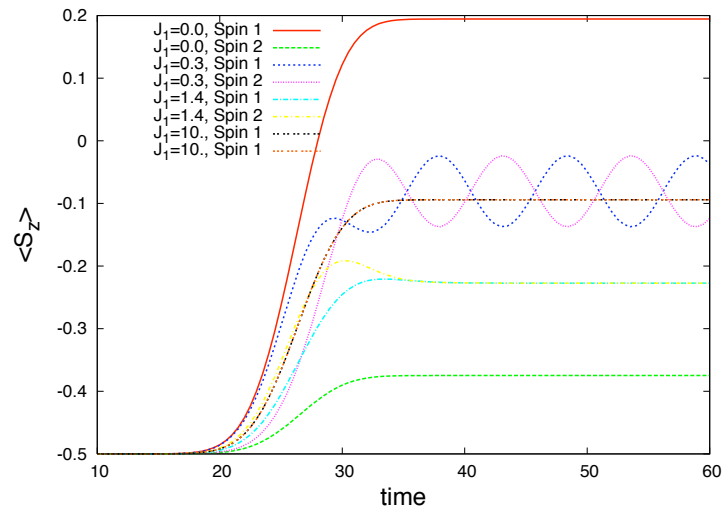


Figure 7.11: z -component of local spins for different spin-spin interaction strength for $J_0 = 2$. For $J_1 = 10$, two spins have the same value. Spin numbers are given with respect to the order they interact with the incoming spin up wave packet.

parameters, J_0 and J_1 , within the ridge, for the wave packet, there is a state that forms at the local spin sites. This state, shown as a small peak centered around the local spins in the plot, forms a peak only for the spin down component of the wave packet and loses its weight exponentially over time since with linear time evolution the maximum of the peak decreases linearly on a logarithmic scale, and the weight transferred to the moving piece decreases linearly. Even though the state itself is a pure “spin transfer” state, the weight decays as both spin down and spin up. Therefore, even though only the spin down part of the wave packet forms this state, just a portion of it leaves the local spin area as spin down. We repeat the same calculation for lower wave packet-spin interaction, $J_0 = 2$, in Fig. 7.13. We again note the existence of the peak around the local sites. Similar to low J_1 behavior, this state is pure spin-down state. However, in contrast, it forms only around the local spins and does not move. Looking at the time evolution of the local spins, Fig. 7.11, we see that the interaction pushes the values of the z-component of both local spins higher than their final value, especially the second spin. This is consistent with the interpretation that the spin down state of the wave packet around the local spins decays as both spin up and spin down packets. The two local spins act differently at the moment of interaction but combine to the same value afterwards. One interpretation for the origin of this ridge or the peak of the wave packet around the local spins is the following. The combination of certain J_0 and J_1 enhances the transfer of energy of the wave packet completely to the local spins, the wave packet forms a stationary state and receives the energy back to move with the momentum of the initial wave packet. It is important to note at this point, as shown in Fig. 7.14, for different combinations of J_0 and J_1 , the z-components of the local spins qualitatively show the same trends in time. Initially, the spin further from the wave packet starts to flip which is followed by the first spin. The second spin goes higher than the long time limit. At the end, the values of the z-component of both local spins are same. The reduction is much more pronounced for lower value of J_0 , where, without the ridge, we would have high spin flip interaction. The existence of the ridge, and the decay of the weight as both spin up and spin down, reduces the effective spin-flip interaction. Because of this, we note an increase for the value of the z-component of the wave packet for $J_0 = 2$ around $J_1 = 1.4$ while we see a dip for $J_0 = 8$ around $J_1 = 3.1$.

Another important aspect of the ridge is the linear tail of the wave packet on the logarithmic scale. This corresponds to an exponential diminishing of the weight of the localized peak at the local spins. For comparison, the time evolution of spin up and spin down components of the wave packet for a larger value of J_1 , or smaller value of J_0 in comparison to Fig. 7.12, is plotted in Fig. 7.15. This value, $J_1 = 3.1$ also corresponds to the ridge for $J_0 = 8$. In this lower case of wave packet-local spin

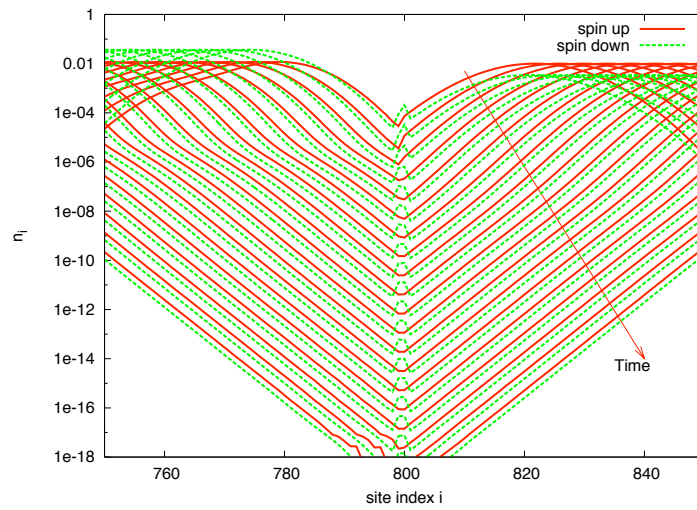


Figure 7.12: Time evolution of wave packet, interacting with two local spins with $J_0 = 8.0$, and $J_1 = 3.1$, short after the interaction. Note the logarithmic scale for y-axis. The wide peaks to the sides of the graph are reflected and transmitted components of the wave packet. $a = 6$ is used for this plot. The linear trend around the local spins is indicative of an exponential decay of the weight around the local spins.

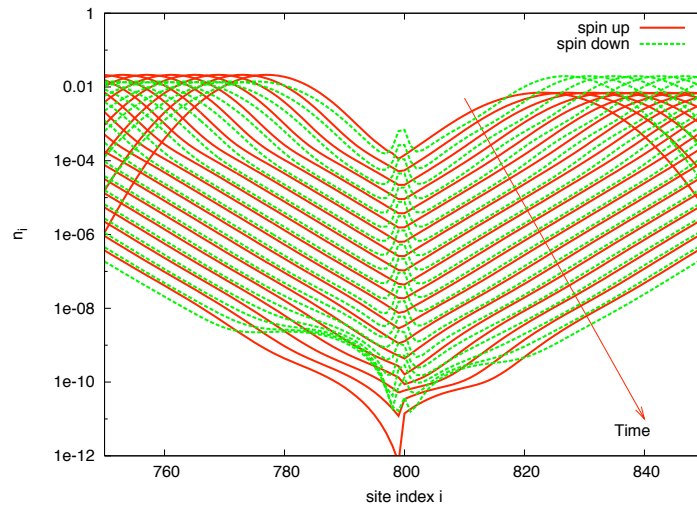


Figure 7.13: Time evolution of wave packet, interacting with two local spins with $J_0 = 2.0$, and $J_1 = 1.4$, short after the interaction. Note the logarithmic scale for y-axis. The wide peaks to the sides of the graph are reflected and transmitted components of the wave packet. $a = 6$ is used for this plot. The linear trend around the local spins is indicative of an exponential decay of the weight around the local spins. There is very small slow moving packet revealed at late times.

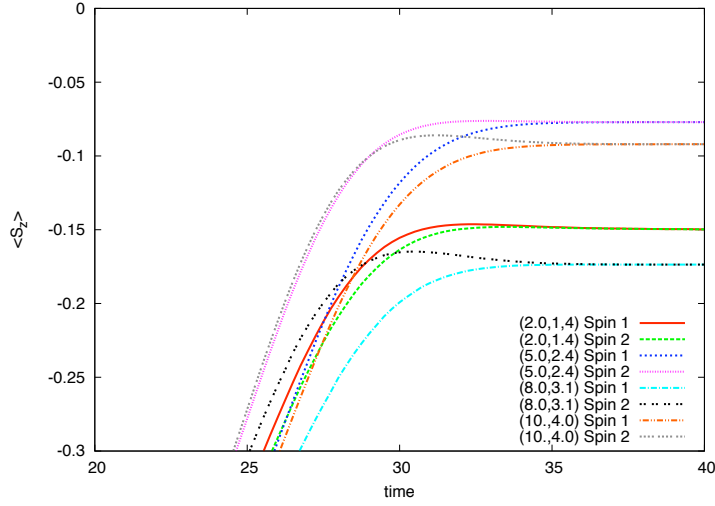


Figure 7.14: Time evolution of the z component of the local spins for 2 sites. The cases along the ridge is shown. The legend is (J_0, J_1) , spin number in order of interaction with the wave packet. The final value of S_z is same for both spins. The second spin changes first.

interaction, $J_0 = 2$, we expect similar values of z-component of the wave packet, σ_z . However, the way the wave packet interacts is very different from the other two cases, Fig. 7.12 and 7.13. This case does not correspond to the ridge, and the peak is not present at the local spins, nor the exponential decay of the weight. Instead, we observe multiple reflections off of the local spins, indicated by the multiple peaks for the reflected and transmitted parts.

7.4 Numerical Results with Proper Basis States

In the previous section, we have analyzed individual components of the system. We have treated the incoming wave packet and the local spins separately, and tried to understand how the interaction modified each of them. However, in quantum mechanics, we know that if two systems interact, they stay coupled and need to be treated together as a single system.

In the case presented in this chapter, two separate spin systems interact. The number of basis states representing the total system, in spin space, changes depending on the number of local spins and the spin value of each local spin. In most general form, the system has $2 \times (2S + 1)^{N_s}$ states with S the spin degree of freedom of each local spin, N_s is number of local spins, the multiplier 2 is for the spin of the incoming wave packet. Since the Hamiltonian does not modify the z-component of the total spin of the system, we can group these basis states using the total z-component. For

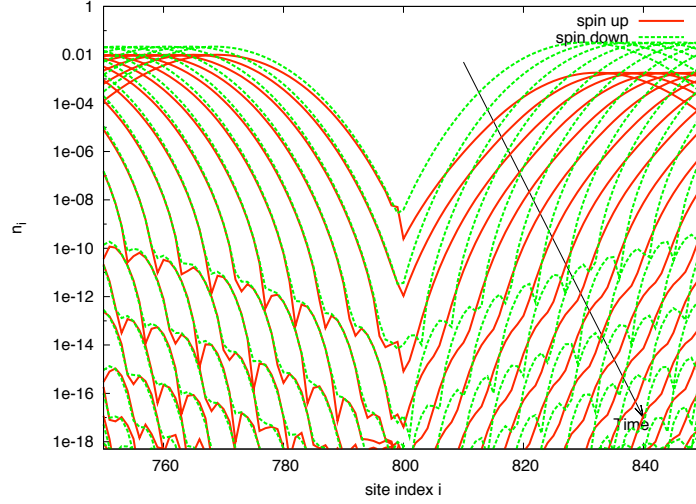


Figure 7.15: Time evolution of wave packet, interacting with two local spins with $J_0 = 2.0$, and $J_1 = 3.1$, short after the interaction. Note the logarithmic scale for y-axis. $a = 6$ is used for this plot. Since this set of parameters is away from the ridge, multiple reflections are observed instead of exponential decay.

the problem we are interested in, we have an incoming wave packet with spin up and ferromagnetic local spins all pointing down with total z-component, $J_z = 0.5 - N_s \times S$. The spin flip interaction can change the z-component of the spin of the wave packet by changing the z-component of the spin of the local spins. For the case we analyze here, having two local spins, each with $S = 1/2$, the three spin states are, in Dirac notation, $|\uparrow\downarrow\downarrow\rangle$, (initial configuration), $|\downarrow\uparrow\downarrow\rangle$ (obtained through spin flip interaction with the first spin), and $|\downarrow\downarrow\uparrow\rangle$ (obtained through spin flip interaction with the second spin). In this representation, the total z-component is always $J_z = -\frac{1}{2}$. In this notation, these three basis states are rewritten as:

$$|\Psi_1\rangle = \frac{1}{\sqrt{3}}(|\downarrow\downarrow\uparrow\rangle + |\downarrow\uparrow\downarrow\rangle + |\uparrow\downarrow\downarrow\rangle) \quad (7.10)$$

$$|\Psi_2\rangle = \frac{1}{\sqrt{6}}(|\downarrow\downarrow\uparrow\rangle + |\downarrow\uparrow\downarrow\rangle - 2|\uparrow\downarrow\downarrow\rangle) \quad (7.11)$$

$$|\Psi_3\rangle = \frac{1}{\sqrt{2}}(|\downarrow\downarrow\uparrow\rangle - |\downarrow\uparrow\downarrow\rangle). \quad (7.12)$$

Any wave packet can be written as:

$$|\Psi(x)\rangle = h(x)|\Psi_1\rangle + f(x)|\Psi_2\rangle + g(x)|\Psi_3\rangle \quad (7.13)$$

where $h(x)$, $f(x)$ and $g(x)$ are coefficients in the spatial subspace of the Hilbert space

for each of the basis states in the spin subspace. For total S , $|\Psi_1\rangle$ represents $S = 3/2$ quartet, $|\Psi_2\rangle$ and $|\Psi_3\rangle$ represent $S = 1/2$ doublet.

We start by repeating the analysis done in the previous section for the coefficients in the proper basis set. In Fig. 7.16, we plot the coefficients, h, f, g for a set of J_1 values with $J_0 = 2$. In the previous section, we have seen that with the change of J_1 , a slower moving piece was formed and the magnitude of reflected and transmitted parts changed considerably, as shown in Figs. 7.1, 7.9 and 7.10. For $J_1 = 1.4$, we have observed a localized peak forming at the local sites, Fig. 7.13. Each coefficient behaves very differently. $h(x)$ shows no change with the change of J_1 , showing no dependence on J_1 . $f(x)$ shows a strong dependence on J_1 for the magnitude of both the reflected and the transmitted components. On the other hand, there is no change to the speed, and hence the energy, of the resulting wave packet components. For $g(x)$, we observe very strong changes in the behavior with the change of J_1 . With increasing J_1 , the $g(x)$ component of the wave packet travels more slowly. In addition, the magnitude of the coefficient changes considerably. For $J_1 = 1.4$, the $g(x)$ component is localized to the local spin sites. The state exists as a temporary weight that does not move, and dissipates. We also note that the basis state $|\Psi_3\rangle$ does not have any weight at $t = 0$, since this basis state represents only the spin down component of the wave packet. It exists purely through the interaction of the other two components of the wave packet with the local spins. Since $h(x)$ does not show any dependence on J_1 , and the total wave function is normalized, we can conclude that $h(x)$ does not cause the existence of $g(x)$. On the other hand, the strong J_1 dependence $f(x)$ indicates that, due to normalization, some of the weight is transferred to the component $g(x)$. With $J_1 = 1.4$, the temporary weight around the local spins for the component $g(x)$, is transferred back to $f(x)$, giving $f(x)$ its original weight. The component $g(x)$ exists only around the local spins for large values of J_1 . The temporary magnitude of $g(x)$ is largest around the ridge, and decays over time.

The existence and speed of $g(x)$ identifies two regions in the $J_0 - J_1$ parameter space for $g(x)$. For one region, $g(x)$ is introduced with the wave packet spin interaction, and travels with a lower speed than the other components. For the other, $g(x)$ exists temporarily around the local spins, then travels as the component $f(x)$. In Fig. 7.17, we plot $|g(x)|^2$ with local spins separated 20 sites apart. On a logarithmic scale, the linear tails are indicative of the existence of a bound state for a range of values of J_0 . When $g(x)$ moves, with slower speed, it exists for any time after the interaction whereas if $g(x)$ exists only around the local spins, it will exist for a short time after the interaction of the wave packet with the local spins. We plot these magnitudes of $g(x)$ in two areas in Figs. 7.18 and 7.19 as a function of J_0 and J_1 . For $J_1 \geq 1$, in Fig. 7.18, even though the localized temporary component exists everywhere, we see

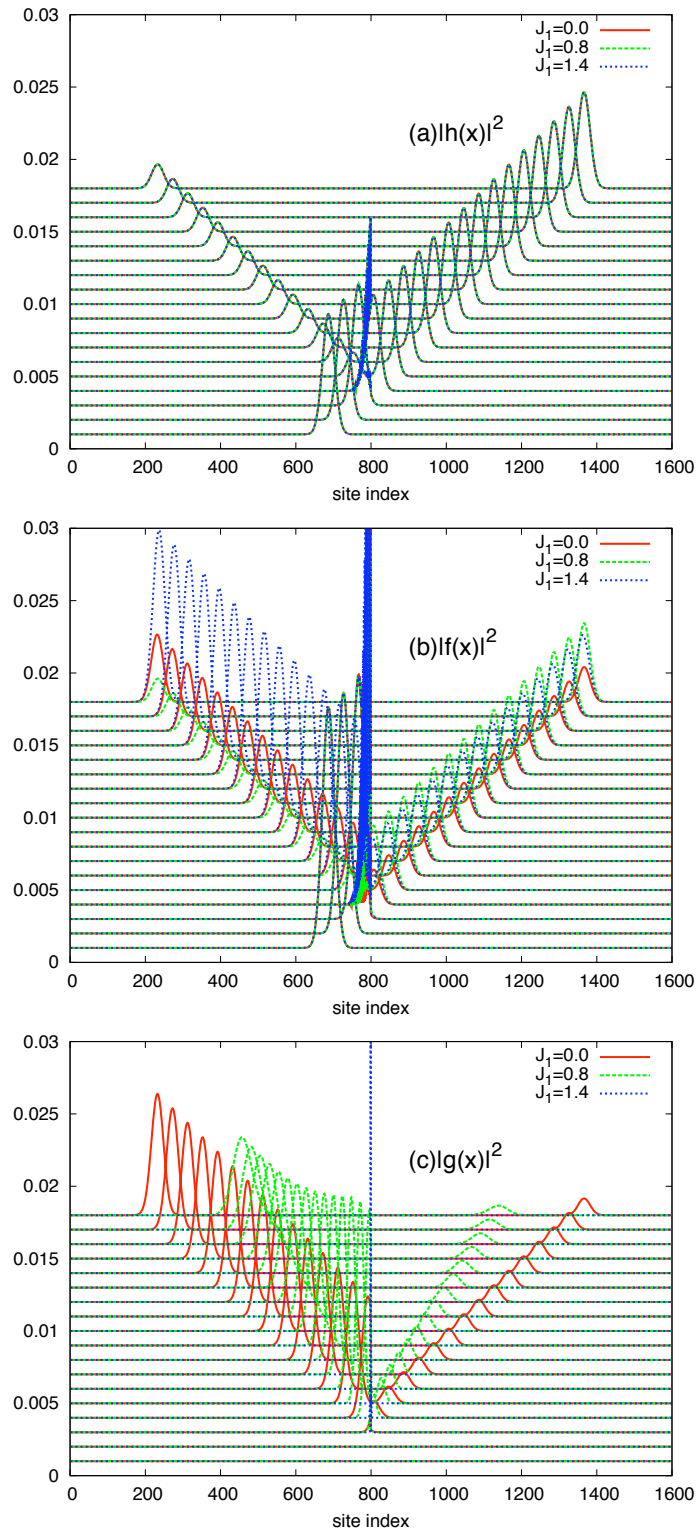


Figure 7.16: Time evolution of wave packet, interacting with two local spins with $J_0 = 2.0$, The spin symmetric states a) $|h(x)|^2$, b) $|f(x)|^2$ and c) $|g(x)|^2$, are shown.

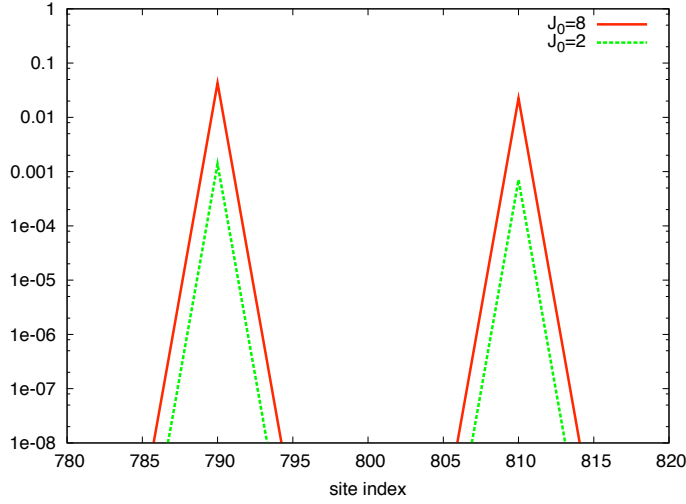


Figure 7.17: The component $|g(x)|^2$ right after the wave packet interacts with the local spins. We use $J_1 = 3.1$ and local spins are at sites 790 and 810. Note the logarithmic scale for the y-axis. The results correspond to earliest times in Figs. 7.12 and 7.15.

that the magnitude of this component is maximum along the ridge. Even though we do not see the ridge around $J_1 \sim 1$ in Fig. 7.4, the state $g(x)$ exists, and, in fact, the maximal, in that region. In Fig. 7.19, we note that the overall cutoff point, where we lose the weight of the slowly moving piece, for the existence of the slowly moving piece is independent of J_0 . It vanishes around $J_1 \sim 1$.

7.5 Analytical Approach

Please note that the analysis done in this section utilizes the results of Appendices B and C.

In order to approach what we have observed numerically from an analytical point of view, we look at the picture as interaction of 3 spins, where one of the spins (wave packet in our case) can travel on a surface. We write the Hamiltonian (Eq. 7.1), in continuum notation as [58]:

$$H = \frac{\hat{P}^2}{2m} - 2J_0[\hat{\sigma} \cdot \hat{S}_1\delta(x) + \hat{\sigma} \cdot \hat{S}_2\delta(x - a)] - 2J_1\hat{S}_1 \cdot \hat{S}_2, \quad (7.14)$$

where \hat{P} is the momentum operator of the moving spin and two local spins are located at $x = 0$ and $x = a$. As we have done previously, we will restrict our analysis to one-dimension for relevance and simplicity, but arguments for extending to higher dimensions will be given.

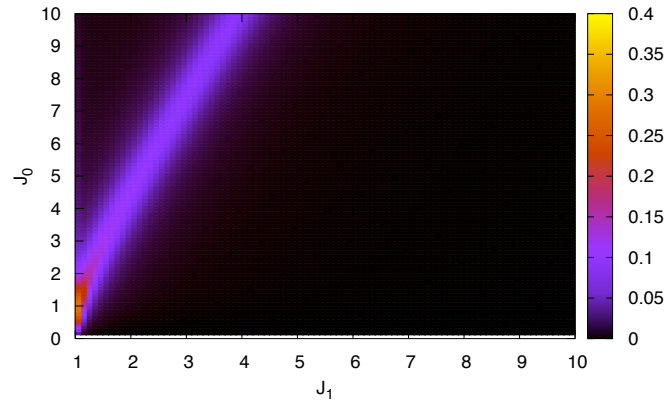


Figure 7.18: The component $|g(x)|^2$ integrated over the entire lattice right after the wave packet interacts with the local spins, using the same time step as Fig. 7.17. Note that scale for J_1 starts at one.

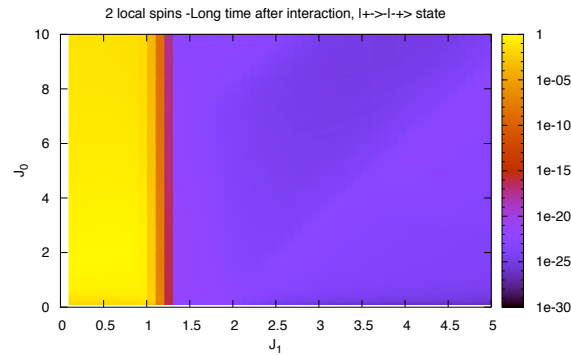


Figure 7.19: The component $|g(x)|^2$ integrated over the entire lattice long after the wave packet interacts with the local spins. The magnitude changes with J_0 , but we are only interested in existence of $g(x)$. We plot on a logarithmic scale to hide the magnitude change for the slowly moving piece.

In one dimension, the Schrodinger equation for this Hamiltonian for each of these components becomes:

$$\begin{aligned}
-\frac{\hbar^2}{2m} \frac{d^2 h(x)}{dx^2} - 2J_0 \frac{\hbar^2}{4} (\delta(x) + \delta(x-a)) h(x) &= \epsilon_{el} h(x), \\
-\frac{\hbar^2}{2m} \frac{d^2 f(x)}{dx^2} + J_0 \frac{\hbar^2}{2} [\delta(x)(2f(x) - \sqrt{3}g(x)) \\
&\quad + \delta(x-a)(2f(x) + \sqrt{3}g(x))] &= \epsilon_{el} f(x), \\
-\frac{\hbar^2}{2m} \frac{d^2 g(x)}{dx^2} - \sqrt{3}J_0 \frac{\hbar^2}{2} [\delta(x) - \delta(x-a)] f(x) &= (\epsilon_{el} - 2J_1 \hbar^2) g(x),
\end{aligned} \tag{7.15}$$

where ϵ_{el} is the energy of the incoming wave packet (only), and the energy of the corresponding component. We note that there is no J_1 dependence for $h(x)$. For $f(x)$, there is no apparent dependence on J_1 as there is no explicit term with J_1 . The equation for $g(x)$ has the term related to J_1 . In our calculations $g(x)$ emerges through the coupling to the component $f(x)$ at the delta functions. Some portion of the component $f(x)$ is transferred to the component $g(x)$. Through this interaction, the component $f(x)$ depends on J_1 . This is the mechanism we observed in our numerical calculations, as shown in Fig. 7.16. The energy of each term, the coefficient of the right hand side term, is different as well. The wave packet energy, ϵ_{el} , is the energy of the first two equations, so there is no change to the energy of the initial wave packet for these two components. The energy of $g(x)$, on the other hand, depends on J_1 . As J_1 gets larger, the energy, and therefore the magnitude of the momentum, of the component reduces. If J_1 is larger than $\frac{\epsilon_{el}}{2\hbar^2}$, the energy of the component $g(x)$ become negative. If a state has negative energy, that state has zero momentum, and the state is bound. In our case, since $g(x)$ emerges at the local spins, the bound state is expected to occur around the local spins, as shown in Fig. 7.17. We have a wave packet moving towards the local spins, and after the interaction it moves away. So we do not have a constant supply of weight to the bound state. After the wave packet leaves the local spin area, the remaining part, the bound state, decays into the component $f(x)$ and propagates as that component, as shown in Figs 7.12, 7.13 and 7.14.

At this point we solve the Schrodinger equations to explore the features we have just mentioned for the component $g(x)$. We define three regions of interest and label them as shown in Fig. 7.20.

With this formalism, for $\epsilon_{el} > 2J_1 \hbar^2$, we see that the momentum of the component

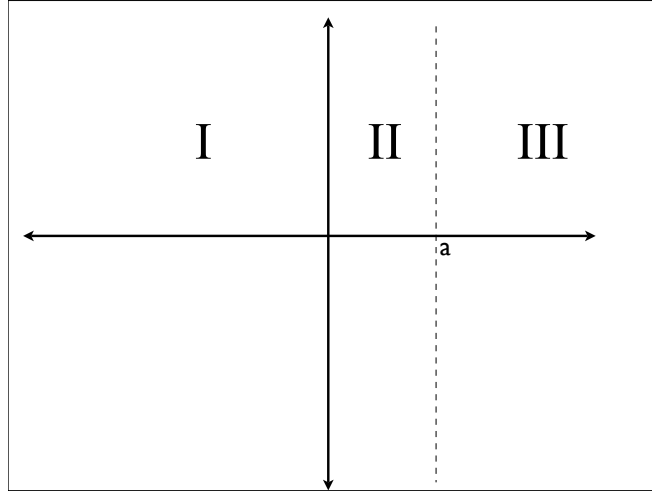


Figure 7.20: Division of one dimensional space. The Hamiltonian has two delta functions at $x = 0$ and $x = a$.

$g(x)$ is $k = \sqrt{2m(\frac{\epsilon_{el}}{\hbar^2} - 2J_1)}$, and the wave function can be written as:

$$g(x) = \left\{ \begin{array}{ll} g_I(x) = A_k e^{-ikx} & x < 0 \\ g_{II}(x) = B_k e^{ikx} + C_k e^{-ikx} & 0 < x < a \\ g_{III}(x) = D_k e^{ikx} & a < x \end{array} \right\}, \quad (7.16)$$

whereas for $\epsilon_{el} < 2J_1 \hbar^2$, the wave function becomes:

$$g(x) = \left\{ \begin{array}{ll} g_I(x) = A e^{Qx} & x < 0 \\ g_{II}(x) = B e^{-Qx} + C e^{Qx} & 0 < x < a \\ g_{III}(x) = D e^{-Qx} & a < x \end{array} \right\}, \quad (7.17)$$

with $Q = \sqrt{2m(2J_1 - \frac{\epsilon_{el}}{\hbar^2})}$. The first wave function exists and moves everywhere in the system. The second wavefunction defines a bound state. This shows us that there is a bound state for some range of spin-spin coupling and it is possible to trap (indefinitely for plane wave) some part of the wave packet at the site of the local spins. We are interested in existence and magnitude of the bound state to see if having that state is possible.

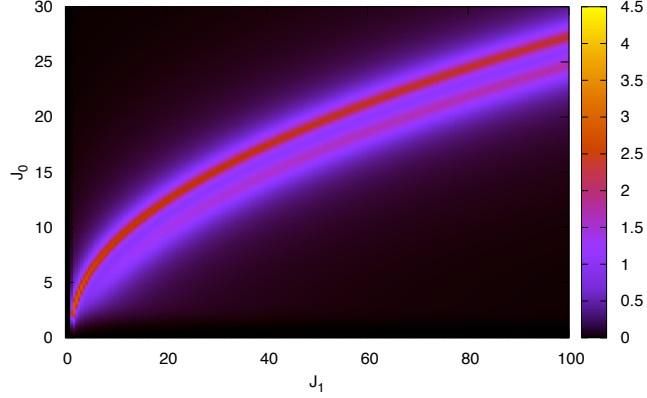


Figure 7.21: The weight transferred to the component $g(x)$ from the incoming plane wave component X of $f(x)$. Specifically, the component $|\frac{B}{X}|^2$ is shown. Only the negative energy portion is shown with $a = 1$ and $p = 2$. Two ridges are shown with one much more pronounced than the other. The maximum amplitude occurs for low J_1 .

We use the plane wave definition of $g(x)$ along with;

$$f(x) = \begin{cases} f_I(x) = X e^{ipx} + Y e^{-ipx} & x < 0 \\ f_{II}(x) = T e^{ipx} + Z e^{-ipx} & 0 < x < a \\ f_{III}(x) = V e^{ipx} & a < x \end{cases}, \quad (7.18)$$

for $f(x)$ with $p = \sqrt{\frac{2m\epsilon_{el}}{\hbar}}$, we can solve the relevant equations to find each coefficient of $f(x)$ and $g(x)$ in terms of the incoming part X . As shown in Appendix B, the rate of weight transfer from $f(x)$ to $g(x)$ is given by the coefficient B in terms of X ;

$$B = \frac{\frac{\sqrt{3}}{2} \frac{J_0}{k} (1 + \Gamma)}{(\gamma_2 - \gamma_1 \Gamma)} X, \quad (7.19)$$

with;

$$\Gamma = \left(\frac{\frac{-J_0}{ip} - \frac{3}{4} \frac{J_0^2}{ipk} e^{ka-ipa} + \frac{3}{4} \frac{J_0^2}{ipk}}{1 + \frac{J_0}{ip} + \frac{3}{4} \frac{J_0^2}{ipk} e^{ka+ipa} - \frac{3}{4} \frac{J_0^2}{ipk}} \right) e^{2ipa} = \frac{\gamma_1}{\gamma_2} e^{2ipa}. \quad (7.20)$$

Up to this point, we have kept the arguments general. We have not specified any corresponding value to the numerical calculations we have performed using wave packets. The Hamiltonian used in the numerical analysis was in tight binding where all energy scales are given by the hopping parameter t_0 . In the plane wave approximation, we use a continuum free space Hamiltonian where we do not have a similar unit.

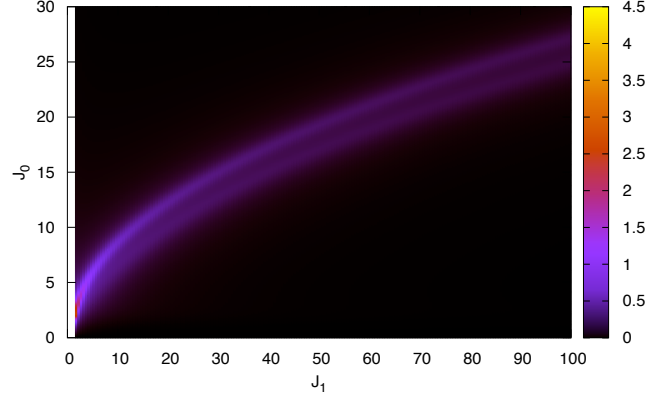


Figure 7.22: The total weight of the component $g(x)$ as generated from the incoming plane wave component X of $f(x)$. Only the negative energy portion is shown with $a = 1$ and $p = 2$. Two ridges are shown following closely with Fig. 7.21. The maximum amplitude occurs for low J_1 .

Therefore, any direct comparison to the results of the numerical calculations is not straightforward. We have one condition that needs to be satisfied if we are to compare the two methods. In Fig 7.18, the slowly moving type of $g(x)$ exists up to $J_1 \sim t_0$ and this determines where the right hand side of the Schrodinger equation for $g(x)$ to change sign, though not satisfying all requirements, that the energy of $g(x)$ should be zero around $J_1 = 1$. We set the energy of $f(x)$, and $h(x)$, to $\epsilon_{el} = 2\hbar^2$, and since we put the local spins next to each other, we have $a = 1$. In Fig. 7.21, we plot the magnitude of B in terms of X , calculated using Eq. 7.19 with the mentioned constraints. We note the formation of the ridge as a function of both J_1 and J_0 . Since this plot represents the total weight transferred to the bound state $g(x)$, it also represents where the maximum spin flip would occur. In Fig. 7.22, we also plot the total magnitude of $g(x)$, and observe the same structure. The spin flip forms two ridges unlike the single ridge we observe in our numerical calculations. We attribute this discrepancy to the fact that we use a wave packet, which is confined to a small space within a tight binding model. To complete the analysis, we plot the z -component of the wave packet:

$$\langle \sigma_z \rangle = \frac{5}{18} - \frac{2\sqrt{2}}{9} \text{Re}(B^*Y + E^*V) \quad (7.21)$$

in Fig. 7.23. The three regions we described at the beginning of this chapter are also present here. Low J_1 region behavior, very high J_1 and the J_0 and J_1 dependent

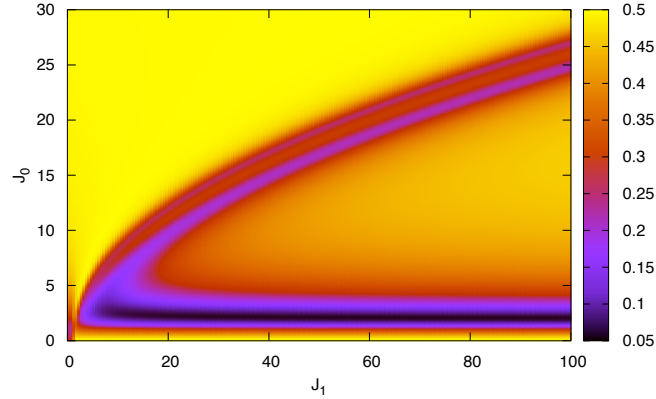


Figure 7.23: z -component of the spin current modeled by a plane wave. For qualitative comparison to Fig. 7.4. The three regions are again present. Low J_1 behavior, very high J_1 and the ridge that is a function of both J_0 and J_1 show similar behavior to wave packet counterparts. There are two ridges instead of one because we have a well defined momentum in this case for the incoming portion of the spin current.

ridge all follow the same trend as Fig. 7.4.

7.6 Generalizations

So far, we have focused our analysis to two local sites each with $S = 1/2$ in one dimension. However, all of these specific choices are not unique. In this section, we will show generalizations to arbitrary values.

We begin with dimensionality. In our equations, we have used one dimensional systems. However, the bound state is formed through the spin-spin interaction, and does not depend on the motion of the wave packet. The kinetic energy term changes with dimensionality. With the change of momentum operator, \hat{P} , ϵ_{el} will change, so will the point the energy of $g(x)$ becomes negative. With negativity still possible for the right hand side of the Schrodinger equation, we expect the bound state to exist in higher dimensions.

We have already shown that the ridge formation is present for longer local spin chains. Because we have a larger number of spin states (total number of spin states is $N_s + 1$), we have more combinations to have the bound state. As an example, we show the results for 3 local spins in Fig. 7.24. In addition to very similar behavior, we see additional features due to formation of similar bound states and ridges. We have shown in Fig. 7.3 that longer spin chains follow similar trends.

In Appendix B, we have generalized Eq. 7.14 for arbitrary S with all local spins initially having $S_z = -S$. Due to symmetry of the problem, the proper basis states we introduced in Sec. 7.4 are still the proper ones with the local spins replaced with the corresponding values. The Schrodinger equations for arbitrary spins for each basis state are:

$$\begin{aligned}
-\frac{2J_0\hbar^2}{2\sqrt{3}}[(a_{h1}h(x) + b_{h1}f(x) + c_{h1}g(x))\delta(x) + \delta(x-a)(a_{h2}h(x) + b_{h2}f(x) + c_{h2}g(x))] \\
= \frac{\hbar^2}{2m} \frac{d^2h(x)}{dx^2} + \epsilon_{el}h(x),
\end{aligned} \tag{7.22}$$

$$\begin{aligned}
-\frac{2J_0\hbar^2}{2\sqrt{3}}[(a_{f1}h(x) + b_{f1}f(x) + c_{f1}g(x))\delta(x) + \delta(x-a)(a_{f2}h(x) + b_{f2}f(x) + c_{f2}g(x))] \\
= \frac{\hbar^2}{2m} \frac{d^2f(x)}{dx^2} + \epsilon_{el}f(x),
\end{aligned} \tag{7.23}$$

$$\begin{aligned}
-\frac{2J_0\hbar^2}{2\sqrt{3}}[(a_{g1}h(x) + b_{g1}f(x) + c_{g1}g(x))\delta(x) + \delta(x-a)(a_{g2}h(x) + b_{g2}f(x) + c_{g2}g(x))] \\
= \frac{\hbar^2}{2m} \frac{d^2g(x)}{dx^2} + (\epsilon_{el} - 4J_1\hbar^2 S_z)g(x).
\end{aligned} \tag{7.24}$$

The coefficients a 's, b 's and c 's are given in Appendix B. These equations suggest that in general, all three basis states are coupled. For any value of S , the first two components have energy independent of J_1 whereas the state $g(x)$ has changing energy. With changing S_z , or S , the location of zero energy changes.

7.7 Conclusions

In this chapter, we have analyzed the interaction of a spin current with a magnetic layer in a fully quantum mechanical point of view. We have simulated the effect of the spin current using a wave packet with a certain spin and momentum. The magnetic layer has been simulated by local spins that interact with each other. The two subsystems interact through a Kondo-like spin flip interaction with magnitude given by J_0 that can modify the spin of the wave packet and the spin of the local spins. The ferromagnetically aligned local spins interact with each other through the Heisenberg

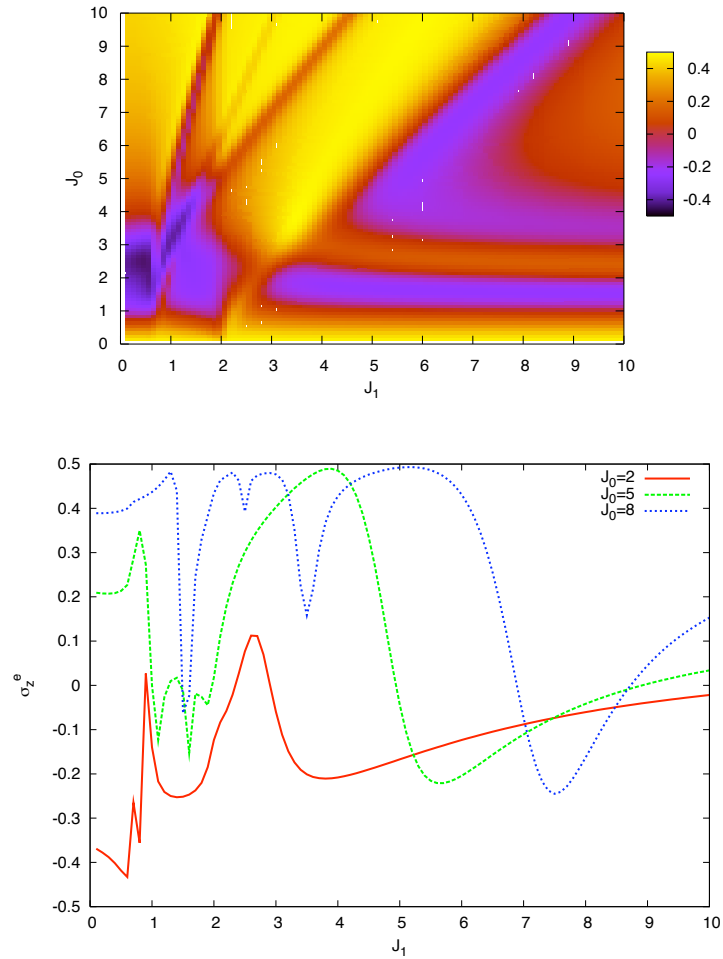


Figure 7.24: Wave packet spin long after the wave packet interacts with the local spins. Top panel: As a function of both wave packet-spin, J_0 , and spin-spin interaction, J_1 , for 3 local spins. Bottom panel: Slices through J_1 for several constant values of J_0 . Three regions are readily identified. Low J_1 , very high J_1 and the ridges, there are several in this case, that is function of both J_0 and J_1 .

interaction with magnitude J_1 . Numerical simulations have been performed on a one-dimensional lattice. We have shown that the spin flip interaction shows non-classical behavior in both wave packet-local spin interaction, J_0 , and spin-spin interaction, J_1 . As a function of J_0 , the spin flip interaction changes z-component of spin of both the wave packet and the local spin(s) considerably for intermediate values of J_0 . As J_0 gets larger, the potential barrier component becomes more important. This is true for any number of local spins when the local spins are independent. A similar behavior is observed when the local spins interact with very large J_1 . In addition to these regions, we have shown that energy transfer to the local spins from the wave packet is also possible and this energy transfer can cause the formation of a slower component of the wave packet. For larger J_1 , the slower piece becomes localized. We have shown that this localized state is present for a combination of J_0 and J_1 . For two local spins, the localized state forms a ridge in the J_0 - J_1 parameter space, and along this ridge the spin flip interaction is considerably enhanced. For larger number of spins, additional ridges are formed, and as a function of J_1 , for a constant J_0 , wiggle-like change is observed. For the source of the change in movement of the wave packet and the formation of a localized state, we focused on the two local spin case, and showed that if we use the proper basis states, one of the states that is not present for the incoming wave packet, $|\Psi_3\rangle$, is responsible for both. The energy of $|\Psi_3\rangle$ decreases with increasing J_1 and for large enough J_1 , the energy becomes negative, making the state $|\Psi_3\rangle$ a bound state. Even though most of the analysis is carried out with two local spins with $S = 1/2$ in one dimension, generalization arguments to higher dimension, longer local spin chains and higher S values have been shown.

These results are important from an application of spintronics point of view, as, currently, a classical view of spin flip interaction is used in manufacturing devices that utilizes spin currents interacting with magnetic layers. With each of these layers containing a large number of spins, the behavior of the magnetic layer can be approximated classically. With the demand for smaller units for magnetic layers, quantum effects become more and more important. With small enough systems, we expect the behavior explained in this chapter to become an important part of manufacturing devices with non-negligable quantum effects. Even though quantum effects tend to be washed out by large number of magnetic atoms for mesoscopic magnetic layers, with small number of magnetic atoms, averaging is not possible. Hence, interaction of spin current with each magnetic atom and coupling of the magnetic atoms will dominate when the large number approximation does not hold. We expect this to start to occur with 30-100 atoms.

Chapter 8

Conclusions

In this thesis, we have looked at the interaction of itinerant fermions with localized degrees of freedom using one dimensional models in real space. With the improvements of the real space computational methods, analysis of systems with large degrees of freedom is possible in real space using quasi exact methods. We have used two such methods, namely density matrix renormalization group (DMRG) and expansion of the operators and observables using orthonormal Chebyshev polynomials.

The interaction of the fermions with the independent local degrees of freedom (pseudo-spins) gives rise to electron-hole symmetry breaking interaction within the dynamic Hubbard model framework. We have used this framework to model the interaction of fermions with the energy states due to rearrangement of the core electrons in the presence of moving fermions. We have restricted our analysis to the interaction of two fermions with the local degrees of freedom. Within this model, two holes form an effective nearest neighbor attraction whereas two electrons repel. We have shown a clear crossover from a weak coupling of the holes to the local degrees of freedom to the strong coupling, where the on-site repulsion component of the model, U , enhances the nearest neighbor attraction, rather than hindering it. We have compared the dynamic Hubbard model to the original Hubbard model and the static Hubbard model, both of which are electron-hole symmetric. The observables we have calculated, the density-density correlation functions, the spectral function, and the optical conductivity, for these electron-hole symmetric models differ considerably from the hole representation of the dynamic Hubbard model. The density-density correlation functions exhibit well defined nearest neighbor peaks for the holes within the dynamic Hubbard model, whereas electron-hole symmetric ones show only repulsion of the two fermions. Low energy peak of the dynamical response functions, the spectral function and the optical conductivity, has shown monotonic dependence on the on-site repulsion, U , for the electron-hole symmetric models, indicating two compet-

ing interactions, on-site repulsion and fermion-pseudo-spin interaction. For the holes within the dynamic Hubbard model, a non-monotonic behavior has been observed for strong coupling, showing that the on-site repulsion can enhance fermion-pseudo-spin interaction.

For the coupled local degrees of freedom, the itinerant fermion is used to model a spin current interacting with a magnetic layer, modeled by the coupled local spin degrees of freedom. The spin current interacts with the coupled local spins through a Kondo-like interaction, whereas the magnetic layer is assumed to have Heisenberg-like interaction. We have looked at time dependent interaction of the spin current with the magnetic layer. We have simulated the interaction via a wave packet with spin up moving towards the local spins that all have spin down, and after the interaction, depending on the parameters, reflecting back, or transmitting forward. For numerical calculations, since standard approach would have been very time consuming, we have developed an approximation within Chebyshev series expansion, and performed the numerical calculations with this approximation. Depending on the relative values of two types of interaction, a non-linear behavior is observed. We first looked at the itinerant part and the local spin part separately. We identified indications for different regimes, but this analysis did not provide qualitative understanding for the origin of the behavior. Using basis states that properly group the states of both itinerant spin and the local spins, we have shown that both energy conserving interaction and energy transfer interaction exist for low spin-spin interaction, J_1 . In addition, for larger values of J_1 , we have shown that energy conservation does not allow the energy transfer state to exist for a long period of time. However, we have shown the existence of a region in the parameter space of wave packet-spin and spin-spin interaction where due to temporary transfer of energy, the Kondo-like spin-flip interaction is enhanced considerably. To explain this behavior, we have used plane wave approximation of the spin current, where the boundary conditions are set to have only relevant components to move towards the local spins, to analytically show that interaction with energy transfer is responsible for the existence of this non-equilibrium-bound-state even though at the beginning of the interaction or long after the interaction, this basis state is not present. The main focus of this analysis has been with two local spins in one dimension for simplicity and computational efficiency purposes. Longer spin systems have also been presented. For realistic systems, arguments for the validity of the results in higher dimensions and for the systems with larger local spin degree of freedom have been given. We believe that the physics described within this model will become more relevant and important with the improvements to the experimental techniques and the production of smaller magnetic structures interacting spin currents, both experimentally and commercially.

Bibliography

- [1] See, for example, *Lecture Notes on Electron Correlation and Magnetism*, Springer Series in Condensed Matter Physics Vol. **5**, P. Fazekas, World Scientific (1999).
- [2] J. Hubbard Proc. R. Soc. London, Ser. A **276**, 238 (1963)
- [3] E. Dagotto, Rev. Mod. Phys. **66**, 763 (1994), and references therein
- [4] A. Georges, G. Kotliar, W. Krauth, and M. J. Rozenberg Rev. Mod. Phys. **68**, 13 (1996)
- [5] M. Imada, A. Fujimori, and Y. Tokura Rev. Mod. Phys. **70**, 1039 (1998)
- [6] K. Alex Mller and J. Georg Bednorz. Science, **237**, 1133 (1987)
- [7] R. Micnas, J. Ranninger, and S. Robaszkiewicz Rev. Mod. Phys. **62**, 113 (1990)
- [8] L. Covaci and F. Marsiglio Phys. Rev. B **73**, 014503 (2006)
- [9] S. White, Phys Rev. Lett. **69**, 2863 (1992).
- [10] U.Schollwock, Rev. Mod. Phys. **77**, 259 (2005).
- [11] S. White, in CIFAR-PITP International Summer School on Numerical Methods for Correlated Systems in Condensed Matter (2008).
- [12] K. Bouadim, M. Enjalran, F. Hébert, G.G. Batrouni, and R.T. Scalettar, Phys. Rev. B **77**, 014516 (2008)
- [13] See, for example, P.A. Rikvold, G. Brown, S.J. Mitchell, and M.A. Novotny, in *Nanostructured Magnetic Materials and their Applications*, edited by D. Shi, B. Aktas, L. Pust, and F. Mikailov, Springer Lecture Notes in Physics, Vol. 593 (Springer, Berlin, 2002), p. 164. See also cond-mat/0110103.
- [14] M.R. Freeman and W.K. Hiebert, in *Spin Dynamics in Confined Magnetic Structures I*, edited by B. Hillebrands and K. Ounadjela (Springer, Berlin, 2002).

- [15] See, for example, T.L. Gilbert, IEEE Transactions on Magnetism **40**, 3343 (2004).
- [16] J.C. Slonczewski, J. Magn. Magn. **159**, L1 (1996); **195**, L261 (1999)
- [17] L. Berger, Phys. Rev. B **54**, 9353 (1996).
- [18] Y. Bazaliy, B. A. Jones, and S.-C. Zhang, Phys. Rev. B **57**, R3213 (1998).
- [19] W. Kim and F. Marsiglio, Phys. Rev. B **69** 212406 (2004).
- [20] A. Brataas, Gergely Zaránd, Yaroslav Tserkovnyak, and Gerrit E. W. Bauer, Phys. Rev. Lett. **91**, 166601 (2003).
- [21] W. Kim and F. Marsiglio, Can. J. Phys. **84**: 507 (2006).
- [22] See the many articles in J. Magnetism and Magnetic Materials **320**, pp. 1190-1311 (2008).
- [23] J.C.Sankey, Y.-T. Cui, J.Z. Sun, J.C. Slonczewski, R.A. Buhrman, and D.C. Ralph, Nat. Phys. **4**, 67 (2008).
- [24] T. Balashov, A.F. Takacs, M. Dane, A. Ernst, P. Bruno, and W. Wulfhekkel, Phys. Rev. B **78**, 174404 (2008).
- [25] C.F. Hirjibehedin, C.P. Lutz, and A.J. Heinrich, Science **312**, 1021 (2006).
- [26] W. Kim, L. Covaci, F. Doğan and F. Marsiglio, Europhys. Lett. **79**, 67004 (2007).
- [27] F. Doğan, W. Kim, C.M. Blois, and F. Marsiglio, Phys. Rev. B **77**, 195107 (2008).
- [28] F. Ciccarello, M. Paternostro, G. M. Palma, M. Zarcone, arXiv:0812.0755v1 [quant-ph]
- [29] K. Wilson, Rev. Mod. Phys **47**, 773 (1975).
- [30] I. Perschel, X. Wang, M. Kaulke and K. Hallberg (eds.) *Density Matrix Renormalization-A New Numerical Method in Physics*, Lecture Notes in Phys., vol. 528 (Springer, Berlin, 1999).
- [31] David Senechal, Andre-Marie Tremblay and Claude Bourbonnais (eds.), *Theoretical Methods for Strongly Correlated Electrons*, CRM Series in Mathematical Physics,(Springer, New York, 2003).
- [32] R. Feynman, *Statistical Mechanics: A Set of Lectures* (Benjamin, Reading, MA, 1972).

- [33] S. White, Phys Rev. B **48**, 10345 (1993).
- [34] The converged value of the observable is plotted as a function of inverse of the total states kept (m), and the value is extrapolated to $m \rightarrow \infty$.
- [35] J.E. Hirsch, Phys. Lett. A **134**, 451 (1989).
- [36] J.E. Hirsch, S. Tang, Phys. Rev. B **40**, 2179 (1989).
- [37] J.E. Hirsch, F. Marsiglio Phys. Rev. B **41**, 2049 (1990).
- [38] J.E. Hirsch, Phys. Rev. B **43**, 11400 (1991).
- [39] J.E. Hirsch, Phys. Rev. B **48**, 3327 (1993).
- [40] H.Q. Lin, J.E. Hirsch, Phys. Rev. B **52**, 16155 (1995).
- [41] J.E. Hirsch, Phys. Rev. B **47**, 5351 (1993).
- [42] J.E. Hirsch, Phys. Rev. Lett. **87**, 206402 (2001).
- [43] J.E. Hirsch, Phys. Rev. B **66**, 064507 (2002).
- [44] J.E. Hirsch, Phys. Rev. B **65**, 214510 (2002).
- [45] J.E. Hirsch, Phys. Rev. B **67**, 035103 (2003).
- [46] F. Marsiglio, R. Teshima, and J.E. Hirsch, Phys. Rev. B **68**, 224507 (2003).
- [47] Andreas Kemper, Andreas Schadschneider Phys. Rev. B **73**, 85113 (2006)
- [48] Andreas Kemper, Andreas Schadschneider Phys. Rev. B **68**, 235102 (2003)
- [49] A. Anfossi, C. Degli, E. Boschi and A. Montorsi, cond-mat/0901.4507
- [50] S. R. White Phys. Rev. B **72**, 180403(R) (2005).
- [51] K. Tanaka and F. Marsiglio Phys. Rev. B **62**, 5345 (2000)
- [52] W. Kim, L. Covaci, and F. Marsiglio, Phys. Rev. B **74**, 205120 (2006)
- [53] A. Weiße and H. Fehske: *Chebyshev Expansion Techniques*, Lect. Notes Phys. **739**, 545577 (2008)
- [54] Dumont, Jain, Bain, J. Chem. Phys., **106**, No. 14, 8 April 1997
- [55] W. Liang et al. Journal of Computational Physics **194** 575 (2004)
- [56] Reader is suggested to go through the derivation before using these formulas.

- [57] It is interesting, on the other hand, to note that for single local spin $\langle \sigma_z \rangle$ is never negative in this setup.
- [58] One should note that, we cannot make a one-to-one quantitative correspondence between the parameters shown here because we change the very basic notion of operators.
- [59] Pauncz, R. *The Construction of Spin Eigenfunctions, An Exercise Book*; Kluwer Academic/Plenum Publishers: New York.
- [60] V.J. Emery, Phys. Rev. Lett, **58**, 2794 (1987).
- [61] F. C. Zhang and T. M. Rice, Phys. Rev. B **37**, 3759 (1988).
- [62] A. Lanzara, P.V Bogdanov, X.J. Zhou, S.A Kellar, D.L. Feng, E.D. Lu, T. Yoshida, H. Eisaki, A. Fujimori, K. Kishio, J.-I. Shimoyama, T. Noda, S. Uchida, Z.Hussain and Z.-X. Shen, Nature **412**, 510 (2001).

Appendix A

Time Evolution Using Chebyshev Polynomials

Introduction

In order to analyze the time evolution of a system, one can perform one of two tasks:

- One can form a wavepacket, let it interact with eigenvalues/eigenvectors of the system through the equation: $\Psi(t) = \sum_n |n\rangle \langle n| \Psi(0) \rangle e^{iE_n t}$. This has been done extensively.
- One can expand the exponential matrix $e^{i\hat{H}t}$ in polynomials, and directly perform $\Psi(t) = e^{i\hat{H}t} |\Psi(0)\rangle$.

In this appendix, we examine a quick way of expanding this exponential in a way that uses very little memory and computation time.

Some of the introduction of the method given in Sec. 3.2 will be briefly repeated. In order for the expansion to work, one should find a portion of the exponential that is less than unity in magnitude. We accomplish this by introducing a factor E_{max} , an upper bound for the eigenvalue of the Hamiltonian.

We rewrite the equation as:

$$\Psi(t) = e^{iE_{max}t \frac{\hat{H}}{E_{max}}} |\Psi(0)\rangle \quad (\text{A-1})$$

From now on, we will only look at the exponential. Try and write it in a form that we can analyze further. The first step is to redefine $y = E_{max}t$, and $x = \frac{\hat{H}}{E_{max}}$.

$$e^{iE_{max}t \frac{\hat{H}}{E_{max}}} = e^{ixy} = \sum_{n=0}^{\infty} a_n(y) T_n(x) \quad (\text{A-2})$$

where: $T_n(x) = \cos(n \arccos(x))$, $T_0(x) = 1$, $T_1(x) = x$ and $T_n(x) = 2xT_{n-1}(x) - T_{n-2}(x)$. a_n can be found using the orthogonality of the trigonometric functions:

$$a_n(y) = \frac{2 - \delta_{n0}}{\pi} \int_{-1}^1 \frac{dx}{\sqrt{1-x^2}} T_n(x) \exp(ixy). \quad (\text{A-3})$$

It has been shown that this equation can be reduced to [53];

$$a_n(y) = (2 - \delta_{0n}) i^n J_n(y), \quad (\text{A-4})$$

where $J_n(y)$ is the n^{th} order Bessel polynomial. The recursion relation can also be written as:

$$\cos((n+m)x) = 2\cos(nx)\cos(mx) - \cos(|n-m|x) \quad (\text{A-5})$$

or

$$T_{n+m}(x) = 2T_n(x)T_m(x) - T_{|n-m|}(x). \quad (\text{A-6})$$

We will use this relationship, Eq. A-6, to find a computationally efficient way to use Chebyshev expansion to approximate time evolution of a wave packet. Since the arguments of T_n for any n is x , we can drop it from now on, also, y is common to all a_n . We are looking for a specific accuracy in the expansion, how we can get away with minimal calculation of the power of the Hamiltonian, because the minimal power of the Hamiltonian means minimal matrix-vector multiplication. We will divide a given summation;

$$\sum_{i=0}^{N \times N} a_i T_i \quad (\text{A-7})$$

into many summations of order N , given by

$$\sum_{i=0}^{N \times N} a_i T_i = \sum_{i=0}^N a_i T_i + \sum_{i=N+1}^{2N} a_i T_i + \sum_{i=2N+1}^{3N} a_i T_i + \sum_{i=3N+1}^{4N} a_i T_i + \dots + \sum_{i=(N-1)N+1}^{N \times N} a_i T_i \quad (\text{A-8})$$

In the next section, each of these summations is probed and a useful relationship is derived. We will try to have the largest index of T to be N in this case, rather than the $N \times N$ of equation A-8.

A.1 Derivation

We will call each summation on the right hand side of the Eq. A-8 a level and look at each level separately.

Zeroth level is

$$\sum_0^N a_i T_i. \quad (\text{A.1-0})$$

First level is

$$\sum_{N+1}^{2N} a_i T_i = \sum_1^N a_{N+i} T_{N+i} = \sum_1^N a_{N+i} (2T_N T_i - T_{N-i}) = \sum_1^N a_{N+i} (-T_{N-i} + 2T_N T_i). \quad (\text{A.1-1})$$

Second level is

$$\begin{aligned} \sum_{2N+1}^{3N} a_i T_i &= \sum_1^N a_{2N+i} T_{2N+i} = \sum_1^N a_{2N+i} (2T_N T_{N+i} - T_i) \\ &= \sum_1^N a_{2N+i} (2T_N (2T_N T_i - T_{N-i}) - T_i) \\ &= \sum_1^N a_{2N+i} (4T_N^2 T_i - 2T_N T_{N-i} - T_i) \\ &= \sum_1^N a_{2N+i} (-T_i - 2T_N T_{N-i} + 4T_N^2 T_i). \end{aligned} \quad (\text{A.1-2})$$

We will omit all coefficients and summations, since they follow the level, to keep track of coefficients, we will write them next to level label.

Third level is, with (a_{3N+i}) ,

$$\begin{aligned} T_{3N+i} &= 2T_{2N} T_{N+i} - T_{N-i} = 2(2T_N^2 - 1)(2T_N T_i - T_{N-i}) - T_{N-i} \\ &= 4T_N^2 - 2(2T_N T_i - T_{N-i}) - T_{N-i} \\ &= 8T_N^3 T_i - 4T_N^2 T_{N-i} - 4T_N T_i + 2T_{N-i} - T_{N-i} \\ &= T_{N-i} - 4T_N T_i - 4T_N^2 T_{N-i} + 8T_N^3 T_i. \end{aligned} \quad (\text{A.1-3})$$

Fourth level is, with (a_{4N+i}) ,

$$\begin{aligned} T_{4N+i} &= 2T_{2N} T_{2N+i} - T_i = 2(2T_N^2 - 1)(-T_i - 2T_N T_{N-i} + 4T_N^2 T_i) - T_i \\ &= -4T_N^2 T_i - 8T_N^3 T_{N-i} + 16T_N^4 T_i + 2T_i + 4T_N T_{N-i} - 8T_N^2 T_i - T_i \\ &= T_i + 4T_N T_{N-i} - 12T_N^2 T_i - 8T_N^3 T_{N-i} + 16T_N^4 T_i. \end{aligned} \quad (\text{A.1-4})$$

Fifth level is, with (a_{5N+i}) ,

$$\begin{aligned} T_{5N+i} &= 2T_{3N} T_{2N+i} - T_{N-i} \\ &= 2(2T_{2N} T_N - T_N)(-T_i - 2T_N T_{N-i} + 4T_N^2 T_i) - T_{N-i} \end{aligned}$$

$$\begin{aligned}
 &= 2(2(2T_N T_N - 1)T_N - T_N)(-T_i - 2T_N T_{N-i} + 4T_N^2 T_i) - T_{N-i} \\
 &= 2(4T_N^3 - 3T_N)(-T_i - 2T_N T_{N-i} + 4T_N^2 T_i) - T_{N-i} \\
 &= 2(-4T_N^3 T_i - 8T_N^4 T_{N-i} + 16T_N^5 T_i + 3T_N T_i + 6T_N^2 T_{N-i} - 12T_N^3 T_i) - T_{N-i} \\
 &= -T_{N-i} + 6T_N T_i + 12T_N^2 T_{N-i} - 32T_N^3 T_i - 16T_N^4 T_{N-i} + 32T_N^5 T_i. \quad (\text{A.1-5})
 \end{aligned}$$

Sixth level is, with (a_{6N+i}) ,

$$\begin{aligned}
 T_{6N+i} &= 2T_{3N} T_{3N+i} - T_i = 2(2T_{2N} T_N - T_N)(T_{N-i} - 4T_N T_i - 4T_N^2 T_{N-i} + 8T_N^3 T_i) - T_i \\
 &= 2(2(2T_N T_N - 1)T_N - T_N)(T_{N-i} - 4T_N T_i - 4T_N^2 T_{N-i} + 8T_N^3 T_i) - T_i \\
 &= 2(4T_N^3 - 3T_N)(T_{N-i} - 4T_N T_i - 4T_N^2 T_{N-i} + 8T_N^3 T_i) - T_i \\
 &= 2(4T_N^3 T_{N-i} - 16T_N^4 T_i - 16T_N^5 T_{N-i} + 32T_N^6 T_i - 3T_N T_{N-i} \\
 &\quad + 12T_N^2 T_i + 12T_N^3 T_{N-i} - 24T_N^4 T_i) - T_i \\
 &= 8T_N^3 T_{N-i} - 32T_N^4 T_i - 32T_N^5 T_{N-i} + 64T_N^6 T_i - 6T_N T_{N-i} + 24T_N^2 T_i \\
 &\quad + 24T_N^3 T_{N-i} - 48T_N^4 T_i - T_i \\
 &= -T_i - 6T_N T_{N-i} + 24T_N^2 T_i + 32T_N^3 T_{N-i} - 80T_N^4 T_i \\
 &\quad - 32T_N^5 T_{N-i} + 64T_N^6 T_i. \quad (\text{A.1-6})
 \end{aligned}$$

Seventh level is, with (a_{7N+i}) ,

$$\begin{aligned}
 T_{7N+i} &= 2T_{4N} T_{3N+i} - T_{N-i} \\
 &= 2(2T_{2N} T_{2N} - 1)(T_{N-i} - 4T_N T_i - 4T_N^2 T_{N-i} + 8T_N^3 T_i) - T_{N-i} \\
 &= 2(2(2T_N T_N - 1)(2T_N T_N - 1) - 1)(T_{N-i} - 4T_N T_i - 4T_N^2 T_{N-i} + 8T_N^3 T_i) - T_{N-i} \\
 &= 2(2(4T_N^4 - 4T_N^2 + 1) - 1)(T_{N-i} - 4T_N T_i - 4T_N^2 T_{N-i} + 8T_N^3 T_i) - T_{N-i} \\
 &= 2(8T_N^4 - 8T_N^2 + 1)(T_{N-i} - 4T_N T_i - 4T_N^2 T_{N-i} + 8T_N^3 T_i) - T_{N-i} \\
 &= 2(8T_N^4 T_{N-i} - 32T_N^5 T_i - 32T_N^6 T_{N-i} + 64T_N^7 T_i - 8T_N^2 T_{N-i} + 32T_N^3 T_i \\
 &\quad + 32T_N^4 T_{N-i} - 64T_N^5 T_i + T_{N-i} - 4T_N T_i - 4T_N^2 T_{N-i} + 8T_N^3 T_i) - T_{N-i} \\
 &= 2(40T_N^4 T_{N-i} - 96T_N^5 T_i - 32T_N^6 T_{N-i} + 64T_N^7 T_i - 12T_N^2 T_{N-i} \\
 &\quad + 40T_N^3 T_i + T_{N-i} - 4T_N T_i) - T_{N-i} \\
 &= 80T_N^4 T_{N-i} - 192T_N^5 T_i - 64T_N^6 T_{N-i} + 128T_N^7 T_i - 24T_N^2 T_{N-i} \\
 &\quad + 80T_N^3 T_i + T_{N-i} - 8T_N T_i \\
 &= T_{N-i} - 8T_N T_i - 24T_N^2 T_{N-i} + 80T_N^3 T_i + 80T_N^4 T_{N-i} - 192T_N^5 T_i \\
 &\quad - 64T_N^6 T_{N-i} + 128T_N^7 T_i. \quad (\text{A.1-7})
 \end{aligned}$$

Eighth level is, with (a_{8N+i}) .

$$\begin{aligned}
 T_{8N+i} &= 2T_{4N}T_{4N+i} - T_i \\
 &= 2(2T_{2N}T_{2N} - 1)(T_i + 4T_N T_{N-i} - 12T_N^2 T_i - 8T_N^3 T_{N-i} + 16T_N^4 T_i) - T_i \\
 &= 2(8T_N^4 - 8T_N^2 + 1)(T_i + 4T_N T_{N-i} - 12T_N^2 T_i - 8T_N^3 T_{N-i} + 16T_N^4 T_i) - T_i \\
 &= 2(8T_N^4 T_i + 32T_N^5 T_{N-i} - 96T_N^6 T_i - 64T_N^7 T_{N-i} + 128T_N^8 T_i - 8T_N^2 T_i \\
 &\quad - 32T_N^3 T_{N-i} + 96T_N^4 T_i + 64T_N^5 T_{N-i} - 128T_N^6 T_i + T_i + 4T_N T_{N-i} \\
 &\quad - 12T_N^2 T_i - 8T_N^3 T_{N-i} + 16T_N^4 T_i) - T_i \\
 &= 2(120T_N^4 T_i + 96T_N^5 T_{N-i} - 224T_N^6 T_i - 64T_N^7 T_{N-i} + 128T_N^8 T_i - 20T_N^2 T_i \\
 &\quad - 40T_N^3 T_{N-i} + T_i + 4T_N T_{N-i}) - T_i \\
 &= T_i + 8T_N T_{N-i} - 40T_N^2 T_i - 80T_N^3 T_{N-i} + 240T_N^4 T_i + 192T_N^5 T_{N-i} \\
 &\quad - 448T_N^6 T_i - 128T_N^7 T_{N-i} + 256T_N^8 T_i.
 \end{aligned} \tag{A.1-8}$$

With these results, we can form a table of coefficients. Columns run over power of T_N (order), whereas rows run over the level (or the coefficient a).

1	0	0	0	0	0	0	0	0
-1x	2	0	0	0	0	0	0	0
-1	-2x	4	0	0	0	0	0	0
1x	-4	-4x	8	0	0	0	0	0
1	4x	-12	-8x	16	0	0	0	0
-1x	6	12x	-32	-16x	32	0	0	0
-1	-6x	24	32x	-80	-32x	64	0	0
1x	-8	-24x	80	80x	-192	-64x	128	0
1	8x	-40	-80x	240	192x	-448	-128x	256

Please note that $a_i T_{N-i} = a_{N-i} T_i$.

Notes:

- The largest order in each level is positive.
- The largest order in each level has i rather than $N - i$.
- From largest order, there are 2 negatives and 2 positives in sequence.

- From lowest level, i is changed to $N - i$ in each step then back to i in the next step.
- x represents the change of i to $N - i$. It is similar to definition of a . The change in index of T can be changed to index of coefficients a .
- **This is the real trick:** The increase in levels happens for every second term. Increase is by twice the value of one lower order.

With these notes, we define:

$$A(i, j) = \begin{cases} A(i - 1, j) + 2 * A(i - 1, j - 1) & \text{mod}(i - j, 2) = 0 \\ -A(i - 1, j) & \text{mod}(i - j, 2) = 1 \\ 0 & i < j. \end{cases} \quad (\text{A.1-9})$$

with $A(0, 0) = 1$. With this definition of $A(i, j)$, the equation can be written as:

$$\sum_0^{NxN} a_i T_i = \sum_0^N b_i^0 T_i + T_N (\sum_1^N b_i^1 T_i + \dots + T_N (\sum_1^N b_i^k T_i + \dots + T_N \sum_1^N b_i^N T_i) \dots) \quad (\text{A.1-10})$$

where

$$b_i^k = \sum_{j=0}^{N-k} (\text{mod}(j, 2) * A(j + k, k) a_{((j+k+1)*N-i)} + \text{mod}(j + 1, 2) * A(j + k, k) a_{((j+k)*N+i)}) \quad (\text{A.1-11})$$

Appendix B

Plane Wave Derivations

We want to look at a wave packet with spin-1/2 pointing up and 2 spins (each spin is spin $\frac{1}{2}$ pointing down) with the Hamiltonian;

$$H = -\frac{\hbar^2}{2m} \frac{d^2}{dx^2} - 2J_0[\hat{\sigma} \cdot \hat{S}_1 \delta(x) + \hat{\sigma} \cdot \hat{S}_2 \delta(x-a)] - 2J_1 \hat{S}_1 \cdot \hat{S}_2 \quad (\text{B-1})$$

The state we are interested in is $(S_z)_{tot} = -\frac{1}{2}$ so the states are $|\uparrow\downarrow\downarrow\rangle$, $|\downarrow\uparrow\downarrow\rangle$, $|\downarrow\downarrow\uparrow\rangle$, resulting in $|\psi\rangle = \phi_1(x)|\uparrow\downarrow\downarrow\rangle + \phi_2(x)|\downarrow\uparrow\downarrow\rangle + \phi_3|\downarrow\downarrow\uparrow\rangle$.
Operations;

$$\hat{\sigma} \cdot \hat{S}_1 |\uparrow\downarrow\downarrow\rangle = [\sigma_z S_{1z} + \frac{1}{2}(\sigma_+ S_{1-} + \sigma_- S_{1+})] |\uparrow\downarrow\downarrow\rangle = -\frac{\hbar^2}{4} |\uparrow\downarrow\downarrow\rangle + \frac{\hbar^2}{2} |\downarrow\uparrow\downarrow\rangle \quad (\text{B-2})$$

$$\hat{\sigma} \cdot \hat{S}_1 |\downarrow\uparrow\downarrow\rangle = -\frac{\hbar^2}{4} |\downarrow\uparrow\downarrow\rangle + \frac{\hbar^2}{2} |\uparrow\downarrow\downarrow\rangle \quad (\text{B-3})$$

$$\hat{\sigma} \cdot \hat{S}_1 |\downarrow\downarrow\uparrow\rangle = \frac{\hbar^2}{4} |\downarrow\downarrow\uparrow\rangle \quad (\text{B-4})$$

$$\hat{\sigma} \cdot \hat{S}_2 |\uparrow\downarrow\downarrow\rangle = [\sigma_z S_{2z} + \frac{1}{2}(\sigma_+ S_{2-} + \sigma_- S_{2+})] |\uparrow\downarrow\downarrow\rangle = -\frac{\hbar^2}{4} |\uparrow\downarrow\downarrow\rangle + \frac{\hbar^2}{2} |\downarrow\downarrow\uparrow\rangle \quad (\text{B-5})$$

$$\hat{\sigma} \cdot \hat{S}_2 |\downarrow\uparrow\downarrow\rangle = \frac{\hbar^2}{4} |\downarrow\uparrow\downarrow\rangle \quad (\text{B-6})$$

$$\hat{\sigma} \cdot \hat{S}_2 |\downarrow\downarrow\uparrow\rangle = -\frac{\hbar^2}{4} |\downarrow\downarrow\uparrow\rangle + \frac{\hbar^2}{2} |\uparrow\downarrow\downarrow\rangle \quad (\text{B-7})$$

$$\hat{S}_1 \cdot \hat{S}_2 = \left[\hat{S}_{1z} \hat{S}_{2z} + \frac{1}{2}(\hat{S}_{1+} \hat{S}_{2-} + \hat{S}_{1-} \hat{S}_{2+}) \right] \quad (\text{B-8})$$

$$\hat{S}_1 \cdot \hat{S}_2 |\uparrow\downarrow\downarrow\rangle = \frac{\hbar^2}{4} |\uparrow\downarrow\downarrow\rangle \quad (\text{B-9})$$

$$|\downarrow\uparrow\downarrow\rangle = -\frac{\hbar^2}{4}|\downarrow\uparrow\downarrow\rangle + \frac{\hbar^2}{2}|\downarrow\downarrow\uparrow\rangle \quad (\text{B-10})$$

$$|\downarrow\downarrow\uparrow\rangle = -\frac{\hbar^2}{4}|\downarrow\downarrow\uparrow\rangle + \frac{\hbar^2}{2}|\downarrow\uparrow\downarrow\rangle \quad (\text{B-11})$$

$H|\Psi\rangle = E|\Psi\rangle$ becomes

$$\begin{aligned} & -\frac{\hbar^2}{2m}\frac{d^2}{dx^2}(\phi_1|\uparrow\downarrow\downarrow\rangle + \phi_2|\downarrow\uparrow\downarrow\rangle + \phi_3|\downarrow\downarrow\uparrow\rangle) - 2J_0\delta(x)\frac{\hbar^2}{4}(-\phi_1|\uparrow\downarrow\downarrow\rangle + \phi_12|\downarrow\uparrow\downarrow\rangle \\ & - \phi_2|\downarrow\uparrow\downarrow\rangle + 2\phi_2|\uparrow\downarrow\downarrow\rangle + \phi_3|\downarrow\downarrow\uparrow\rangle) - 2J_0\delta(x-a)\frac{\hbar^2}{4}(-\phi_1|\uparrow\downarrow\downarrow\rangle + 2\phi_1|\downarrow\downarrow\uparrow\rangle \\ & + \phi_2|\downarrow\uparrow\downarrow\rangle - \phi_3|\downarrow\downarrow\uparrow\rangle + 2\phi_3|\uparrow\downarrow\downarrow\rangle) \\ & - 2J_1\frac{\hbar^2}{4}(\phi_1|\uparrow\downarrow\downarrow\rangle - \phi_2|\downarrow\uparrow\downarrow\rangle + 2\phi_2|\downarrow\downarrow\uparrow\rangle - \phi_3|\downarrow\downarrow\uparrow\rangle + 2\phi_3|\downarrow\uparrow\downarrow\rangle) \\ = & E(\phi_1|\uparrow\downarrow\downarrow\rangle + \phi_2|\downarrow\uparrow\downarrow\rangle + \phi_3|\downarrow\downarrow\uparrow\rangle) \end{aligned}$$

Separating out each component;

$|\uparrow\downarrow\downarrow\rangle$

$$-\frac{\hbar^2}{2m}\frac{d^2\phi_1}{dx^2} - 2J_0\delta(x)\frac{\hbar^2}{4}(-\phi_1 + 2\phi_2) - 2J_0\delta(x-a)\frac{\hbar^2}{4}(-\phi_1 + 2\phi_3) - 2J_1\frac{\hbar^2}{4}(\phi_1) = E\phi_1 \quad (\text{B-12})$$

$|\downarrow\uparrow\downarrow\rangle$

$$-\frac{\hbar^2}{2m}\frac{d^2\phi_2}{dx^2} - 2J_0\delta(x)\frac{\hbar^2}{4}(2\phi_1 - \phi_2) - 2J_0\delta(x-a)\frac{\hbar^2}{4}(\phi_2) - 2J_1\frac{\hbar^2}{4}(-\phi_2 + 2\phi_3) = E\phi_2 \quad (\text{B-13})$$

$|\downarrow\downarrow\uparrow\rangle$

$$-\frac{\hbar^2}{2m}\frac{d^2\phi_3}{dx^2} - 2J_0\delta(x)\frac{\hbar^2}{4}(\phi_3) - 2J_0\delta(x-a)\frac{\hbar^2}{4}(2\phi_1 - \phi_3) - 2J_1\frac{\hbar^2}{4}(2\phi_2 - \phi_3) = E\phi_3 \quad (\text{B-14})$$

The proper basis states are:

$$|h\rangle = \frac{1}{\sqrt{3}}(|\downarrow\downarrow\uparrow\rangle + |\downarrow\uparrow\downarrow\rangle + |\uparrow\downarrow\downarrow\rangle) \quad (\text{B-15})$$

$$|f\rangle = \frac{1}{\sqrt{6}}(|\downarrow\downarrow\uparrow\rangle + |\downarrow\uparrow\downarrow\rangle - 2|\uparrow\downarrow\downarrow\rangle) \quad (\text{B-16})$$

$$|g\rangle = \frac{1}{\sqrt{2}}(|\downarrow\downarrow\uparrow\rangle - |\downarrow\uparrow\downarrow\rangle) \quad (\text{B-17})$$

We rewrite differential equations in these basis states;

for h;

$$\begin{aligned} & -\frac{\hbar^2}{2m}\frac{d^2}{dx^2}(\phi_1 + \phi_2 + \phi_3) - 2J_0\delta(x)\frac{\hbar^2}{4}(\phi_1 + \phi_2 + \phi_3) - 2J_0\delta(x-a)\frac{\hbar^2}{4}(\phi_1 + \phi_2 + \phi_3) - \\ & 2J_1\frac{\hbar^2}{4}(\phi_1 + \phi_2 + \phi_3) = E(\phi_1 + \phi_2 + \phi_3), \\ & -\frac{\hbar^2}{2m}\frac{d^2h(x)}{dx^2} - 2J_0\delta(x)\frac{\hbar^2}{4}h(x) - 2J_0\delta(x-a)\frac{\hbar^2}{4}h(x) = (E + 2J_1\frac{\hbar^2}{4})h(x). \end{aligned}$$

For f;

$$-\frac{\hbar^2}{2m}\frac{d^2}{dx^2}(-2\phi_1 + \phi_2 + \phi_3) - 2J_0\delta(x)\frac{\hbar^2}{4}(2\phi_1 - 4\phi_2 + 2\phi_1 - \phi_2 + \phi_3) - 2J_0\delta(x-a)\frac{\hbar^2}{4}(2\phi_1 -$$

$$\begin{aligned}
4\phi_3 + \phi_2 + 2\phi_1 - \phi_3) - 2J_1 \frac{\hbar^2}{4} (-2\phi_1 - \phi_2 + 2\phi_3 + 2\phi_2 - \phi_3) &= E(-2\phi_1 + \phi_2 + \phi_3) \\
- \frac{\hbar^2}{2m} \frac{d^2}{dx^2} (\sqrt{6}f) - 2J_0 \delta(x) \frac{\hbar^2}{4} (-2(-2\phi_1 + \phi_2 + \phi_3) + 3(\phi_3 - \phi_2)) - 2J_0 \delta(x-a) \frac{\hbar^2}{4} (-2(-2\phi_1 + \\
\phi_2 + \phi_3) - 3(\phi_3 - \phi_2)) - 2J_1 \frac{\hbar^2}{4} (1(-2\phi_1 + \phi_2 + 2\phi_3) + 0(\phi_3 - \phi_2)) &= E\sqrt{6}f \\
- \frac{\hbar^2}{2m} \frac{d^2}{dx^2} (\sqrt{6}f) - 2J_0 \delta(x) \frac{\hbar^2}{4} (-2\sqrt{6}f + 3\sqrt{2}g) - 2J_0 \delta(x-a) \frac{\hbar^2}{4} (-2\sqrt{6}f - 3\sqrt{2}g) - \\
2J_1 \frac{\hbar^2}{4} (\sqrt{6}f) &= E\sqrt{6}f \\
- \frac{\hbar^2}{2m} \frac{d^2}{dx^2} f - 2J_0 \delta(x) \frac{\hbar^2}{4} (-2f + \sqrt{3}g) - 2J_0 \delta(x-a) \frac{\hbar^2}{4} (-2f - \sqrt{3}g) &= (E + 2J_1 \frac{\hbar^2}{4})f
\end{aligned}$$

For g;

$$\begin{aligned}
- \frac{\hbar^2}{2m} \frac{d^2}{dx^2} (\phi_3 - \phi_2) - 2J_0 \delta(x) \frac{\hbar^2}{4} (\phi_3 - 2\phi_1 + \phi_2) - 2J_0 \delta(x-a) \frac{\hbar^2}{4} (2\phi_1 - \phi_3 - \phi_2) - \\
2J_1 \frac{\hbar^2}{4} (2\phi_2 - \phi_3 + \phi_2 - 2\phi_3) &= E(\phi_3 - \phi_2) \\
- \frac{\hbar^2}{2m} \frac{d^2}{dx^2} \sqrt{2}g - 2J_0 \delta(x) \frac{\hbar^2}{4} (\sqrt{6}f) - 2J_0 \delta(x-a) \frac{\hbar^2}{4} (-\sqrt{6}f) - 2J_1 \frac{\hbar^2}{4} (-3\sqrt{2}g) &= E\sqrt{2}g \\
- \frac{\hbar^2}{2m} \frac{d^2}{dx^2} g - 2J_0 \delta(x) \frac{\hbar^2}{4} \sqrt{3}f - 2J_0 \delta(x-a) \frac{\hbar^2}{4} (-\sqrt{3}f) &= (E - 2J_1 \frac{\hbar^2}{4})g
\end{aligned}$$

Solving for h;

$$- \frac{\hbar^2}{2m} \frac{d^2 h}{dx^2} - 2J_0 \frac{\hbar^2}{4} (\delta(x) + \delta(x-a)) h = \left(E + 2J_1 \frac{\hbar^2}{4} \right) h \quad (\text{B-18})$$

We redefine the parameters for shorthand notation to be $E \rightarrow \frac{2E}{\hbar^2}$, $J_0 \rightarrow -J_0 m$ and $k = \sqrt{m(E + J_1)}$.

$$- \frac{d^2 h}{dx^2} + J_0 (\delta(x) + \delta(x-a)) h = k^2 h \quad (\text{B-19})$$

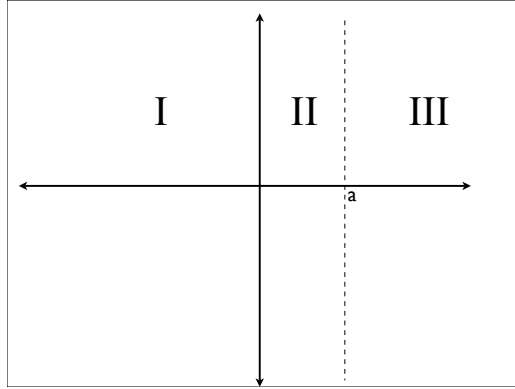


Figure B.1: Three regions for which the coefficients are defined.

$$h_I = Ae^{ikx} + Be^{-ikx} \quad (\text{B-20})$$

$$h_{II} = Ce^{ikx} + De^{-ikx} \quad (\text{B-21})$$

$$h_{III} = Ee^{ikx} \quad (\text{B-22})$$

Boundary conditions;

$$h_I(0) = h_{II}(0) \Rightarrow A + B = C + D \quad (\text{B-23})$$

$$h_{II}(a) = h_{III}(a) \Rightarrow Ce^{ika} + De^{-ika} = Ee^{ika} \Rightarrow E = C + De^{-2ika} \quad (\text{B-24})$$

$$\begin{aligned} \frac{dh_{III}}{dx}(a) - \frac{dh_{II}}{dx}(a) &= -J_0 h(a) \Rightarrow \\ ikEe^{ika} - ik(Ce^{ika} - De^{-ika}) &= -J_0(Ee^{ika}) \end{aligned} \quad (\text{B-25})$$

$$\begin{aligned} \frac{dh_{II}}{dx}(0) - \frac{dh_I}{dx}(0) &= -J_0 h(0) \Rightarrow \\ ik(A - B) - ik(C - D) &= -J_0(A - B) \end{aligned} \quad (\text{B-26})$$

$$e^{ika} ikE - ik(Ce^{ika} - De^{-ika}) = -J_0(Ee^{ika}) \quad (\text{B-27})$$

$$Ce^{ika} - De^{-ika} = \left(1 + \frac{J_0}{ik}\right) e^{ika} (C + De^{-2ika}) \quad (\text{B-28})$$

$$Ce^{ika} - De^{-ika} = \left(1 + \frac{J_0}{ik}\right) (Ce^{ika} + De^{-ika}) \quad (\text{B-29})$$

$$Ce^{ika} \left(1 - 1 - \frac{J_0}{ik}\right) = \left(1 + 1 + \frac{J_0}{ik}\right) e^{-ika} D \quad (\text{B-30})$$

$$C = \left(-\frac{2ik}{J_0} - 1\right) e^{-2ika} D \quad (\text{B-31})$$

$$(ik)(A - B) - ik(C - D) = -J_0(A - B) \quad (\text{B-32})$$

$$\begin{aligned} \left(1 + \frac{J_0}{ik}\right) (A - B) = C - D &= \left(\frac{-2ik}{J_0} - 1\right) e^{-ika} D - D = \\ D \left[\left(\frac{-2ik}{J_0} - 1\right) e^{-2ika} - 1\right] &= \frac{D}{J_0} [(-2ik - J_0) e^{-2ika} - J_0] \end{aligned} \quad (\text{B-33})$$

$$\begin{aligned} (A + B) = C + D &= \left(\frac{-2ik}{J_0} - 1\right) e^{-2ika} D + D = \\ D \left[\left(\frac{-2ik}{J_0} - 1\right) e^{-2ika} + 1\right] &= \frac{D}{J_0} [(-2ik - J_0) e^{-2ika} + J_0] \end{aligned} \quad (\text{B-34})$$

$$\frac{A - B}{A + B} = \left(\frac{ik}{ik + J_0} \right) \left(\frac{(2ik + J_0)e^{-2ika} + J_0}{(2ik + J_0)e^{-2ika} - J_0} \right) \quad (\text{B-35})$$

$$\frac{A - B}{A + B} = x \Rightarrow A - B = xA + xB \Rightarrow A - xA = B + xB \Rightarrow B = \frac{1 - x}{1 + x} A \quad (\text{B-36})$$

$$B = \frac{\frac{ik + J_0}{ik} - \frac{(2ik + J_0)e^{-2ika} + J_0}{(2ik + J_0)e^{-2ika} - J_0}}{\frac{ik + J_0}{ik} + \frac{(2ik + J_0)e^{-2ika} + J_0}{(2ik + J_0)e^{-2ika} - J_0}} A \quad (\text{B-37})$$

$$B = \frac{(ik + J_0)((2ik + J_0)e^{-2ika} - J_0) - ((2ik + J_0)e^{-2ika} + J_0)ik}{(ik + J_0)((2ik + J_0)e^{-2ika} - J_0) + ((2ik + J_0)e^{-2ika} + J_0)ik} A \quad (\text{B-38})$$

$$B = \frac{-2J_0ik + J_0((2ik + J_0)e^{-2ika} - J_0)}{2ik(2ik + J_0)e^{-2ika} + J_0((2ik + J_0)e^{-2ika} - J_0)} A \quad (\text{B-39})$$

$$B = \frac{2J_0ik(e^{-2ika} - 1) + J_0^2(e^{-2ika} - 1)}{e^{-2ika}(4ikJ_0 + (2ik)^2 + J_0^2) - J_0^2} A = \frac{(e^{-2ika} - 1)(2J_0ik + J_0^2)}{e^{-2ika}(2ik + J_0)^2 - J_0^2} A \quad (\text{B-40})$$

$$A + B = \frac{D}{J_0} ((-2ik - J_0)e^{-2ika} + J_0) \quad (\text{B-41})$$

$$A + \frac{(e^{-2ika} - 1)(2J_0ik + J_0^2)}{e^{-2ika}(2ik + J_0)^2 - J_0^2} A = \frac{D}{J_0} ((-2ik - J_0)e^{-2ika} + J_0) \quad (\text{B-42})$$

$$A \frac{e^{-2ika}(2ik + J_0)^2 - J_0^2 + (e^{-2ika} - 1)(2J_0ik + J_0^2)}{e^{-2ika}(2ik + J_0)^2 - J_0^2} = \frac{D}{J_0} ((-2ik - J_0)e^{-2ika} + J_0) \quad (\text{B-43})$$

$$A \frac{((2ik + J_0)(e^{-2ika}(2ik + J_0) + (e^{-2ika} - 1)J_0) - J_0^2)J_0}{((-2ik - J_0)e^{-2ika} + J_0)(e^{-2ika}(2ik + J_0)^2 - J_0^2)} = D \quad (\text{B-44})$$

$$E = C + De^{-2ika} \quad (\text{B-45})$$

$$E = \left(-\frac{2ik}{J_0} - 1 \right) e^{-2ika} D + De^{-2ika} \quad (\text{B-45})$$

$$E = \left(-\frac{2ik}{J_0} \right) e^{-2ika} D \quad (\text{B-46})$$

$$(\text{B-47})$$

$$E = \left(-\frac{2ik}{J_0} \right) \frac{((2ik + J_0)(e^{-2ika}(2ik + J_0) + (e^{-2ika} - 1)J_0) - J_0^2)J_0}{((-2ik - J_0)e^{-2ika} + J_0)(e^{-2ika}(2ik + J_0)^2 - J_0^2)} e^{-2ika} A \quad (\text{B-48})$$

We need to solve the other two equations together as they are coupled.

$$-\frac{\hbar^2}{2m} \frac{d^2 g(x)}{dx^2} - \sqrt{3}J_0 \frac{\hbar^2}{2} [\delta(x) - \delta(x-a)]f(x) = (E - \frac{3}{2}J_1\hbar^2)g(x) \quad (\text{B-49})$$

$$-\frac{\hbar^2}{2m} \frac{d^2 f(x)}{dx^2} + J_0 \frac{\hbar^2}{2} [\delta(x)(2f(x) - \sqrt{3}g(x)) + \delta(x-a)(2f(x) + \sqrt{3}g(x))] = (E + J_1 \frac{\hbar^2}{2})f(x) \quad (\text{B-50})$$

Depending on the sign of right hand side of the equation for g , the general form of $g(x)$ will change. We will first solve one case and generalize to all values of E .

B.1 Case for $E > 3J_1$

The general form of the solutions are, with the regions defined in Fig. B,

$$f(x) = \begin{cases} f_I(x) = Xe^{ipx} + Ye^{-ipx} \\ f_{II}(x) = Ze^{ipx} + Te^{-ipx} \\ f_{III}(x) = Ve^{ipx} \end{cases} \quad (\text{B-51})$$

$$g(x) = \begin{cases} g_I(x) = Ee^{ikx} + Ae^{-ikx} \\ g_{II}(x) = Be^{ikx} + Ce^{-ikx} \\ g_{III}(x) = De^{ikx} \end{cases} \quad (\text{B-52})$$

with

$$E \rightarrow \frac{2E}{\hbar^2} \quad J_0 \rightarrow mJ_0 \quad k = \sqrt{m(E - 3J_1)} \quad p = \sqrt{m(E + J_1)}. \quad (\text{B-53})$$

The differential equation becomes:

$$-\frac{d^2 f(x)}{dx^2} + J_0[\delta(x)(2f(x) - \sqrt{3}g(x)) + \delta(x-a)(2f(x) + \sqrt{3}g(x))] = p^2 f(x) \quad (\text{B-54})$$

$$-\frac{d^2 g(x)}{dx^2} - \sqrt{3}J_0[\delta(x) - \delta(x-a)]f(x) = k^2 g(x). \quad (\text{B-55})$$

The boundary conditions are:

$$g_I(0) = g_{II}(0)/g_{III}(a) = g_{II}(a)/\frac{dg_{II}(0)}{dx} - \frac{dg_I(0)}{dx}$$

$$= \sqrt{3}J_0f(0)/\frac{dg_{III}(a)}{dx} - \frac{dg_{II}(a)}{dx} = -\sqrt{3}J_0f(a) \quad (\text{B-56})$$

We now solve this set of equations with the definitions of $g(x)$ and $f(x)$,

$$\begin{aligned} f_I(0) &= f_{II}(0)/f_{III}(a) = f_{II}(a)/\frac{df_{II}(0)}{dx} - \frac{df_I(0)}{dx} = -J_0(2f(0) - \sqrt{3}g(0))/ \\ &\frac{df_{III}(a)}{dx} - \frac{df_{II}(a)}{dx} = -J_0(2f(a) + \sqrt{3}g(a)) \end{aligned} \quad (\text{B-57})$$

$$E = 0 \quad (\text{B-58})$$

$$E + A = B + C \quad (\text{B-59})$$

$$Be^{ika} + Ce^{-ika} = De^{ika} \quad (\text{B-60})$$

$$ik(B - C - (E - A)) = \sqrt{3}J_0(X + Y) \quad (\text{B-61})$$

$$ik(De^{ika} - (Be^{ika} - Ce^{-ika})) = -\sqrt{3}J_0Ve^{ipa} \quad (\text{B-62})$$

$$X + Y = Z + T \quad (\text{B-63})$$

$$Ve^{ipa} = Ze^{ipa} + Te^{-ipa} \quad (\text{B-64})$$

$$ip(Z - T) - ip(X - Y) = -J_0(2(X + Y) - \sqrt{3}(E + A)) \quad (\text{B-65})$$

$$ip(Ve^{ipa} - (Ze^{ipa} - Te^{-ipa})) = -J_0(2Ve^{ipa} + \sqrt{3}De^{ika}) \quad (\text{B-66})$$

$$A = B + C \quad (\text{B-67})$$

$$ik(B - C + A) = \sqrt{3}J_0(Z + T) \Rightarrow ik(2c) = \sqrt{3}J_0(Z + T) \quad (\text{B-68})$$

$$ik(Be^{ika} + Ce^{-ika} - (Be^{ika} - Ce^{-ika})) = -\sqrt{3}J_0(Ze^{ipa} + Te^{-ipa}) \quad (\text{B-69})$$

$$X + Y = Z + T \quad (\text{B-70})$$

$$ip((Z - T) - (X - Y)) = -J_0(2(X + Y) - \sqrt{3}(E + A)) \quad (\text{B-71})$$

$$ip(Ze^{ipa} + Te^{-ipa} - (Ze^{ipa} - Te^{-ipa})) = -J_0(2(Ze^{ipa} + Te^{-ipa}) + \sqrt{3}(Be^{ika} + Ce^{-ika})) \quad (\text{B-72})$$

$$ik(2B) = \sqrt{3}J_0(Z + T) \Rightarrow B = \frac{\sqrt{3}J_0}{2} \frac{1}{ik} (Z + T) \quad (\text{B-73})$$

$$ik(2Ce^{-ika}) = -\sqrt{3}J_0(Ze^{ipa} + Te^{-ipa}) \quad (\text{B-74})$$

$$X + Y = Z + T \quad (\text{B-75})$$

$$ip(Z - T - X + Y) = -J_0(2(X + Y) - \sqrt{3}(B + C)) \quad (\text{B-76})$$

$$ip(2Te^{-ipa}) = -J_0(2(Ze^{ipa} + Te^{-ipa}) + \sqrt{3}(Be^{ika} + Ce^{-ika})) \quad (\text{B-77})$$

$$ik(2Ce^{-ika}) = -\sqrt{3}J_0(Ze^{ipa} + Te^{-ipa}) \quad (\text{B-78})$$

$$X + Y = Z + T \quad (\text{B-79})$$

$$ip(Z - T - X + Y) = -J_0((Z + T)(2 - \frac{3}{2} \frac{J_0}{ik}) - \sqrt{3}C) \quad (\text{B-80})$$

$$ip(2Te^{-ipa}) = -J_0(2(Ze^{ipa} + Te^{-ipa}) + \sqrt{3}(e^{ika}(\frac{\sqrt{3}J_0}{2} \frac{1}{ik} (Z + T)) + Ce^{-ika})) \quad (\text{B-81})$$

$$C = e^{ika} \frac{-\sqrt{3}J_0}{2} \frac{1}{ik} (Ze^{ipa} + Te^{-ipa}) \quad (\text{B-82})$$

$$ip(Z - X - X + Z) = -J_0((Z + T)(2 - \frac{3}{2} \frac{J_0}{ik}) - \sqrt{3}C) \quad (\text{B-83})$$

$$ip(2Te^{-ipa}) = -J_0(2(Ze^{ipa} + Te^{-ipa}) + \sqrt{3}(e^{ika}(\frac{\sqrt{3}J_0}{2} \frac{J_0}{ik}(Z + T)) + Ce^{-ika})) \quad (\text{B-84})$$

$$2ip(Z - X) = -J_0((Z + T)\left(2 - \frac{3J_0}{2} \frac{J_0}{ik}\right) - \sqrt{3}(e^{ika} \frac{-\sqrt{3}J_0}{2} \frac{J_0}{ik}(Ze^{ipa} + Te^{-ipa})) \quad (\text{B-85})$$

$$2ip(Te^{-ipa}) = -J_0(2(Ze^{ipa} + Te^{-ipa}) + e^{ika} \frac{3J_0}{2} \frac{J_0}{ik}(Z + T) + \frac{-3J_0}{2} \frac{J_0}{ik}(Ze^{ipa} + Te^{-ipa})) \quad (\text{B-86})$$

$$Te^{-ipa} = \frac{-J_0}{ip}(Ze^{ipa} + Te^{-ipa} + \frac{3J_0}{4} \frac{J_0}{ik}(Z + T)e^{ika} + \frac{-3J_0}{4} \frac{J_0}{ik}(Ze^{ipa} + Te^{-ipa})) \quad (\text{B-87})$$

$$Te^{-ipa} = Z\left(\frac{-J_0}{ip}e^{ipa} + \frac{3J_0^2}{4pk}e^{ika} - \frac{3J_0^2}{4pk}(e^{ipa})\right) + T\left(\frac{-J_0}{ip}e^{ipa} + \frac{3J_0^2}{4pk}e^{ika} - \frac{3J_0^2}{4pk}e^{-ipa}\right) \quad (\text{B-88})$$

$$T = \left(\frac{\frac{-J_0}{ip}e^{ipa} + \frac{3J_0^2}{4pk}e^{ika} - \frac{3J_0^2}{4pk}(e^{ipa})}{e^{-ipa} + \frac{J_0}{ip}e^{-ipa} - \frac{3J_0^2}{4kp}e^{ika} + \frac{3J_0^2}{4kp}e^{-ipa}}\right)Z \quad (\text{B-89})$$

The coefficient is too long, for efficiency, we define:

$$\Gamma = \left(\frac{\frac{-J_0}{ip}e^{ipa} + \frac{3J_0^2}{4pk}e^{ika} - \frac{3J_0^2}{4pk}(e^{ipa})}{e^{-ipa} + \frac{J_0}{ip}e^{-ipa} - \frac{3J_0^2}{4kp}e^{ika} + \frac{3J_0^2}{4kp}e^{-ipa}}\right) \quad (\text{B-90})$$

$$\Gamma = \left(\frac{\frac{-J_0}{ip} + \frac{3J_0^2}{4pk}e^{ika-ipa} - \frac{3J_0^2}{4pk}}{1 + \frac{J_0}{ip} - \frac{3J_0^2}{4kp}e^{ika+ipa} + \frac{3J_0^2}{4kp}}\right)e^{2ipa} \quad (\text{B-91})$$

$$\Gamma = \frac{\gamma_1}{\gamma_2}e^{2ipa} \quad (\text{B-92})$$

so that Eq. B-89 becomes:

$$T = \Gamma Z. \quad (\text{B-93})$$

$$B = \frac{\sqrt{3}J_0}{2} \frac{J_0}{ik}(Z + T) \quad (\text{B-94})$$

$$B = \frac{\sqrt{3} J_0}{2 ik} (1 + \Gamma) Z \quad (\text{B-95})$$

$$2ip(Z - X) = -J_0((Z + T)\left(2 - \frac{3 J_0}{2 ik}\right) - \sqrt{3}(e^{ika} - \frac{\sqrt{3} J_0}{2 ik})(Ze^{ipa} + Te^{-ipa})) \quad (\text{B-96})$$

$$(Z - X) = -\frac{J_0}{ip}((Z + T)\left(1 - \frac{3 J_0}{4 ik}\right) - \sqrt{3}(e^{ika} - \frac{\sqrt{3} J_0}{4 ik})(Ze^{ipa} + Te^{-ipa})) \quad (\text{B-97})$$

$$(Z - X) = ((Z + T)\left(-\frac{J_0}{ip} - \frac{3 J_0^2}{4 kp}\right) + (e^{ika} \frac{3 J_0^2}{4 pk})(Ze^{ipa} + Te^{-ipa})) \quad (\text{B-98})$$

$$X = Z - ((Z + T)\left(-\frac{J_0}{ip} - \frac{3 J_0^2}{4 kp}\right) + (e^{ika} \frac{3 J_0^2}{4 pk})(Ze^{ipa} + Te^{-ipa})) \quad (\text{B-99})$$

$$X = Z\left(1 + \frac{J_0}{ip} + \frac{3 J_0^2}{4 kp} - e^{ika} \frac{3 J_0^2}{4 pk} e^{ipa}\right) + \left(\frac{J_0}{ip} + \frac{3 J_0^2}{4 kp} - e^{ika} \frac{3 J_0^2}{4 pk} e^{-ipa}\right) T \quad (\text{B-100})$$

$$X = Z\gamma_2 - \gamma_1 T \quad (\text{B-101})$$

$$X = (\gamma_2 - \gamma_1 \Gamma) Z \quad (\text{B-102})$$

$$B = \frac{\sqrt{3} J_0}{2 ik} (1 + \Gamma) Z \quad (\text{B-103})$$

$$Z = \frac{1}{\frac{\sqrt{3} J_0}{2 ik} (1 + \Gamma)} B \quad (\text{B-104})$$

$$X = \frac{(\gamma_2 - \gamma_1 \Gamma)}{\frac{\sqrt{3} J_0}{2 ik} (1 + \Gamma)} B \quad (\text{B-105})$$

B.2 Generalization to all J_1

Looking at Eq. B-53, we identify two places that J_1 appear. We define $E + J_1$ as the energy of electron ϵ . This modifies the equation for k as $k = \sqrt{m(\epsilon - 4J_1)}$ for the case mentioned above, however, when the spin-spin coupling is increased so that $\epsilon \leq 4J_1$, k becomes purely imaginary. In this case, the general solution for g becomes:

$$g(x) = \begin{cases} g_I(x) = Ae^{Qx} & x \leq 0 \\ g_{II}(x) = Be^{-Qx} + Ce^{Qx} & a \geq x \geq 0 \\ g_{III}(x) = De^{-Qx} & x \geq a \end{cases} \quad (\text{B-106})$$

where $Q = ik$.

The solution given in the previous holds in this case as well with k replaced with $-iQ$.

$$\Gamma = \left(\frac{\frac{-J_0}{ip} - \frac{3}{4} \frac{J_0^2}{ipQ} e^{Qa-ipa} + \frac{3}{4} \frac{J_0^2}{ipQ}}{1 + \frac{J_0}{ip} + \frac{3}{4} \frac{J_0^2}{ipQ} e^{Qa+ipa} - \frac{3}{4} \frac{J_0^2}{ipQ}} \right) e^{2ipa} \quad (\text{B-107})$$

$$\Gamma = \frac{\gamma_1}{\gamma_2} e^{2ipa} \quad (\text{B-108})$$

$$X = \frac{(\gamma_2 - \gamma_1 \Gamma)}{\frac{\sqrt{3}}{2} \frac{J_0}{Q} (1 + \Gamma)} B \quad (\text{B-109})$$

B.3 Generalization to arbitrary S

For generalization to arbitrary S , we will take a different route.

We will look at how a function, $\phi(x)$ along each basis state is affected by the application of the Hamiltonian. Note that spin flip operation can change the direction (basis) of the function.

Along h :

$$\hat{H}\phi(x)|h\rangle = E\phi(x)|h\rangle \quad (\text{B-110})$$

where $E = \epsilon - 2J_1\hbar^2m^2$ is the total energy of the system and ϵ is the electron energy. In this derivation, for tidiness purposes $m = S$.

$$\left(-\frac{\hbar^2}{2m} \frac{d^2}{dx^2} - 2J_0[\hat{\sigma} \cdot \hat{S}_1\delta(x) + \hat{\sigma} \cdot \hat{S}_2\delta(x-a)] - 2J_1\hat{S}_1 \cdot \hat{S}_2 \right) \phi(x)|h\rangle = E\phi(x)|h\rangle \quad (\text{B-111})$$

The kinetic energy term will be shorthanded as:

$$\hat{T} = -\frac{\hbar^2}{2m} \frac{d^2}{dx^2} \quad (\text{B-112})$$

$$\left(\hat{T} - 2J_0[\hat{\sigma} \cdot \hat{S}_1|h\rangle\delta(x) + \hat{\sigma} \cdot \hat{S}_2|h\rangle\delta(x-a)] - 2J_1\hat{S}_1 \cdot \hat{S}_2|h\rangle \right) \phi(x) = E\phi(x)|h\rangle \quad (\text{B-113})$$

We look at the action of the operators to the state:

$$\hat{\sigma} \cdot \hat{S}_1|h\rangle = (\sigma_z S_{1z} + \frac{1}{2}(\sigma_+ S_{1-} + \sigma_- S_{1+})) \left(\frac{1}{\sqrt{3}} (|\downarrow\downarrow\uparrow\rangle + |\downarrow\uparrow\downarrow\rangle + |\uparrow\downarrow\downarrow\rangle) \right) \quad (\text{B-114})$$

$$= \frac{1}{\sqrt{3}} (\sigma_z S_{1z} + \frac{1}{2}(\sigma_+ S_{1-} + \sigma_- S_{1+})) (|\downarrow\downarrow\uparrow\rangle + |\downarrow\uparrow\downarrow\rangle + |\uparrow\downarrow\downarrow\rangle) \quad (\text{B-115})$$

$$= \frac{\hbar^2}{2\sqrt{3}} ((m|\downarrow\downarrow\uparrow\rangle + (m-1)|\downarrow\uparrow\downarrow\rangle - m|\uparrow\downarrow\downarrow\rangle) + (\sqrt{2m}|\downarrow\uparrow\downarrow\rangle + \sqrt{2m}|\uparrow\downarrow\downarrow\rangle)) \quad (\text{B-116})$$

rewriting the equation in terms of basis states;

$$= \frac{\hbar^2}{2\sqrt{3}}(a_1|h\rangle + b_1|f\rangle + c_1|g\rangle) \quad (\text{B-117})$$

with

$$\begin{aligned} a_1 &= \frac{m-1+2\sqrt{2m}}{\sqrt{3}} \\ b_1 &= \frac{4m-1-\sqrt{2m}}{\sqrt{6}} \\ c_1 &= \frac{-1+\sqrt{2m}}{\sqrt{2}} \end{aligned} \quad (\text{B-118})$$

$$\hat{\sigma} \cdot \hat{S}_2|h\rangle = (\sigma_z S_{2z} + \frac{1}{2}(\sigma_+ S_{2-} + \sigma_- S_{2+}))(\frac{1}{\sqrt{3}}(|\downarrow\downarrow\uparrow\rangle + |\downarrow\uparrow\downarrow\rangle + |\uparrow\downarrow\downarrow\rangle)) \quad (\text{B-119})$$

$$= \frac{\hbar^2}{2\sqrt{3}}(((m-1)|\downarrow\downarrow\uparrow\rangle + m|\downarrow\uparrow\downarrow\rangle - m|\uparrow\downarrow\downarrow\rangle) + (\sqrt{2m}|\downarrow\downarrow\uparrow\rangle + \sqrt{2m}|\uparrow\downarrow\downarrow\rangle)) \quad (\text{B-120})$$

rewriting the equation in terms of basis states;

$$= \frac{\hbar^2}{2\sqrt{3}}(a_2|h\rangle + b_2|f\rangle + c_2|g\rangle) \quad (\text{B-121})$$

with

$$\begin{aligned} a_2 &= \frac{m-1+2\sqrt{2m}}{\sqrt{3}} \\ b_2 &= \frac{4m-1-\sqrt{2m}}{\sqrt{6}} \\ c_2 &= \frac{1-\sqrt{2m}}{\sqrt{2}} \end{aligned} \quad (\text{B-122})$$

$$\hat{S}_1 \hat{S}_2|h\rangle = (S_{1z} S_{2z} + \frac{1}{2}(S_{1+} S_{2-} + S_{1-} S_{2+}))(\frac{1}{\sqrt{3}}(|\downarrow\downarrow\uparrow\rangle + |\downarrow\uparrow\downarrow\rangle + |\uparrow\downarrow\downarrow\rangle)) \quad (\text{B-123})$$

$$= \frac{\hbar^2}{\sqrt{3}}((m(m-1)|\downarrow\downarrow\uparrow\rangle + m(m-1)|\downarrow\uparrow\downarrow\rangle + m^2|\uparrow\downarrow\downarrow\rangle) + \frac{\sqrt{2m}\sqrt{2m}}{2}(|\downarrow\downarrow\uparrow\rangle + |\downarrow\uparrow\downarrow\rangle)) \quad (\text{B-124})$$

$$= \hbar^2 m^2|h\rangle + \frac{\hbar^2}{\sqrt{3}}(-m(|\downarrow\downarrow\uparrow\rangle + |\downarrow\uparrow\downarrow\rangle) + \frac{\sqrt{2m}\sqrt{2m}}{2}(|\downarrow\downarrow\uparrow\rangle + |\downarrow\uparrow\downarrow\rangle)) \quad (\text{B-125})$$

$$= \hbar^2 m^2|h\rangle + \frac{\hbar^2}{\sqrt{3}}((\frac{\sqrt{2m}\sqrt{2m}}{2} - m)(|\downarrow\downarrow\uparrow\rangle + |\downarrow\uparrow\downarrow\rangle)) \quad (\text{B-126})$$

but

$$\frac{\sqrt{2m}\sqrt{2m}}{2} = m \quad (\text{B-127})$$

therefore

$$\hat{S}_1 \cdot \hat{S}_2 |h\rangle = \hbar^2 m^2 |h\rangle \quad (\text{B-128})$$

All these results put together gives:

$$\begin{aligned} \hat{T}\phi(x)|h\rangle - \frac{2J_0\hbar^2}{2\sqrt{3}}\phi(x)[(a_1|h\rangle + b_1|f\rangle + c_1|g\rangle)\delta(x) + \delta(x-a)(a_2|h\rangle + b_2|f\rangle + c_2|g\rangle)] \\ - 2J_1\hbar^2 m^2 \phi(x)|h\rangle = E\phi(x)|h\rangle \end{aligned} \quad (\text{B-129})$$

$$\begin{aligned} \hat{T}\phi(x)|h\rangle - \frac{2J_0\hbar^2}{2\sqrt{3}}\phi(x)[(a_1|h\rangle + b_1|f\rangle + c_1|g\rangle)\delta(x) + \delta(x-a)(a_2|h\rangle + b_2|f\rangle + c_2|g\rangle)] \\ = \epsilon\phi(x)|h\rangle \end{aligned} \quad (\text{B-130})$$

The basis state of $|f\rangle$;

$$\hat{H}\phi(x)|f\rangle = E\phi(x)|f\rangle \quad (\text{B-131})$$

$$\left(\hat{T} - 2J_0[\hat{\sigma} \cdot \hat{S}_1\delta(x) + \hat{\sigma} \cdot \hat{S}_2\delta(x-a)] - 2J_1\hat{S}_1 \cdot \hat{S}_2\right)\phi(x)|f\rangle = E\phi(x)|f\rangle \quad (\text{B-132})$$

$$\left(\hat{T} - 2J_0[\hat{\sigma} \cdot \hat{S}_1|f\rangle\delta(x) + \hat{\sigma} \cdot \hat{S}_2|f\rangle\delta(x-a)] - 2J_1\hat{S}_1 \cdot \hat{S}_2|f\rangle\right)\phi(x) = E\phi(x)|f\rangle \quad (\text{B-133})$$

$$\hat{\sigma} \cdot \hat{S}_1|f\rangle = (\sigma_z S_{1z} + \frac{1}{2}(\sigma_+ S_{1-} + \sigma_- S_{1+}))\left(\frac{1}{\sqrt{6}}(|\downarrow\downarrow\uparrow\rangle + |\downarrow\uparrow\downarrow\rangle - 2|\uparrow\downarrow\downarrow\rangle)\right) \quad (\text{B-134})$$

$$= \frac{1}{\sqrt{6}}(\sigma_z S_{1z} + \frac{1}{2}(\sigma_+ S_{1-} + \sigma_- S_{1+}))(|\downarrow\downarrow\uparrow\rangle + |\downarrow\uparrow\downarrow\rangle - 2|\uparrow\downarrow\downarrow\rangle) \quad (\text{B-135})$$

$$= \frac{\hbar^2}{2\sqrt{6}}((m|\downarrow\downarrow\uparrow\rangle + (m-1)|\downarrow\uparrow\downarrow\rangle + 2m|\uparrow\downarrow\downarrow\rangle) - 2\sqrt{2m}|\downarrow\uparrow\downarrow\rangle + \sqrt{2m}|\uparrow\downarrow\downarrow\rangle) \quad (\text{B-136})$$

rewriting the equation in terms of basis states;

$$= \frac{\hbar^2}{2\sqrt{6}}(a_1|h\rangle + b_1|f\rangle + c_1|g\rangle) \quad (\text{B-137})$$

with

$$\begin{aligned} a_1 &= \frac{4m - 1 - \sqrt{2m}}{\sqrt{3}} \\ b_1 &= \frac{-2m - 1 - 4\sqrt{2m}}{\sqrt{6}} \\ c_1 &= \frac{-1 - 2\sqrt{2m}}{\sqrt{2}} \end{aligned} \quad (\text{B-138})$$

$$\hat{\sigma} \cdot \hat{S}_2 |f\rangle = (\sigma_z S_{2z} + \frac{1}{2}(\sigma_+ S_{2-} + \sigma_- S_{2+})) (\frac{1}{\sqrt{6}}(|\downarrow\downarrow\uparrow\rangle + |\downarrow\uparrow\downarrow\rangle - 2|\uparrow\downarrow\downarrow\rangle)) \quad (\text{B-139})$$

$$= \frac{\hbar^2}{2\sqrt{6}} (((m-1)|\downarrow\downarrow\uparrow\rangle + m|\downarrow\uparrow\downarrow\rangle + 2m|\uparrow\downarrow\downarrow\rangle) - 2\sqrt{2m}|\downarrow\downarrow\uparrow\rangle + \sqrt{2m}|\uparrow\downarrow\downarrow\rangle) \quad (\text{B-140})$$

rewriting the equation in terms of basis states;

$$= \frac{\hbar^2}{2\sqrt{6}} (a_2|h\rangle + b_2|f\rangle + c_2|g\rangle) \quad (\text{B-141})$$

with

$$\begin{aligned} a_1 &= \frac{4m - 1 - \sqrt{2m}}{\sqrt{3}} \\ b_1 &= \frac{-2m - 1 - 4\sqrt{2m}}{\sqrt{6}} \\ c_1 &= \frac{1 + 2\sqrt{2m}}{\sqrt{2}} \end{aligned} \quad (\text{B-142})$$

$$\hat{S}_1 \cdot \hat{S}_2 |f\rangle = (S_{1z} S_{2z} + \frac{1}{2}(S_{1+} S_{2-} + S_{1-} S_{2+})) (\frac{1}{\sqrt{6}}(|\downarrow\downarrow\uparrow\rangle + |\downarrow\uparrow\downarrow\rangle - 2|\uparrow\downarrow\downarrow\rangle)) \quad (\text{B-143})$$

$$= \frac{\hbar^2}{\sqrt{6}} ((m(m-1)|\downarrow\downarrow\uparrow\rangle + m(m-1)|\downarrow\uparrow\downarrow\rangle - 2m^2|\uparrow\downarrow\downarrow\rangle) + \frac{\sqrt{2m}\sqrt{2m}}{2} (|\downarrow\downarrow\uparrow\rangle + |\downarrow\uparrow\downarrow\rangle)) \quad (\text{B-144})$$

$$= \hbar^2 m^2 |f\rangle + \frac{\hbar^2}{\sqrt{6}} (-m(|\downarrow\downarrow\uparrow\rangle + |\downarrow\uparrow\downarrow\rangle) + \frac{\sqrt{2m}\sqrt{2m}}{2} (|\downarrow\downarrow\uparrow\rangle + |\downarrow\uparrow\downarrow\rangle)) \quad (\text{B-145})$$

$$= \hbar^2 m^2 |f\rangle + \frac{\hbar^2}{\sqrt{6}} ((\frac{\sqrt{2m}\sqrt{2m}}{2} - m)(|\downarrow\downarrow\uparrow\rangle + |\downarrow\uparrow\downarrow\rangle)) \quad (\text{B-146})$$

$$\hat{S}_1 \cdot \hat{S}_2 |h\rangle = \hbar^2 m^2 |f\rangle \quad (\text{B-147})$$

All these results put together gives:

$$\hat{T}\phi(x)|f\rangle - \frac{2J_0\hbar^2}{2\sqrt{3}}\phi(x)[(a_1|h\rangle + b_1|f\rangle + c_1|g\rangle)\delta(x) + \delta(x-a)(a_2|h\rangle + b_2|f\rangle + c_2|g\rangle)]$$

$$-2J_1\hbar^2m^2\phi(x)|f\rangle = E\phi(x)|f\rangle \quad (\text{B-148})$$

$$\begin{aligned} \hat{T}\phi(x)|f\rangle - \frac{2J_0\hbar^2}{2\sqrt{3}}\phi(x)[(a_1|h\rangle + b_1|f\rangle + c_1|g\rangle)\delta(x) + \delta(x-a)(a_2|h\rangle + b_2|f\rangle + c_2|g\rangle)] \\ = \epsilon\phi(x)|f\rangle \end{aligned} \quad (\text{B-149})$$

For the basis $|g\rangle$;

$$\hat{H}\phi(x)|g\rangle = E\phi(x)|g\rangle \quad (\text{B-150})$$

$$\left(\hat{T} - 2J_0[\hat{\sigma} \cdot \hat{S}_1\delta(x) + \hat{\sigma} \cdot \hat{S}_2\delta(x-a)] - 2J_1\hat{S}_1 \cdot \hat{S}_2\right)\phi(x)|g\rangle = E\phi(x)|g\rangle \quad (\text{B-151})$$

$$\left(\hat{T} - 2J_0[\hat{\sigma} \cdot \hat{S}_1|g\rangle\delta(x) + \hat{\sigma} \cdot \hat{S}_2|g\rangle\delta(x-a)] - 2J_1\hat{S}_1 \cdot \hat{S}_2|g\rangle\right)\phi(x) = E\phi(x)|g\rangle \quad (\text{B-152})$$

$$\hat{\sigma} \cdot \hat{S}_1|g\rangle = (\sigma_z S_{1z} + \frac{1}{2}(\sigma_+ S_{1-} + \sigma_- S_{1+}))\left(\frac{1}{\sqrt{2}}(|\downarrow\uparrow\downarrow\rangle - |\downarrow\downarrow\uparrow\rangle)\right) \quad (\text{B-153})$$

$$= \frac{1}{\sqrt{2}}(\sigma_z S_{1z} + \frac{1}{2}(\sigma_+ S_{1-} + \sigma_- S_{1+}))(|\downarrow\uparrow\downarrow\rangle - |\downarrow\downarrow\uparrow\rangle) \quad (\text{B-154})$$

$$= \frac{\hbar^2}{2\sqrt{2}}((-m|\downarrow\downarrow\uparrow\rangle + (m-1)|\downarrow\uparrow\downarrow\rangle) + \sqrt{2m}|\uparrow\downarrow\downarrow\rangle) \quad (\text{B-155})$$

rewriting the equation in terms of basis states;

$$= \frac{\hbar^2}{2\sqrt{6}}(a_1|h\rangle + b_1|f\rangle + c_1|g\rangle) \quad (\text{B-156})$$

with

$$\begin{aligned} a_1 &= \frac{-1 + \sqrt{2m}}{\sqrt{3}} \\ b_1 &= \frac{-1 - 2\sqrt{2m}}{\sqrt{6}} \\ c_1 &= \frac{2m - 1}{\sqrt{2}} \end{aligned} \quad (\text{B-157})$$

$$\hat{\sigma} \cdot \hat{S}_2|g\rangle = (\sigma_z S_{2z} + \frac{1}{2}(\sigma_+ S_{2-} + \sigma_- S_{2+}))\left(\frac{1}{\sqrt{2}}(|\downarrow\uparrow\downarrow\rangle - |\downarrow\downarrow\uparrow\rangle)\right) \quad (\text{B-158})$$

$$= \frac{\hbar^2}{2\sqrt{2}}((-m-1)|\downarrow\downarrow\uparrow\rangle + m|\downarrow\uparrow\downarrow\rangle) - \sqrt{2m}|\uparrow\downarrow\downarrow\rangle \quad (\text{B-159})$$

rewriting the equation in terms of basis states;

$$= \frac{\hbar^2}{2\sqrt{6}}(a_2|h\rangle + b_2|f\rangle + c_2|g\rangle) \quad (\text{B-160})$$

with

$$\begin{aligned} a_1 &= \frac{1 - \sqrt{2m}}{\sqrt{3}} \\ b_1 &= \frac{1 - 4\sqrt{2m}}{\sqrt{6}} \\ c_1 &= \frac{2m - 1}{\sqrt{2}} \end{aligned} \quad (\text{B-161})$$

$$\hat{S}_1 \cdot \hat{S}_2|g\rangle = (S_{1z}S_{2z} + \frac{1}{2}(S_{1+}S_{2-} + S_{1-}S_{2+}))(\frac{1}{\sqrt{2}}(|\downarrow\uparrow\downarrow\rangle - |\downarrow\downarrow\uparrow\rangle)) \quad (\text{B-162})$$

$$= \frac{\hbar^2}{\sqrt{2}}((-m(m-1)|\downarrow\downarrow\uparrow\rangle + m(m-1)|\downarrow\uparrow\downarrow\rangle) + \frac{\sqrt{2m}\sqrt{2m}}{2}(|\downarrow\downarrow\uparrow\rangle - |\downarrow\uparrow\downarrow\rangle)) \quad (\text{B-163})$$

$$= \frac{\hbar^2}{\sqrt{2}}(m(m-1) - \frac{\sqrt{2m}\sqrt{2m}}{2})(|\downarrow\uparrow\downarrow\rangle - |\downarrow\downarrow\uparrow\rangle) \quad (\text{B-164})$$

$$= \hbar^2(m^2 - 2m)|g\rangle \quad (\text{B-165})$$

$$\hat{S}_1 \cdot \hat{S}_2|h\rangle = \hbar^2(m^2 - 2m)|g\rangle \quad (\text{B-166})$$

All these results put together gives:

$$\begin{aligned} \hat{T}\phi(x)|g\rangle - \frac{2J_0\hbar^2}{2\sqrt{3}}\phi(x)[(a_1|h\rangle + b_1|f\rangle + c_1|g\rangle)\delta(x) + \delta(x-a)(a_2|h\rangle + b_2|f\rangle + c_2|g\rangle)] \\ - 2J_1\hbar^2(m^2 - 2m)\phi(x)|g\rangle = E\phi(x)|g\rangle \end{aligned} \quad (\text{B-167})$$

$$\begin{aligned} \hat{T}\phi(x)|g\rangle - \frac{2J_0\hbar^2}{2\sqrt{3}}\phi(x)[(a_1|h\rangle + b_1|f\rangle + c_1|g\rangle)\delta(x) + \delta(x-a)(a_2|h\rangle + b_2|f\rangle + c_2|g\rangle)] \\ = (\epsilon - 4J_1\hbar^2m)\phi(x)|g\rangle \end{aligned} \quad (\text{B-168})$$

Appendix C

Expectation value of σ_z

We would like to calculate:

$$\langle \sigma_z \rangle = \frac{\langle \Psi | \sigma_z | \Psi \rangle}{\langle \Psi | \Psi \rangle} \quad (\text{C-1})$$

where:

$$|\Psi\rangle = h(x)|h\rangle + f(x)|f\rangle + g(x)|g\rangle \quad (\text{C-2})$$

the basis states are:

$$|h\rangle = \frac{1}{\sqrt{3}}(|\downarrow\downarrow\uparrow\rangle + |\downarrow\uparrow\downarrow\rangle + |\uparrow\downarrow\downarrow\rangle) \quad (\text{C-3})$$

$$|f\rangle = \frac{1}{\sqrt{6}}(|\downarrow\downarrow\uparrow\rangle + |\downarrow\uparrow\downarrow\rangle - 2|\uparrow\downarrow\downarrow\rangle) \quad (\text{C-4})$$

$$|g\rangle = \frac{1}{\sqrt{2}}(|\downarrow\downarrow\uparrow\rangle - |\downarrow\uparrow\downarrow\rangle) \quad (\text{C-5})$$

$$\sigma_z|h\rangle = \frac{\sigma_z}{\sqrt{3}}(|\downarrow\downarrow\uparrow\rangle + |\downarrow\uparrow\downarrow\rangle + |\uparrow\downarrow\downarrow\rangle) \quad (\text{C-6})$$

$$\sigma_z|f\rangle = \frac{\sigma_z}{\sqrt{6}}(|\downarrow\downarrow\uparrow\rangle + |\downarrow\uparrow\downarrow\rangle - 2|\uparrow\downarrow\downarrow\rangle) \quad (\text{C-7})$$

$$\sigma_z|g\rangle = \frac{\sigma_z}{\sqrt{2}}(|\downarrow\downarrow\uparrow\rangle - |\downarrow\uparrow\downarrow\rangle) \quad (\text{C-8})$$

$$\sigma_z|h\rangle = \frac{1}{2\sqrt{3}}(-|\downarrow\downarrow\uparrow\rangle - |\downarrow\uparrow\downarrow\rangle + |\uparrow\downarrow\downarrow\rangle) \quad (\text{C-9})$$

$$\sigma_z|f\rangle = \frac{1}{2\sqrt{6}}(-|\downarrow\downarrow\uparrow\rangle - |\downarrow\uparrow\downarrow\rangle - 2|\uparrow\downarrow\downarrow\rangle) \quad (\text{C-10})$$

$$\sigma_z|g\rangle = \frac{1}{2\sqrt{2}}(-|\downarrow\downarrow\uparrow\rangle + |\downarrow\uparrow\downarrow\rangle) \quad (\text{C-11})$$

$$\langle h|\sigma_z|h\rangle = \frac{-1}{6} \quad (\text{C-12})$$

$$\langle h|\sigma_z|f\rangle = \langle f|\sigma_z|h\rangle = \frac{-\sqrt{2}}{3} \quad (\text{C-13})$$

$$\langle h|\sigma_z|g\rangle = \langle g|\sigma_z|h\rangle = 0 \quad (\text{C-14})$$

$$\langle f|\sigma_z|f\rangle = \frac{1}{6} \quad (\text{C-15})$$

$$\langle f|\sigma_z|g\rangle = \langle g|\sigma_z|f\rangle = 0 \quad (\text{C-16})$$

$$\langle g|\sigma_z|g\rangle = \frac{-1}{2} \quad (\text{C-17})$$

With these expectation values we would like to calculate:

$$\langle \sigma_z \rangle = \frac{\langle \Psi|\sigma_z|\Psi\rangle}{\langle \Psi|\Psi\rangle} = \frac{(\langle h|h^*(x) + \langle f|f^*(x) + \langle g|g^*(x)\rangle\sigma_z(h(x)|h) + f(x)|f) + g(x)|g))}{|h(x)|^2 + |f(x)|^2 + |g(x)|^2} \quad (\text{C-18})$$

When the state g describes the bound state, we can assume that the contribution to $\langle \sigma_z \rangle$ from this state can be ignored. Within plainwave description, we need to take the integral of numerator and the denominator for the expectation values. Then:

$$\langle \sigma_z \rangle = \frac{\int dx[(\langle h|h^*(x) + \langle f|f^*(x)\rangle\sigma_z(h(x)|h) + f(x)|f))]}{\int dx(|h(x)|^2 + |f(x)|^2)} \quad (\text{C-19})$$

For numerator:

$$\int dx[(\langle h|h^*(x) + \langle f|f^*(x)\rangle\sigma_z(h(x)|h) + f(x)|f)) \quad (\text{C-20})$$

$$= \int dx[\langle h|\sigma_z|h\rangle|h(x)|^2 + \langle h|\sigma_z|f\rangle h^*(x)f(x) + \langle f|\sigma_z|h\rangle f^*(x)h(x) + \langle f|\sigma_z|f\rangle|f(x)|^2] \quad (\text{C-21})$$

$$= \int dx[-\frac{1}{6}|h(x)|^2 - \frac{\sqrt{2}}{3}h^*(x)f(x) - \frac{\sqrt{2}}{3}f^*(x)h(x) + \frac{1}{6}|f(x)|^2] \quad (\text{C-22})$$

We can divide the system to three parts. Since the limit of the integration will be taken to infinity, we ignore the middle component for all functions.

When we look at region I,

$$|h(x)|^2 = |Ae^{ikx} + Be^{-ikx}|^2 = |A|^2 + |B|^2 + AB^*e^{2ikx} + A^*Be^{-2ikx} \quad (\text{C-23})$$

$$h^*(x)f(x) = (A^*e^{-ikx} + B^*e^{ikx})(Xe^{ikx} + Ye^{-ikx}) = A^*X + B^*Y + B^*Xe^{2ikx} + A^*Ye^{-2ikx} \quad (\text{C-24})$$

$$h(x)f^*(x) = (h^*(x)f(x))^* = AX^* + BY^* + BX^*e^{-2ikx} + AY^*e^{2ikx} \quad (\text{C-25})$$

$$|f(x)|^2 = |Xe^{ikx} + Ye^{-ikx}|^2 = |X|^2 + |Y|^2 + XY^*e^{2ikx} + X^*Ye^{-2ikx} \quad (\text{C-26})$$

Similarly for region III,

$$|h(x)|^2 = |Ee^{ikx}|^2 = |E|^2 \quad (\text{C-27})$$

$$h^*(x)f(x) = E^*e^{-ikx}Ve^{ikx} = E^*V \quad (\text{C-28})$$

$$h(x)f^*(x) = Ee^{ikx}V^*e^{-ikx} = EV^* \quad (\text{C-29})$$

$$|f(x)|^2 = |Ve^{ikx}|^2 = |V|^2 \quad (\text{C-30})$$

As the integral limits will be taken to infinity, any term involving exponential function will die off, only constant terms will contribute:

$$\langle \sigma_z \rangle = \frac{\int dx [-\frac{1}{6}|h(x)|^2 - \frac{\sqrt{2}}{3}h^*(x)f(x) - \frac{\sqrt{2}}{3}f^*(x)h(x) + \frac{1}{6}|f(x)|^2]}{\int dx (|h(x)|^2 + |f(x)|^2)} \quad (\text{C-31})$$

$$\langle \sigma_z \rangle = \frac{-\frac{1}{6}(|A|^2 + |B|^2 + |E|^2) - \frac{2\sqrt{2}}{3}\text{Re}(A^*X + B^*Y + E^*V) + \frac{1}{6}(|X|^2 + |Y|^2 + |V|^2)}{|A|^2 + |B|^2 + |E|^2 + |X|^2 + |Y|^2 + |V|^2} \quad (\text{C-32})$$

In our problem, we have the incoming wavepacket as spin up, so $A = \frac{-X}{\sqrt{2}}$. After the wavepacket interacts with the local spins, h and f function reflects and transmits the initial weights. Therefore the total weight of each of these functions should be conserved.

$$|A|^2 = |B|^2 + |E|^2 \quad (\text{C-33})$$

$$|X|^2 = |Y|^2 + |V|^2 \quad (\text{C-34})$$

We set incoming component of the function f to one, $X = 1$. With these parameters;

$$\langle \sigma_z \rangle = \frac{-\frac{1}{6}(\frac{1}{2} + \frac{1}{2}) - \frac{2\sqrt{2}}{3}\text{Re}(A^*X + B^*Y + E^*V) + \frac{1}{6}(1 + 1)}{\frac{1}{2} + \frac{1}{2} + 1 + 1} \quad (\text{C-35})$$

$$\langle \sigma_z \rangle = \frac{\frac{1}{6} - \frac{2\sqrt{2}}{3}\text{Re}(A^* + B^*Y + E^*V)}{3} \quad (\text{C-36})$$

$$\langle \sigma_z \rangle = \frac{\frac{1}{6} + \frac{2}{3} - \frac{2\sqrt{2}}{3}\text{Re}(B^*Y + E^*V)}{3} \quad (\text{C-37})$$

$$\langle \sigma_z \rangle = \frac{5}{18} - \frac{2\sqrt{2}}{9}\text{Re}(B^*Y + E^*V) \quad (\text{C-38})$$